SOME INVESTIGATIONS ON
A WAVEGUIDE FEED PATCH ANTENNA

A DISSERTATION

submitted in partial fulfilment of the
requirements for the award of the degree
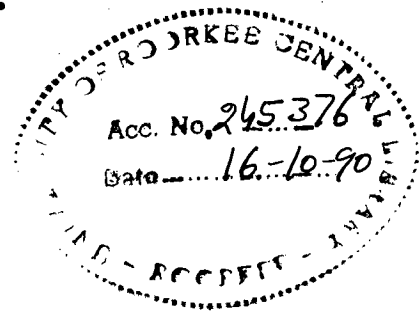*of*

MASTER OF ENGINEERING
in
(ELECTRONICS AND COMPUTER ENGINEERING)
(Microwave and Radar Engineering)

By

HARISH A. R.

DEPARTMENT OF ELECTRONICS AND COMPUTER ENGINEERING
UNIVERSITY OF ROORKEE
ROORKEE-247 667 (INDIA)

MARCH, 1990

CANDIDATE'S DECLARATION

This is to certify that the work which is being presented in the dissertation entitled, 'SOME INVESTIGATIONS ON A WAVEGUIDE FEED PATCH ANTENNA' in partial fulfilment of the requirements for the award of the degree of Master of Engineering in Electronics and Computer Engineering (Microwave and Radar Engineering), submitted in the Department of Electronics and Computer Engineering of the University is an authentic record of my own work carried out during a period from August 1989 to March 1990, under the supervision of Dr. S.N. Sinha.

The matter embodied in this dissertation has not been submitted for the award of any other degree.
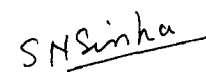
ROORKEE   (HARISH A.R.)

DATED: MARCH 30 , 1990

This is to certify that the above statement made by the candidate is correct to the best of my knowledge.

ROORKEE   (Dr. S.N. SINHA)
                                                      Reader
DATED: MARCH 30 , 1990   Department of Electronics
                                         and Computer Engineering,
                                         University of Roorkee,
                                         ROORKEE-247 667, INDIA.

CONTENTS

ABSTRACT

The microstrip antennas in recent years, are gaining wide publicity due to their numerous advantages. The versatility of this class of antennas at microwave frequencies suggests a potential usefulness at millimeter-wave frequencies. However, it has become apparant that feed structures which operate quite well at microwave frequencies are not viable with millimeter-waves, since the losses become significant in microstrip lines and co-axial feed components are not available above about 50 GHz. For this reason, a new feeding technique for patch antenna, namely, 'waveguide feed', has been studied in this dissertation.

In this work, a moment method analysis has been presented for a microstrip patch antenna coupled to a waveguide via an aperture in its ground plane. Equivalence theorem, in conjunction with the boundary conditions, has been used to set up two coupled integro-differential equations. These are then reduced to matrix form using the method of moments. Though the analysis is quite general, in the sense that no restrictions have been imposed on the shape and size of the patch and the aperture, analytical expressions have been derived for the particular case of a rectangular patch fed by a rectangular waveguide via a rectangular aperture in the ground plane.

Based on the above analysis, a computer program has been developed in FORTRAN, to analyse the structure. Numerical results obtained from the program have been checked for the convergence and compared with the published work for a number of different problems. Some test data have also been presented for a waveguide fed microstrip patch antenna.

Some experimental investigations were also carried out on the waveguide feed patch antenna which was constructed using RT/Duroid 5880. Experimental results have been reported here on the input characteristics, gain, and the radiation pattern of this antenna. Further, the effect of using a slide screw tuner for reducing the impedance mismatch and increasing the size of the ground plane has also been studied.

LIST OF FIGURES

CHAPTER 1

INTRODUCTION

The concept of microwave radiators was first proposed by Deschamps [1] in 1953, but the first practical antennas were developed only in the early 1970's by Howell [2] and Munson [3]. Since then, a considerable amount of research effort has been directed towards exploiting the numerous advantages of this class of antennas.

The microstrip antenna consists of a radiating patch on one side of a dielectric substrate which has a ground plane on the other side. The patch can have any shape but is restricted to some geometrically regular patterns so that the analysis is simplified. A source of current located on the underside of the metallic patch antenna radiates an electromagnetic wave. Some of the waves are diffracted and go back under the patch and store electromagnetic energy. Some radiate out into space and contribute to the useful radiation pattern of the antenna. Yet others, called the surface waves, remain within the dielectric substrate and propagate along the two dimensional air-dielectric interface [4].

Microstrip antennas are inherently narrow band devices and have a low power handling capability. However, since they are thin, light - weight, and conformable, they are very much suitable for applications such as in satellites and avionics.

In addition, this type of antennas can be mass produced using photolithographic technique.

With the increasing popularity of microstrip antennas, the need for accurate modelling is also growing. Apart from accuracy, the models should be numerically efficient to suit the Computer-Aided-Design procedure.

The earliest analytical model for the patch antenna, called the transmission line model, was published by Munson [3]. He modelled the patch as two radiating slots separated by a trans- mission line (Fig. 1.1). Although this model has the advantage of yielding very simple expressions for the radiation admittance, it does not take into account the mutual coupling between the main radiating slots and the influence of side slots on the radiation admittance. Derneryd [5,6] modified the model to account for the mutual coupling between the radiating slots. However, he did not consider the effect of side slots. Pues et al. [7] improvised the model to take into account all these shortcomings.

The transmission line model gives very simple expressions to analyse the behaviour of patch antennas and is very well suited for rectangular patches. However, this model does not take into account the effect of surface waves, diffraction at the substrate and the ground plane edges, and contributions due to higher order modes.

Lo et al. [8] developed an altogether different theory to analyse the patch antennas. The region between the patch

and the ground plane is treated as a cavity bounded by a magnetic wall all along the edge and electric walls above and below (Fig. 1.2). This model assumes that the thickness of the dielectric substrate is small. Therefore, the model fails to predict accurate results when the thickness is large in comparison with the wavelength. Moreover, there is no convenient way to include the effect of surface waves in this model. Additionally, in both these models, length corrections are to be incorporated to take into account the fringing fields.

The transmission line and the cavity models give good results for thin and low dielectric constant substrates. However, these models give relatively inaccurate results for thick or high dielectric constant substrates which are used in MMIC's. Moreover, since the effect of surface waves becomes much more pronounced in thicker substrates with high values of dielectric constant, it should be incorporated in the analysis.

With the development of digital computers, a powerful numerical tool has become available to electromagnetic engineers in the form of method of moments. The moment method [9] essentially utilises the exact Green's function for the grounded dielectric slab and, thus, inherently takes into account the effect of surface wave excitation. In addition, this method rigorously accounts for fringing fields and hence, no adhoc length corrections are needed.

4

Another important area in which a lot of recent research effort has been directed, is the development of feeding techniques for microstrip antennas. This has resulted in a number of feeding techniques, which can be classified into three categories as:

* Direct contact feeds

* Proximity coupled feeds

* Aperture coupled feeds

The earliest and simplest of all these feeds are the direct contact feeds, which include the microstripline feed and the co-axial line feed. In microstripline feed, the microstripline is etched along with the patch on the same substrate. It may touch the patch along the radiating or the non-radiating edge (Fig. 1.3). To obtain a proper impedance match between the feed and the patch, a matching network is also etched on the same substrate between the line and the patch. Alternatively, an impedance match can be provided by connecting the feed line at a suitable point along the radiating edge. The drawbacks of this feed system are that, the feed line also radiates along with the antenna causing degradation of the radiation pattern and the feed structure occupies a large area on the antenna substrate.

The use of a matching transformer and unwanted radiations from the feed line can be avoided by using the co-axial feed. In this case, the inner conductor of the co-axial probe is connected to the patch through the substrate and the outer

conductor is connected to the ground plane (Fig. 1.4). The impedance matching can be obtained by adjusting the position of the feed point.

In case of proximity coupled feeds [10,11], the antenna element is electromagnetically coupled by close proximity to a microstripline. The antenna element may be in the same plane as the feed line (Fig. 1.5(a)) or printed on a superstrate (Fig. 1.5(b)). Tighter coupling can be obtained in the latter case by having the antenna element overlap the feed line. The amount of power coupled to a proximity coupled element can be easily controlled by the spacing between the element and the microstripline.

Pozar [12,13,14] suggested the aperture coupled feeds for the microstrip patch antennas. Here the microstrip antenna is proximity coupled to a small aperture in the ground plane which is coupled to a microstripline (Fig. 1.6). This type of feed arrangement is well suited for monolithic applications since one substrate can be of low permittivity, suitable for printed antenna purposes, while the other substrate can be of higher dielectric constant for active circuit fabrication. The ground plane reduces the spurious coupling from feed to the antenna element and the spurious radiation due to feed circuitry in the front halfspace.

The versatility of the microstrip patch antenna suggests its potential usefulness at millimeter wave (mm-wave) frequencies. However, the feed structures that operate very well at

microwave frequencies are not viable with mm-waves. At mm-wave frequencies, losses become significant in microstripline and co-axial feed components are not available above 50 GHz. The feed line losses can be very significant when one is dealing with an array antenna with its associated complex feed circuitry. It is, therefore, necessary to consider a low loss transmission medium, such as a waveguide, as a feed for microstrip antennas. Some ·preliminary investigations, mainly experimental, were carried out by Greenlee et al. [15] on such a feed system. Their results indicate that an iris-coupled waveguide feed is worthy of consideration, especially for mm-wave microstrip antennas. However, they could not achieve a good impedance match until the iris size was made equal to the waveguide dimension. Since the performance of such an antenna depends upon the waveguide-iris and the iris-patch interactions, which can be rather complex, it is felt that more investigations are required before any firm conclusion can be drawn. Further, since a purely experimental investigation would be too costly, time consuming, and prone to tolerance induced errors, an attempt should be made to develop a suitable theoretical model for this type of feed.

1.1 Statement of the Problem

The problem treated in this dissertation is divided into two parts as follows:

(a) Analysis of a rectangular microstrip patch antenna coupled to a rectangular waveguide via an aperture in its ground plane using the method of moments.

(b) Experimental investigations on the proposed antenna.

1.2 Organisation of the Dissertation

The work embodied in this dissertation has been arranged in five chapters. In Chapter 2, a moment method formulation is presented for analysing the problem of a waveguide fed patch antenna. Explicit formulae have been derived for various matrices and vectors for the particular case of a rectangular patch coupled to a rectangular waveguide via a rectangular aperture in the ground plane. The evaluation of input impedance and the input reflection coefficient are also included in this chapter. The far-field pattern has been computed for the particular case of air-dielectric patch antenna. In Chapter 3, the computer program is discussed and the numerical results obtained from it are presented. In Chapter 4, results of the experimental study conducted on the patch antenna have been presented. Finally, Chapter 5 concludes the dissertation discussing the successes and failures of this work and suggesting some problems for future work.

Also included are two appendices which contain the procedure followed to solve some of the integrals.

RADIATING
SLOTS

PATCH

SIDE SLOTS

DIELECTRIC
SUBSTRATE

GROUND PLANE
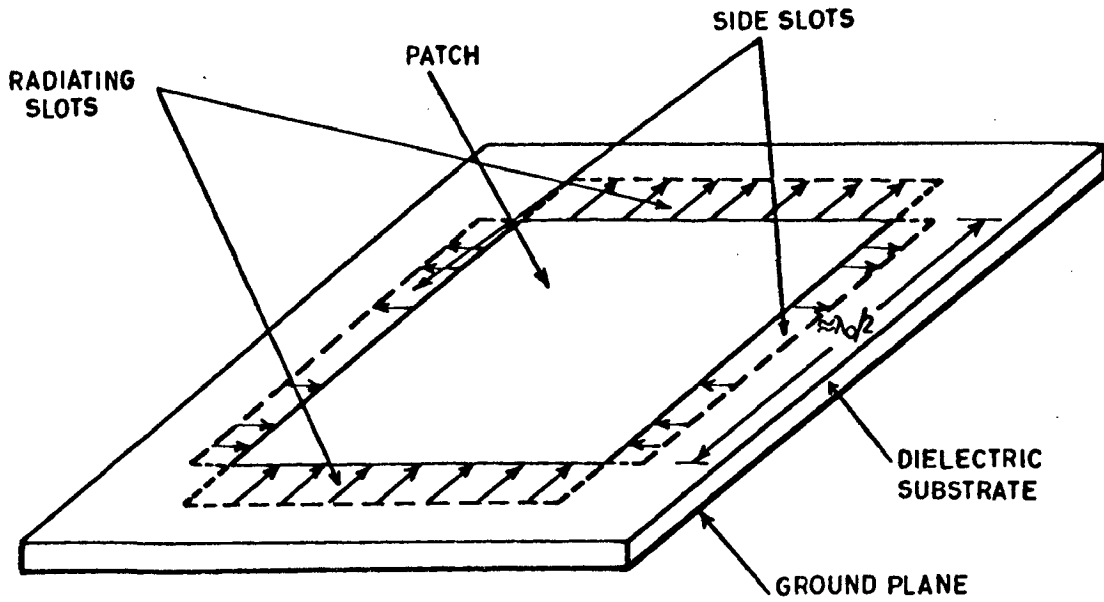
Fig.1.1: Rectangular microstrip antenna with equivalent radiating slots.

ELECTRIC
CONDUCTORS
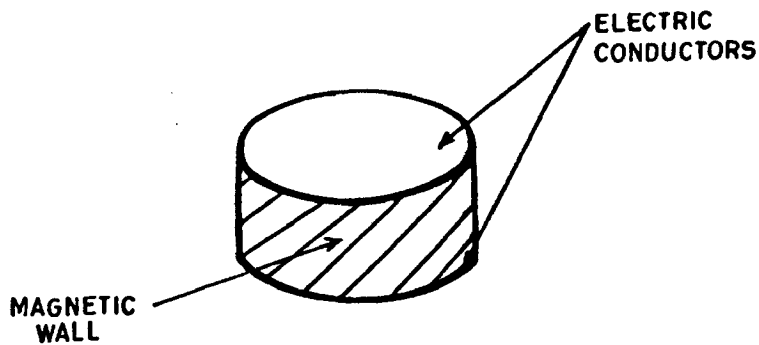
MAGNETIC
WALL

Fig.1.2 : Cavity model indicating electric and magnetic conductors.

Fig.1.4: Co-axial feed.

INNER CONDUCTOR

OUTER CONDUCTOR

PATCH

DIELECTRIC SUBSTRATE

GROUND PLANE

PATCH

GROUND PLANE

ϵ_{r2}

ϵ_{r1}
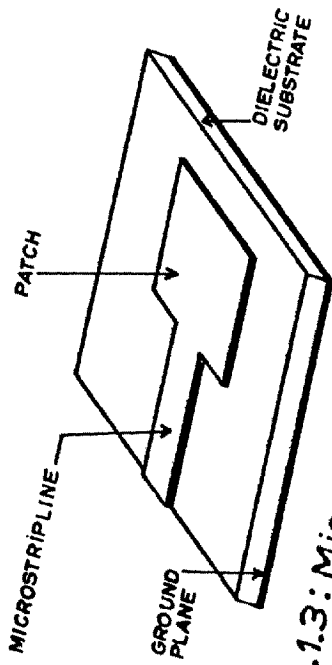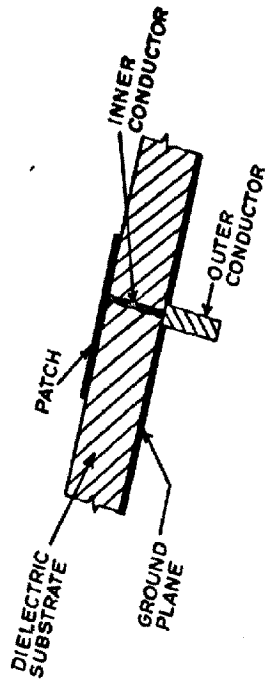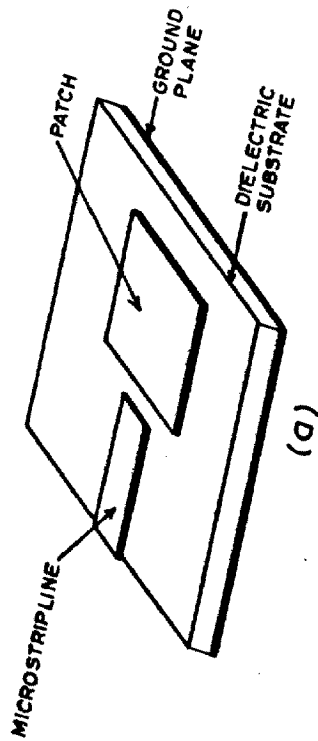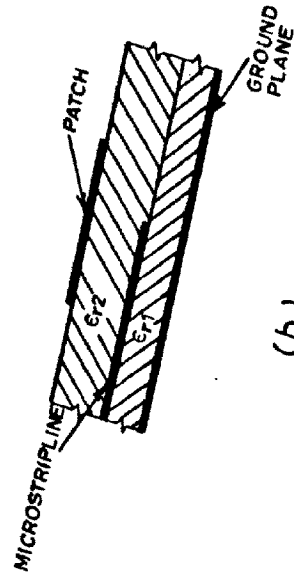
MICROSTRIPLINE

(b)

Fig.1.5: Proximity coupled feeds.

PATCH

MICROSTRIPLINE

GROUND PLANE

DIELECTRIC SUBSTRATE

Fig.1.3: Microstripline feed.

PATCH

GROUND PLANE

DIELECTRIC SUBSTRATE

MICROSTRIPLINE

(a)

9

MICROSTRIPLINE

APERTURE

PATCH

ANTENNA SUBSTRATE

GROUND PLANE

TOP VIEW

MICROSTRIPLINE

GROUND PLANE

APERTURE

MICROSTRIP PATCH

ϵ_{r1}

ϵ_{r2}

SIDE VIEW
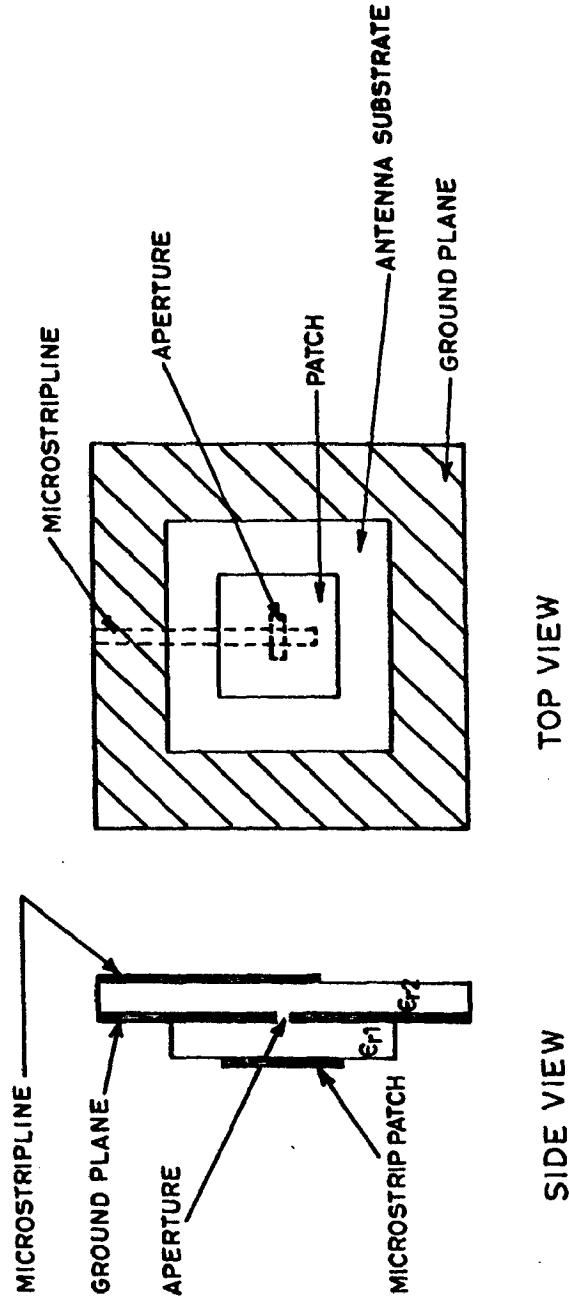
Fig.1.6 : Aperture coupled microstrip antenna .

CHAPTER 2

PROBLEM FORMULATION

In this chapter, a general formulation is presented for the analysis of a microstrip patch antenna coupled to a rectangular waveguide via an aperture in its ground plane. The equivalence principle, in conjunction with the appropriate boundary conditions, is utilised to describe the problem in terms of a pair of coupled integro-differential equations, which are reduced to a set of algebraic equations using the method of moments. These can be solved using a digital computer, yielding magnetic and electric currents on the aperture and the patch respectively. Once the unknown currents are determined, antenna characteristics can be computed using standard techniques.

The general formulation of the boundary value problem and its reduction into matrix form is presented in Section 2.1. Using the piecewise sinusoidal expansion and testing functions, defined in Section 2.2, various matrices and excitation vector are determined in Sections 2.3 through 2.5. The Section 2.6 describes the calculation of input impedance and input reflection coefficient. In Section 2.7 radiated power is calculated along with the radiation pattern.

2.1 Formulation

Figs. 2.1 and 2.2 illustrate the geometry of the problem, the coordinate system, and various parameters used. A perfectly conducting and infinitely thin patch with its centre at (x_{cp}, y_{cp}) and having dimensions $L_p \times W_p$ is placed on the top of a infinitely large grounded dielectric slab having a thickness d and dielectric constant ε. The patch is excited via a rectangular opening in the ground plane of zero thickness having dimensions $L_{ap} \times W_{ap}$ with its centre at (x_c, y_c). This structure is excited by a rectangular waveguide of dimensions $a \times b$, whose axis coincides with the z axis.

The problem can be separated into two distinct regions by the application of equivalence theorem. The aperture is covered by a perfectly conducting screen and equivalent magnetic currents $\overline{M}_s$ and $-\overline{M}_s$ are placed on either side of it (Fig. 2.3). This ensures the continuity of the electric field across the aperture. The equivalent surface magnetic current is given by

$$\overline{M}_s = \hat{z} \times \overline{E} \tag{2.1}$$

where $\overline{E}$ is the aperture electric field of the original problem. Similarly the patch is replaced by an equivalent electric current $\overline{J}_p$, given by

$$\overline{J}_p = \overline{H} \times \hat{z} \tag{2.2}$$

where $\hat{z}$ represents the unit vector in the positive direction of the z-axis and $\overline{H}$ is the patch magnetic field of the original problem.

The application of the equivalence theorem has decoupled the problem into two distinct regions, namely, region 'a' and region 'b'. Region 'a' is a semi-infinite waveguide in which the total field is produced by the impressed sources and the equivalent magnetic current $\overline{M}_s$. Region 'b' is a halfspace with an infinitely large grounded dielectric slab of thickness d. The total field in region 'b' is due to the equivalent magnetic current $-\overline{M}_s$ on the surface S and the equivalent electric current $\overline{J}_p$ on the patch.

The total tangential magnetic field on S in region 'a', $\overline{H}_t^a$ is given by

$$\overline{H}_t^a = \overline{H}_t^{sc} + \overline{H}_t^a(\overline{M}_s) \qquad \text{over S} \qquad (2.3)$$

where $\overline{H}_t^{sc}$ is the tangential component of the magnetic field of the original problem and $\overline{H}_t^a(\overline{M}_s)$ is the tangential magnetic field produced by the equivalent magnetic current $\overline{M}_s$ over S. In region 'b' the total tangential magnetic field over S, $\overline{H}_t^b$ is given by

$$\overline{H}_t^b = \overline{H}_t^b(\overline{J}_p) + \overline{H}_t^b(-\overline{M}_s) \qquad \text{over S} \qquad (2.4)$$

where $\overline{H}_t^b(\overline{J}_p)$ and $\overline{H}_t^b(-\overline{M}_s)$ are the tangential components of magnetic field due to the electric current $\overline{J}_p$ on the patch and the magnetic current $-\overline{M}_s$ over S. The component of electric field tangential to the patch, $\overline{E}_t^b$ is given by

$$\overline{E}_t^b = \overline{E}_t^b(\overline{J}_p) + \overline{E}_t^b(-\overline{M}_s) \qquad \text{over patch} \qquad (2.5)$$

where $\overline{E}_t^b(\overline{J}_p)$ and $\overline{E}_t^b(-\overline{M}_s)$ are the tangential (to patch) components

of electric fields due to electric current $\bar{J}_p$ on the patch and the magnetic current $-\bar{M}_s$ on the surface S. Using the linearity of the operators $\bar{H}_t$ and $\bar{E}_t$, (2.4) and (2.5) can be written as

$$\bar{H}_t^b = \bar{H}_t^b(\bar{J}_p) - \bar{H}_t^b(\bar{M}_s) \tag{2.6}$$

$$\bar{E}_t^b = \bar{E}_t^b(\bar{J}_p) - \bar{E}_t^b(\bar{M}_s) \tag{2.7}$$

Enforcing the boundary condition that the tangential component of $\bar{H}$ is continuous across the aperture, we obtain from (2.4) and (2.6)

$$\bar{H}_t^b(\bar{J}_p) - \bar{H}_t^b(\bar{M}_s) - \bar{H}_t^a(\bar{M}_s) = \bar{H}_t^{sc} \qquad \text{over S} \tag{2.8}$$

On enforcing the other boundary condition, that is, the tangential component of electric field vanishes on the patch, we get, from (2.7)

$$\bar{E}_t^b(\bar{M}_s) - \bar{E}_t^b(\bar{J}_p) = 0 \qquad \text{over patch} \tag{2.9}$$

It is worth noting at this juncture that all these fields are to be evaluated with the aperture closed by a perfectly conducting screen. Equations (2.8) and (2.9) are a pair of coupled integro-differential equations, which are to be solved for the unknown currents $\bar{M}_s$ and $\bar{J}_p$. An approximate solution for (2.8) and (2.9) can be obtained by the method of moments.

In the method of moments, the currents $\bar{M}_s$ and $\bar{J}_p$ are expressed as a set of known expansion functions with some unknown complex coefficients. Let two sets of expansion functions $\{\bar{J}_n, \ n = 1,2,\ldots,N_1\}$ and $\{\bar{M}_j, \ j = 1,2,\ldots,N_2\}$ be defined over

the patch and the surface S, respectively, such that

$$\bar{J}_p = \sum_{n=1}^{N_1} I_n \, \bar{J}_n \qquad (2.10)$$

$$\bar{M}_s = \sum_{j=1}^{N_2} V_j \, \bar{M}_j \qquad (2.11)$$

where $\bar{J}_n$ and $\bar{M}_j$ are the known vector basis functions and I_n and V_j are the unknown complex coefficients to be determined. Substituting (2.10) and (2.11) in (2.8) and (2.9) and using the linearity of the operators, we get

$$\sum_n I_n \, \bar{H}_t^b(\bar{J}_n) - \sum_j V_j \, \bar{H}_t^b(\bar{M}_j) - \sum_j V_j \, \bar{H}_t^a(\bar{M}_j) = \bar{H}_t^{sc}$$

$$\text{over } S \qquad (2.12)$$

$$\sum_j V_j \, \bar{E}_t^b(\bar{M}_j) - \sum_n I_n \, \bar{E}_t^b(\bar{J}_n) = 0 \qquad \text{over patch} \qquad (2.13)$$

Define an inner product for this problem as

$$\langle \bar{A}, \bar{B} \rangle_{S(\text{or patch})} = \iint_{S \atop (\text{or patch})} \bar{A} \cdot \bar{B} \; ds \qquad (2.14)$$

Let us now define two sets of testing functions $\{\bar{U}_m, \; m=1,2,..,N_1\}$ and $\{\bar{W}_i, \; i=1,2,..,N_2\}$ over the patch and the surface S respectively. Taking the inner product of $\bar{W}_i$ with (2.12) and $\bar{U}_m$ with (2.13), we get

$$\sum_n I_n \, \langle \bar{W}_i, \bar{H}_t^b(\bar{J}_n) \rangle - \sum_j V_j \, \langle \bar{W}_i, \bar{H}_t^b(\bar{M}_j) \rangle$$

$$- \sum_j V_j \, \langle \bar{W}_i, \bar{H}_t^a(\bar{M}_j) \rangle = \langle \bar{W}_i, \bar{H}_t^{sc} \rangle$$

$$\text{over } S \qquad (2.15)$$

$$-\sum_n I_n \langle \overline{U}_m, \overline{E}_t^b(\overline{J}_n) \rangle + \sum_j V_j \langle \overline{U}_m, \overline{E}_t^b(\overline{M}_j) \rangle = 0$$

over patch (2.16)

The equations (2.15) and (2.16) can be written in the matrix notation by defining the following matrices and vector.

(i) An admittance matrix for region 'a'

$$[Y^a] = [-\langle \overline{W}_i, \overline{H}_t^a(\overline{M}_j) \rangle]_{N_2 \times N_2}$$ (2.17)

(ii) An admittance matrix for region 'b'

$$[Y^b] = [-\langle \overline{W}_i, \overline{H}_t^b(\overline{M}_j) \rangle]_{N_2 \times N_2}$$ (2.18)

(iii) A matrix due to coupling from patch to surface S

$$[T^b] = [\langle \overline{W}_i, \overline{H}_t^b(\overline{J}_n) \rangle]_{N_2 \times N_1}$$ (2.19)

(iv) A matrix due to coupling from surface S to patch

$$[C^b] = [\langle \overline{U}_m, \overline{E}_t^b(\overline{M}_j) \rangle]_{N_1 \times N_2}$$ (2.20)

(v) An impedance matrix for the patch

$$[Z^b] = [-\langle \overline{U}_m, \overline{E}_t^b(\overline{J}_n) \rangle]_{N_1 \times N_1}$$ (2.21)

(vi) An excitation vector

$$[\vec{I}^i] = [\langle \overline{W}_i, \overline{H}_t^{sc} \rangle]_{N_2 \times 1}$$ (2.22)

(vii) The coefficient vectors

$$[\vec{I}] = [I_n]_{N_1 \times 1}$$ (2.23)

$$[\vec{V}] = [V_j]_{N_2 \times 1} \tag{2.24}$$

Combining the two vectors (2.23) and (2.24)

$$[\vec{V}_T] = \begin{bmatrix} [\vec{I}] \\ [\vec{V}] \end{bmatrix}_{(N_1 + N_2) \times 1} \tag{2.25}$$

Using the definitions (2.17) through (2.25) the equations (2.15) and (2.16) may be written in matrix notation as

$$\begin{bmatrix} [T^b] & [Y^b + Y^a] \\ [Z^b] & [C^b] \end{bmatrix} \begin{bmatrix} [\vec{I}] \\ [\vec{V}] \end{bmatrix} = \begin{bmatrix} [\vec{I}^i] \\ 0 \end{bmatrix} \tag{2.26}$$

which is of the form

$$[Y][\vec{V}_T] = [\vec{I}] \tag{2.27}$$

where

$$[\vec{I}] = \begin{bmatrix} [\vec{I}^i] \\ 0 \end{bmatrix}_{(N_1 + N_2) \times 1} \tag{2.28}$$

The solution of (2.27) is

$$[\vec{V}_T] = [Y]^{-1}[\vec{I}] \tag{2.29}$$

It may be emphasized here that the formulation presented so far is completely general and can be applied to aperture and patch of arbitrary shape and size. However, larger the size of the aperture and patch, more will be the requirements of

computer storage and run time, which places a practical limitation on the size of the problem which can be solved.

2.2 Choice of Expansion and Testing Functions

For the solution of the problem under consideration, we have chosen the same function for both expansion as well as testing. This is known as "Galerkins procedure". Use of Galerkins procedure reduces the computational efforts to a considerable extent.

The rectangular aperture of dimensions $L_{ap} \times W_{ap}$ is subdivided into a number of rectangular subareas of length Δx in the x direction and Δy in the y direction. The set $\overline{M}_j$ of magnetic current expansion functions is further split into a set of x-directed currents, $\overline{M}_j^x$ and a set of y-directed currents, $\overline{M}_j^y$. When the aperture is very narrow compared to the waveguide dimensions, y-directed currents can be neglected. Hence, assuming a narrow aperture, only x-directed magnetic current expansion functions are considered over the aperture in the present problem. These currents are defined as

$$\overline{M}_j^x = \overline{M}_{s+(t-1)(L_x-1)}^x = \hat{x}\ M_j^x = \hat{x}\ S_s^x(x-x_c+ L_{ap}/2)$$

$$P_t^y(y-y_c+ W_{ap}/2) \qquad \begin{array}{l} s = 1,2,\ldots,(L_x-1) \\ t = 1,2,\ldots,L_y \end{array} \qquad (2.30)$$

where L_x and L_y are, respectively, the number of subsections along the x and y directions. S_s^x and P_t^y are, respectively, the piecewise sinusoidal and pulse functions, defined as

$$S_s^x(x-x_1) = \begin{cases} \dfrac{\text{Sin } k_{ap}[\Delta x - |x - x_1 - s\Delta x|]}{\text{Sin } k_{ap}\Delta x} & ; \ x_1 + (s-1)\Delta x \leq x \leq \\ & \qquad x_1 + (s+1)\Delta x \\ 0 & ; \ \text{elsewhere} \end{cases}$$

(2.31)

$$P_t^y(y-y_1) = \begin{cases} 1/\Delta y & ; \ y_1 + (t-1)\Delta y \leq y \leq y_1 + t\Delta y \\ 0 & ; \ \text{elsewhere} \end{cases}$$

(2.32)

where

$$x_1 = x_c - L_{ap}/2$$
$$y_1 = y_c - W_{ap}/2$$

(2.33)

Similarly, the rectangular patch of length L_p and width W_p along x and y directions, respectively, is subdivided into L_{xp} subsections of length Δx_p along x and L_{yp} subsections of length Δy_p along y. The equivalent electric current $\bar{J}_n$ is split into two components namely, $\bar{J}_n^x$ along x direction and $\bar{J}_n^y$ along y direction. For the present case, the x-directed currents, $\bar{J}_n^x$ on the patch will have negligibly small amplitudes as compared with y-directed currents, $\bar{J}_n^y$ [16]. Thus, for the present analysis, only y-directed currents on the patch are considered. These currents are defined as

$$\bar{J}_n^y = \hat{y}\, J_n^y = \hat{y}\, J_{s+(t-1)L_{xp}}^y =$$

$$\hat{y}\, S_t^y(y-y_{cp} + W_p/2)\, P_s^x(x-x_{cp}+L_p/2) \quad \begin{array}{l} s=1,2,\ldots,L_{xp} \\ t=1,2,\ldots,(L_{yp}-1) \end{array}$$

(2.34)

where S_t^y and P_s^x are given by

$$s_t^y(y-y_{1p}) = \begin{bmatrix} \dfrac{\text{Sin } k_e[\Delta y_p - |y - y_{1p} - t\Delta y_p|]}{\text{Sin}(k_e \Delta y_p)} & ; \\[4mm] \quad y_{1p} + (t-1)\Delta y_p \le y \le y_{1p} + (t+1)\Delta y_p \quad (2.35) \\[4mm] 0 & ; \text{ elsewhere} \end{bmatrix}$$

$$P_s^x(x-x_{1p}) = \begin{bmatrix} 1/\Delta x_p & ; \\[4mm] \quad x_{1p} + (s-1)\Delta x_p \le x \le s\Delta x_p + x_{1p} \quad (2.36) \\[4mm] 0 & ; \text{ elsewhere} \end{bmatrix}$$

with

$$\begin{aligned} x_{1p} &= x_{cp} - L_p/2 \\[3mm] y_{1p} &= y_{cp} - W_p/2 \end{aligned} \qquad (2.37)$$

The parameter, k_e is called the effective propagation constant and is given by

$$k_e = \sqrt{e}_{re}\, k_o \qquad (2.38)$$

$$e_{re} = \left(\frac{e_r+1}{2}\right) + \left(\frac{e_r-1}{2}\right)\left(1 + \frac{10d}{W}\right)^{-1/2} \qquad (2.39)$$

$$k_o = \omega\sqrt{\mu_o e_o} \qquad (2.40)$$

The parameter, k_{ap} is given by

$$k_{ap} = (k_o + k_e)/2 \qquad (2.41)$$

where e_r is the relative dielectric constant of the dielectric slab.

2.3 Evaluation of $[Y^a]$

From (2.17) an element of admittance matrix for the waveguide region, $[Y^a]$ is given by

$$Y^a_{ij} = <-\overline{M}_i , \overline{H}^a_t(\overline{M}_j)>$$

The magnetic field due to $\overline{M}_j$, $\overline{H}^a_t(\overline{M}_j)$, can be expressed in terms of the electric vector potential, $\overline{F}_j$ as

$$\overline{H}^a_t(\overline{M}_j) = -j\omega\overline{F}_j + \nabla\nabla.\overline{F}_j/(j\omega\mu_o e_o) \qquad (2.42)$$

with

$$\overline{F}_j = e_o \iint_S \overline{\overline{g}}_m(\overline{r}|\overline{r}').\overline{M}_j(\overline{r}')ds' \qquad (2.43)$$

where $\overline{r}$ and $\overline{r}'$, respectively, denote the position vectors of the field and the source points and $\overline{\overline{g}}_m(\overline{r}|\overline{r}')$ is the dyadic Green's function corresponding to the electric vector potential for the waveguide region and is given by [17]

$$\overline{\overline{g}}_m(\overline{r}|\overline{r}') = \sum_{m=0}^{\infty} \sum_{n=0}^{\infty} \{e_m e_n/(ab\Gamma_{mn})\} \{[\hat{x}\hat{x}(SS)_x(CC)_y$$

$$+ \hat{y}\hat{y}(CC)_x(SS)_y]p(m,n)$$

$$+ \hat{z}\hat{z}(CC)_x(CC)_y \; q(m,n)\} \qquad (2.44)$$

$$p(m,n) = \begin{cases} e^{-\Gamma_{mn}z} \; Cosh(\Gamma_{mn}z') & z > z' \\ \\ e^{-\Gamma_{mn}z'} \; Cosh(\Gamma_{mn}z) & z < z' \end{cases} \qquad (2.45)$$

$$q(m,n) = \begin{cases} e^{-\Gamma_{mn}z} \; Sinh(\Gamma_{mn}z') & z > z' \\ \\ e^{-\Gamma_{mn}z'} \; Sinh(\Gamma_{mn}z) & z < z' \end{cases} \qquad (2.46)$$

where

$$\Gamma^2_{mn} = (m\pi/a)^2 + (n\pi/b)^2 - k^2_o \qquad (2.47)$$

$$(SS)_x = Sin[(m\pi/a)(x+a/2)] \; Sin[(m\pi/a)(x'+a/2)] \qquad (2.48)$$

$$(CC)_y = Cos[(n\pi/b)(y+b/2)] \; Cos[(n\pi/b)(y'+b/2)] \qquad (2.49)$$

and $\mathcal{e}_m$, $\mathcal{e}_n$ are the Newman's numbers, defined as

$$\mathcal{e}_i = \begin{bmatrix} 1 & \text{for} & i = 0 \\ 2 & \text{for} & i > 0 \end{bmatrix} \qquad (2.50)$$

Since $\overline{M}_j$ has only x-directed components, the admittance matrix $[Y^a]$ may be written as

$$[Y^a] = [Y^{axx}] \qquad (2.51)$$

The electric vector potential $\overline{F}_j$ may be obtained by substituting (2.30) and (2.44) in (2.43) as (see Appendix A)

$$\overline{F}_j = \hat{x} \; \mathcal{e}_o \sum_{m=0}^{\infty} \sum_{n=0}^{\infty} (\mathcal{e}_m \mathcal{e}_n/(ab\Gamma_{mn})) \; Sin[(m\pi/a)(x+a/2)]$$
$$Cos[(n\pi/b)(y+b/2)]\{FACT(s,t)\} \qquad (2.52)$$

$$FACT(s,t) = \left[\frac{4 \times k_{ap}}{Sin(k_{ap}\Delta x)\{k^2_{ap}-(m\pi/a)^2\}} \right] \{Cos[(n\pi/b)(y_1+t\Delta y)$$

$$-n\pi\Delta y/(2b)+(n\pi/2)]\}\{Sin[(k_{ap}+(m\pi/a))(\Delta x/2)]\}$$

$$\{Sin[(k_{ap}-(m\pi/a))(\Delta x/2)]\}\{\frac{Sin(n\pi\Delta y/(2b))}{n\pi\Delta y/(2b)}\}$$

$$\{Sin[(m\pi/a)(x_1+s\Delta x)+(m\pi/2)]\} \qquad (2.53)$$

Taking the gradient of the divergence of the vector potential function, we obtain (noting that $\overline{F}_j$ has only x component)

$$\nabla(\nabla \cdot \overline{F}_j) = \hat{x} \frac{\partial^2 F_j^x}{\partial x^2} + \hat{y} \frac{\partial^2 F_j^x}{\partial x \partial y} + \hat{z} \frac{\partial^2 F_j^x}{\partial x \partial z} \qquad (2.54)$$

Substituting (2.54) in (2.42) and simplifying, we get

$$\overline{H}_t^a(\overline{M}_j) = \hat{x}[-j\omega F_j^x + \frac{1}{j\omega\mu_o e_o}(\frac{\partial^2 F_j^x}{\partial x^2})] + \hat{y}[\frac{1}{j\omega\mu_o e_o}(\frac{\partial^2 F_j^x}{\partial x \partial y})]$$

$$+ \hat{z}[\frac{1}{j\omega\mu_o e_o}(\frac{\partial^2 F_j^x}{\partial x \partial z})] \qquad (2.55)$$

Multiplying (2.55), scalarly, by testing function, $\overline{M}_i$

$$\overline{M}_i \cdot \overline{H}_t^a(\overline{M}_j) = -j\omega F_j^x M_i^x + \frac{1}{j\omega\mu_o e_o} M_i^x \frac{\partial^2 F_j^x}{\partial x^2} \qquad (2.56)$$

Substituting (2.30), (2.52) and (2.56) in (2.17) and simplifying, we get

$$Y_{ij}^{axx} = \sum_m \sum_n (e_m e_n/(ab\Gamma_{mn}))\{j\omega e_o + (1/j\omega\mu_o)(m\pi/a)^2\}$$

$$\{FACT(s,t)\}\{FACT(p,q)\} \qquad (2.57)$$

In equation (2.57)

$$i = p+(q-1)(L_x-1) \qquad \begin{array}{l} p=1,2,..,L_x-1 \\ q=1,2,..,L_y \end{array} \qquad (2.58)$$

$$j = s+(t-1)(L_x-1) \qquad \begin{array}{l} s=1,2,..,L_x-1 \\ t=1,2,..,L_y \end{array} \qquad (2.59)$$

FACT(p,q) is given by (2.53) with s and t replaced by p and q respectively.

2.4 Evaluation of $[Y^b]$, $[T^b]$, $[C^b]$ and $[Z^b]$

In this section, expressions have been derived for the evaluation of $[Y^b]$, $[T^b]$, $[C^b]$ and $[Z^b]$. For the evaluation of these matrices, the fields due to a given current in the presence of a grounded dielectric slab are required. The fields can be obtained by convolving the given expansion function against the appropriate Green's function. The required Green's functions are the y-directed electric field and x-directed magnetic field due to a y-directed infinitesimal electric dipole at (x_o, y_o, d) and the same field components due to an x-directed infinitesimal magnetic dipole at $(x_o, y_o, 0)$ for the grounded dielectric slab, where the ground plane and dielectric to air interface are located at $z = 0$ and $z = d$ respectively. These Green's functions are obtained in the spectral domain. In principle, the term, 'Spectral Domain Approach' refers to the application of integral transforms, such as Fourier transforms, to the solution of boundary value and initial value problems [18].

2.4.1 Grounded Slab Green's Functions [19]

The Green's functions due to y-directed infinitesimal electric dipole at (x_o, y_o, d) are:

(1) the y-directed electric field at $z = d$

$$G_{EJyy}(x,y,d \mid x_o, y_o, d) = \int\int_{-\infty}^{\infty} Q_{EJyy}(k_x, k_y)$$

$$e^{jk_x(x-x_o) + jk_y(y-y_o)} \, dk_x \, dk_y \qquad (2.60)$$

$$Q_{EJyy}(k_x,k_y) = -j \frac{Z_o}{4\pi^2 k_o} \frac{(\epsilon_r k_o^2 - k_y^2)k_2 Cos(k_1 d) + j(k_o^2 - k_y^2)k_1 Sin(k_1 d)}{T_e T_m} \times$$

$$Sin(k_1 d) \qquad\qquad (2.61)$$

(2) the x-directed magnetic field at z = 0

$$G_{HJxy}(x,y,0|x_o,y_o,d) = \int\int_{-\infty}^{\infty} Q_{HJxy}(k_x,k_y)$$

$$e^{jk_x(x-x_o)+jk_y(y-y_o)} dk_x\, dk_y \qquad\qquad (2.62)$$

$$Q_{HJxy}(k_x,k_y) = \frac{1}{4\pi^2} \frac{-\epsilon_r k_1 k_2 Cos(k_1 d) + j\{k_y^2(\epsilon_r - 1) - k_1^2\}Sin(k_1 d)}{T_e T_m} \qquad (2.63)$$

The Green's functions due to x-directed infinitesimal magnetic dipole at $(x_o,y_o,0)$ are:

(1) the x-directed magnetic field at z = 0

$$G_{HMxx}(x,y,0|x_o,y_o,0) = \int\int_{-\infty}^{\infty} Q_{HMxx}(k_x,k_y)$$

$$e^{jk_x(x-x_o)+jk_y(y-y_o)} dk_x\, dk_y \qquad\qquad (2.64)$$

$$Q_{HMxx}(k_x,k_y) = -\frac{j}{4\pi^2 k_o Z_o} \frac{1}{k_1 T_e T_m} [jk_x^2 k_1^2(\epsilon_r - 1) + (\epsilon_r k_o^2 - k_x^2) \times$$

$$\{k_1 k_2(\epsilon_r + 1)Sin(k_1 d)Cos(k_1 d) + j(\epsilon_r k_2^2 Sin^2(k_1 d)$$

$$-k_1^2 Cos^2(k_1 d))\}] \qquad\qquad (2.65)$$

(2) the y-directed electric field at z = d

$$G_{EMyx}(x,y,d|x_o,y_o,0) = \int\int\limits_{-\infty}^{\infty} Q_{EMyx}(k_x,k_y)$$

$$e^{jk_x(x-x_o)+jk_y(y-y_o)} \, dk_x \, dk_y \qquad (2.66)$$

$$Q_{EMyx}(k_x,k_y) = -Q_{HJxy}(k_x,k_y) \qquad (2.67)$$

In the equations (2.60) - (2.67)

$$k_1 = \sqrt{e_r k_o^2 - \beta^2} \qquad \begin{array}{l} Re(k_1) \geq 0 \\[6pt] Im(k_1) \leq 0 \end{array} \qquad (2.68)$$

$$k_2 = \sqrt{k_o^2 - \beta^2} \qquad \begin{array}{l} Re(k_2) \geq 0 \\[6pt] Im(k_2) \leq 0 \end{array} \qquad (2.69)$$

$$T_e = k_1 Cos(k_1 d) + jk_2 Sin(k_1 d) \qquad (2.70)$$

$$T_m = e_r k_2 Cos(k_1 d) + jk_1 Sin(k_1 d) \qquad (2.71)$$

$$k_o^2 = \omega^2 \mu_o e_o \qquad (2.72)$$

$$\beta^2 = k_x^2 + k_y^2 \qquad (2.73)$$

$$Z_o = \sqrt{\mu_o/e_o} \qquad (2.74)$$

2.4.2 Evaluation of $[Y^b]$

From (2.18) an element of the matrix $[Y^b]$ is given by

$$Y_{ij}^b = -\langle \bar{M}_i, \bar{H}_t^b(\bar{M}_j) \rangle$$

The magnetic field due to $\overline{M}_j$ can be obtained by convolving the corresponding Green's function, eq.(2.64) with $\overline{M}_j$ as

$$\overline{H}_t^b(\overline{M}_j) = \hat{x} \int_{y_o} \int_{x_o} M_j^x(x_o, y_o) \int\int_{-\infty}^{\infty} Q_{HMxx}(k_x, k_y)$$

$$e^{jk_x(x-x_o)+jk_y(y-y_o)} \, dk_x \, dk_y \, dx_o \, dy_o \qquad (2.75)$$

Taking inner product of $\overline{M}_i$ with $\overline{H}_t^b(\overline{M}_j)$, we get

$$Y_{ij}^b = - \int_y \int_x M_i^x(x,y) \int_{y_o} \int_{x_o} M_j^x(x_o, y_o) \int\int_{-\infty}^{\infty} Q_{HMxx}(k_x, k_y)$$

$$e^{jk_x(x-x_o)+jk_y(y-y_o)} \, dk_x \, dk_y \, dx_o \, dy_o \, dx \, dy \qquad (2.76)$$

This six fold integral can be converted into a double integral by writing

$$Y_{ij}^b = - \int\int_{-\infty}^{\infty} Q_{HMxx}(k_x, k_y) \, F*(M_i^x(x,y)) \, F(M_j^x(x_o, y_o)) \, dk_x \, dk_y$$

$$\qquad (2.77)$$

where

$$F*(M_i^x(x,y)) = F*_{M_i^x}(k_x, k_y)$$

$$= \int_y \int_x M_i^x(x,y) \, e^{jk_x x + jk_y y} \, dx \, dy \qquad (2.78)$$

$$F(M_j^x(x_0,y_0)) = F_{M_j^x}(k_x,k_y)$$

$$= \int_{y_0} \int_{x_0} M_j^x(x_0,y_0) \, e^{-jk_x x_0 - jk_y y_0} \, dx_0 \, dy_0 \quad (2.79)$$

are the complex conjugate of Fourier transform of $M_i^x(x,y)$ and Fourier transform of $M_j^x(x_0,y_0)$ to be evaluated analytically. Equations (2.78) and (2.79) can be separated into k_x dependent and k_y dependent functions as

$$F^*_{M_i^x}(k_x,k_y) = F^*_{M_i^x}(k_x) \, F^*_{M_i^x}(k_y) \quad (2.80)$$

$$F_{M_j^x}(k_x,k_y) = F_{M_j^x}(k_x) \, F_{M_j^x}(k_y) \quad (2.81)$$

The double integral over k_x and k_y in (2.77) can be transformed into polar coordinates by writing

$$k_x = \beta \cos\alpha \quad (2.82)$$

$$k_y = \beta \sin\alpha \quad (2.83)$$

Therefore, equation (2.77) can be written as

$$Y_{ij}^b = - \int_{\alpha=0}^{2\pi} \int_{\beta=0}^{\infty} Q_{HMxx}(k_x,k_y)[F^*_{M_i^x}(k_x) \, F_{M_j^x}(k_x)]$$

$$[F^*_{M_i^x}(k_y) \, F_{M_j^x}(k_y)] \, \beta \, d\beta \, d\alpha \quad (2.84)$$

These Fourier transforms can be obtained by direct integration of (2.78) and (2.79) as (see Appendix B)

$$F^{*}_{M^x_i}(k_x) = \frac{2\,k_{ap}}{k_x^2-k_{ap}^2}\,[Cot(k_{ap}\Delta x) - \frac{Cos(k_x\Delta x)}{Sin(k_{ap}\Delta x)}]\; e^{jk_x(x_1+p\Delta x)}$$

(2.85)

$$F_{M^x_j}(k_x) = \frac{2\,k_{ap}}{k_x^2-k_{ap}^2}\,[Cot(k_{ap}\Delta x) - \frac{Cos(k_x\Delta x)}{Sin(k_{ap}\Delta x)}]\; e^{-jk_x(x_1+s\Delta x)}$$

(2.86)

$$F^{*}_{M^x_i}(k_y) = \frac{Sin(k_y\Delta y/2)}{(k_y\Delta y/2)}\; e^{jk_y(y_1+(q-\frac{1}{2})\Delta y)}$$

(2.87)

$$F_{M^x_j}(k_y) = \frac{Sin(k_y\Delta y/2)}{(k_y\Delta y/2)}\; e^{-jk_y(y_1+(t-\frac{1}{2})\Delta y)}$$

(2.88)

Using (2.65), (2.82), (2.83), and (2.85) through (2.88), the equation (2.84) can be written as

$$Y^b_{ij} = - \int_{\alpha=0}^{2\pi} \int_{\beta=0}^{\infty} Q_{HMxx}(\alpha,\beta)\{F1(\alpha,\beta)\}$$

$$e^{j\beta\Delta x(p-s)Cos\alpha + j\beta\Delta y(q-t)Sin\alpha}\beta\, d\beta\, d\alpha$$

(2.89)

where

$$Q_{HMxx}(\alpha,\beta) = \frac{-j}{4\pi^2 k_o z_o}\frac{1}{k_1}\frac{1}{T_e T_m}[j(\beta Cos\alpha)^2 k_1^2(\varepsilon_r-1)$$

$$+ (\varepsilon_r k_o^2-(\beta Cos\alpha)^2)\{k_1 k_2(\varepsilon_r+1)Sin(k_1 d)Cos(k_1 d)$$

$$+ j(\varepsilon_r k_2^2 Sin^2(k_1 d)-k_1^2 Cos^2(k_1 d))\}]$$

(2.90)

$$F1(\alpha,\beta) = \left[\frac{4\,k_{ap}}{(k_x^2-k_{ap}^2)}\{Cot(k_{ap}\Delta x) - \frac{Cos(\beta\Delta x Cos\alpha)}{Sin(k_{ap}\Delta x)}\}\right.$$

$$\left.\{\frac{Sin(\frac{\beta\Delta y Sin\alpha}{2})}{(\frac{\beta\Delta y Sin\alpha}{2})}\}\right]^2$$

(2.91)

We note from (2.90) and (2.91) that $Q_{HMxx}(\alpha,\beta)$ and $F1(\alpha,\beta)$ are even functions of α. Substituting $\Theta = \alpha-\pi$ in (2.89), we get

$$Y_{ij}^b = - \int_{\beta=0}^{\infty} \int_{\Theta=-\pi}^{\pi} \{Q_{HMxx}(\Theta,\beta)\}\{F1(\Theta,\beta)\}[\{Cos[\beta(p-s)\Delta xCos\Theta] \times$$

$$Cos[\beta(q-t)\Delta ySin\Theta] - Sin[\beta(p-s)\Delta xCos\Theta] \times$$

$$Sin[\beta(q-t)\Delta ySin\Theta]\} + j\{Sin[\beta(p-s)\Delta xCos\Theta] \times$$

$$Cos[\beta(q-t)\Delta ySin\Theta] + Cos[\beta(p-s)\Delta xCos\Theta] \times$$

$$Sin[\beta(q-t)\Delta ySin\Theta]\}] \beta \, d\Theta \, d\beta \qquad (2.92)$$

Using the even and odd property of the integrand, (2.92) reduces to

$$Y_{ij}^b = -2 \int_{\beta=0}^{\infty} \int_{\Theta=0}^{\pi} \{Q_{HMxx}(\Theta,\beta)\}\{F1(\Theta,\beta)\}\{Cos[\beta(p-s)\Delta xCos\Theta] \times$$

$$Cos[\beta(q-t)\Delta ySin\Theta] + jSin[\beta(p-s)\Delta xCos\Theta] \times$$

$$Cos[\beta(q-t)\Delta ySin\Theta]\} \beta \, d\Theta \, d\beta \qquad (2.93)$$

Equation (2.93) may be written as

$$Y_{ij}^b = -2 \int_{\beta=0}^{\infty} \int_{\Theta=0}^{\pi/2} (\quad) \beta \, d\Theta \, d\beta - 2 \int_{\beta=0}^{\infty} \int_{\Theta=0}^{\pi/2} (\quad) \beta \, d\Theta \, d\beta$$

$$(2.94)$$

Substituting $\Theta = \alpha$ in the first integral and $\Theta = \alpha+\pi$ in the second integral of (2.94) and simplifying, we get

$$Y_{ij}^b = -4 \int_{\beta=0}^{\infty} \int_{\alpha=0}^{\pi/2} \{Q_{HMxx}(\alpha,\beta)\}\{F1(\alpha,\beta)\}$$

$$\{Cos[\beta(p-s)\Delta xCos\Theta] \quad Cos[\beta(q-t)Sin\Theta]\} \beta \, d\alpha \, d\beta \qquad (2.95)$$

which can be written as

$$Y_{ij}^b = -4 \int_{\beta=0}^{\infty} \int_{\alpha=0}^{\pi/2} Q_{HMxx}(k_x,k_y) \left[\frac{2}{(k_x^2-k_{ap}^2)}\{k_{ap}Cot(k_{ap}\Delta x) \right.$$

$$\left. - \frac{k_{ap}Cos(k_x\Delta x)}{Sin(k_{ap}\Delta x)}\}\{\frac{Sin(k_y\Delta y/2)}{(k_y\Delta y/2)}\} \right]^2 \times Cos\{k_x(p-s)\Delta x\} \times$$

$$Cos\{k_y(q-t)\Delta y\} \ \beta \ d\alpha \ d\beta \tag{2.96}$$

In equation (2.96)

$$i = p+(q-1)(L_x-1) \qquad \begin{array}{l} p=1,2,..,L_x-1 \\[4pt] q=1,2,..,L_y \end{array} \tag{2.97}$$

$$j = s+(t-1)(L_x-1) \qquad \begin{array}{l} s=1,2,..,L_x-1 \\[4pt] t=1,2,..,L_y \end{array} \tag{2.98}$$

2.4.3 Evaluation of $[T^b]$

From (2.19) an element of the matrix $[T^b]$ is given by

$$T_{in}^b = <\overline{M}_i, \overline{H}_t^b(\overline{J}_n)>$$

Following the procedure of section (2.4.2) and using the Green's function given by (2.62), we get

$$T_{in}^b = 4 \int_{\beta=0}^{\infty} \int_{\alpha=0}^{\pi/2} Q_{HJxy}(k_x,k_y) [\frac{2}{(k_x^2-k_{ap}^2)}\{k_{ap}Cot(k_{ap}\Delta x)$$

$$- \frac{k_{ap}Cos(k_x\Delta x)}{Sin(k_{ap}\Delta x)}\} \times \frac{2}{(k_y^2-k_e^2)}\{k_e Cot(k_e\Delta y_p)$$

$$- \frac{k_e}{Sin(k_e\Delta y_p)}Cos(k_y\Delta y_p)\}] \times [\frac{Sin(k_x\Delta x_p/2)}{(k_x\Delta x_p/2)}] \times$$

$$[\frac{Sin(k_y\Delta y/2)}{(k_y\Delta y/2)}] \times Cos\{k_x(x_1-x_{1p})+k_x\Delta xp-k_x\Delta x_p(s-\tfrac{1}{2})\} \times$$

$$Cos\{k_y(y_1-y_{1p})+k_y\Delta y(q-\tfrac{1}{2})-k_y\Delta y_p t\} \ \beta \ d\alpha \ d\beta \tag{2.99}$$

In (2.99)

$$i = p+(q-1)(L_x-1)$$

$$p=1,2,..,L_x-1$$
$$q=1,2,..,L_y$$

(2.100)

$$n = s+(t-1)(L_{xp})$$

$$s=1,2,..,L_{xp}$$
$$t=1,2,..,L_{yp}-1$$

(2.101)

2.4.4 Evaluation of $[C^b]$

From (2.20) an element of the matrix $[C^b]$ is given by

$$C^b_{mj} = <\bar{J}_m, \bar{E}^b_t(\bar{M}_j)>$$

Following the procedure of section (2.4.2) and using the Green's function given by (2.66), we get

$$C^b_{mj} = 4 \int_{\alpha=0}^{\pi/2} \int_{\beta=0}^{\infty} Q_{EMyx}(k_x, k_y) \left[\frac{2}{(k_x^2-k_{ap}^2)} \{k_{ap} Cot(k_{ap}\Delta x) \right.$$

$$- \frac{k_{ap} Cos(k_x \Delta x)}{Sin(k_{ap}\Delta x)} \} \times \frac{2}{(k_y^2-k_e^2)} \{k_e Cot(k_e \Delta y_p)$$

$$- \frac{k_e}{Sin(k_e \Delta y_p)} Cos(k_y \Delta y_p) \}] \times \left[\frac{Sin(k_x \Delta x_p/2)}{(k_x \Delta x_p/2)} \right] \times$$

$$\left[\frac{Sin(k_y \Delta y/2)}{(k_y \Delta y/2)} \right] \times [Cos\{k_x(x_{1p}-x_1)+k_x\Delta x_p(u-\frac{1}{2})-sk_x\Delta x\}] \times$$

$$[Cos\{k_y(y_{1p}-y_1)-k_y\Delta y(t-\frac{1}{2})+vk_y\Delta y_p\}] \beta d\beta d\alpha$$

(2.102)

In (2.102)

$$m = u+(v-1)(L_{xp})$$

$$u=1,2,..,L_{xp}$$
$$v=1,2,..,L_{yp}-1$$

(2.103)

$$j = s+(t-1)(L_x-1)$$

$$s=1,2,..,L_x-1$$
$$t=1,2,..,L_y$$

(2.104)

2.4.5 Evaluation of $[Z^b]$

From (2.21) an element of the matrix $[Z^b]$ is given by

$$Z_{mn}^b = <\bar{J}_m, \bar{E}_t^b(\bar{J}_n)>$$

Following the procedure of section (2.4.2) and using the Green's function given by (2.60), we get

$$Z_{mn}^b = -4 \int_{\alpha=0}^{\pi/2} \int_{\beta=0}^{\infty} Q_{EJyy}(k_x, k_y) \left[\frac{2}{(k_y^2 - k_e^2)}\{k_e \text{Cot}(k_e \Delta y_p) - \frac{k_e \text{Cos}(k_y \Delta y_p)}{\text{Sin}(k_e \Delta y_p)}\}\{\frac{\text{Sin}(k_x \Delta x_p/2)}{(k_x \Delta x_p/2)}\}\right]^2 \times \text{Cos}[k_x(u-s)\Delta x_p] \times$$

$$\text{Cos}[k_y(v-t)\Delta y_p] \ \beta \ d\beta \ d\alpha \tag{2.105}$$

In (2.105)

$$m = u+(v-1)(L_{xp}) \qquad \begin{array}{l} u=1,2,..,L_{xp} \\ v=1,2,..,L_{yp}-1 \end{array} \tag{2.106}$$

$$n = s+(t-1)(L_{xp}) \qquad \begin{array}{l} s=1,2,..,L_{xp} \\ t=1,2,..,L_{yp}-1 \end{array} \tag{2.107}$$

2.5 Evaluation of Excitation Vector $\vec{I}^i$

From (2.22) an element of the excitation vector is given by

$$I_i^i = <\bar{M}_i, \bar{H}_t^{sc}>$$

The magnetic field of the original problem, tangential to S, $\bar{H}_t^{sc}$ is given by

$$\bar{H}_t^{sc} = \bar{H}_t^{inc} + \bar{H}_t^{ref} \tag{2.108}$$

where $\bar{H}_t^{inc}$ and $\bar{H}_t^{ref}$ are, respectively, the incident and reflected magnetic fields tangential to S. Since the screen is a perfect conductor, $\bar{H}_t^{ref} = \bar{H}_t^{inc}$ and (2.108) reduces to

$$\bar{H}_t^{sc} = 2\,\bar{H}_t^{inc} \qquad\qquad (2.109)$$

Substituting (2.109) in (2.22) we get

$$I_i^i = 2\,<\bar{M}_i,\bar{H}_t^{inc}> \qquad\qquad (2.110)$$

For TE_{mn} mode incidence, the tangential magnetic field on S is given by [11]

$$\bar{H}_t^{inc} = Y_{mn}\,e^{-\Gamma_{mn}z}\,\hat{z} \times \bar{e}_{mn} \qquad\qquad (2.111)$$

where Y_{mn}, Γ_{mn} and $\bar{e}_{mn}$ are, respectively, the characteristic admittance, the propagation constant and the normalized modal vector for the incident mode, and are given by

$$\bar{e}_{mn} = [ab\mathcal{E}_m\mathcal{E}_n/\{(mb)^2+(na)^2\}]^{\frac{1}{2}} \times [\hat{x}(n/b)Cos\{(m\pi/a)(x+a/2)\} \times$$

$$Sin\{(n\pi/b)(y+b/2)\} - \hat{y}(m/a)Sin\{(m\pi/a)(x+a/2)\} \times$$

$$Cos\{(n\pi/b)(y+b/2)\}] \quad \begin{matrix} m=0,1,2,\ldots \\ n=0,1,2,\ldots \end{matrix} \quad m+n \neq 0 \qquad (2.112)$$

$$Y_{mn} = -j\Gamma_{mn}/(Z_o k_o) \qquad\qquad (2.113)$$

Γ_{mn} is given by (2.47)

Z_o is given by (2.72)

k_o is given by (2.74)

From (2.110) and (2.111) an element of the excitation vector can be written as

$$I_i^i = 2\ Y_{mn}\ \iint_S \overline{M}_i \cdot (\hat{z} \times \overline{e}_{mn})\ ds \qquad (2.114)$$

Substituting (2.30) and (2.112) in (2.114) and simplifying, we get

$$I_i^i = 2\ Y_{mn}\ A_{imn} \qquad (2.115)$$

where

$$A_{imn} = [ab\Theta_m\Theta_n/\{(mb)^2+(na)^2\}]^{1/2}\ (m/a)\{FACT(p,q)\} \qquad (2.116)$$

FACT(p,q) is given by (2.53) with s and t replaced by p and q respectively.

In (2.115) and (2.116)

$$i = p+(q-1)(L_x-1) \qquad \begin{array}{l} p=1,2,..,L_x-1 \\ q=1,2,..,L_y \end{array} \qquad (2.117)$$

2.6 Evaluation of Input Characteristics

In this section, expressions for the calculation of input characteristics like standing wave ratio, reflection coefficient and impedance are derived. First the reflection coefficient is obtained in terms of complex amplitudes of the current on the aperture. Once the reflection coefficient is determined, the other parameters can be obtained without any difficulty.

For the calculation of the reflection coefficient, let z = 0 be the reference plane. The reflection coefficient is given by

$$\Gamma = \frac{V^-}{V^+} \qquad (2.118)$$

where V^+ and V^- are the amplitudes of the incoming and outgoing

waves at the reference plane. Assuming the energy is incident in TE_{10} mode, the total electric field transverse to the direction of propagation (z axis) in region 'a' is given by

$$\overline{E}_t^a = \overline{E}_t^{inc} + \overline{E}_t^{ref} + \overline{E}_t(\overline{M}_s) \qquad (2.119)$$

where $\overline{E}_t^{inc}$ and $\overline{E}_t^{ref}$ are the transverse (to the direction of propagation) components of the incident and reflected fields and $\overline{E}_t(\overline{M}_s)$ is the transverse field produced by $\overline{M}_s$ at $z = 0$. The expressions for the above fields may be written as

$$\overline{E}_t^{inc} = e^{-\Gamma_o z} \overline{e}_o^a \qquad (2.120)$$

$$\overline{E}_t^{ref} = -e^{\Gamma_o z} \overline{e}_o^a \qquad (2.121)$$

$$\overline{E}_t^a(\overline{M}_s) = \sum_{i=1}^{N_2} V_i \overline{E}_t^a(\overline{M}_i) \qquad (2.122)$$

with

$$\overline{E}_t^a(\overline{M}_i) = A_{io} e^{\Gamma_o z} \overline{e}_o^a \qquad (2.123)$$

where the subscript 'o' denotes the dominant mode, $\overline{e}_o^a$ is the normalized modal vector and A_{io} are the modal amplitudes given by (2.112) and (2.116) with $m = 1$ and $n = 0$, respectively. At the interface (2.120) through (2.123) reduce to

$$\overline{E}_t^{inc} = \overline{e}_o^a \qquad (2.124)$$

$$\overline{E}_t^{ref} = -\overline{e}_o^a \qquad (2.125)$$

$$\overline{E}_t^a(\overline{M}_s) = \sum_{i=1}^{N_2} V_i \overline{E}_t^a(\overline{M}_i) \qquad (2.126)$$

with

$$\overline{E}_t^a(\overline{M}_i) = A_{io}\ \overline{e}_o^a \tag{2.127}$$

Now, the amplitudes of the incoming and outgoing waves at the interface can be written as

$$V^+ = \overline{e}_o^a \tag{2.128}$$

$$V^- = -\ \overline{e}_o^a + \sum_{i=1}^{N_2} V_i\ A_{io}\ \overline{e}_o^a \tag{2.129}$$

From (2.118), (2.128) and (2.129) we obtain the value of the input reflection coefficient as

$$\Gamma = -1 + \sum_{i=1}^{N_2} V_i\ A_{io} \tag{2.130}$$

The normalized input impedance is now given by

$$\overline{Z}_{in} = \frac{1+\Gamma}{1-\Gamma} \tag{2.131}$$

whereas, the voltage standing wave ratio, VSWR is

$$VSWR = \frac{1+|\Gamma|}{1-|\Gamma|} \tag{2.132}$$

2.7 Far Field Calculations

The far field computation in this work has been carried out with a view to verify the present theory by comparison with previously published works. Since these include the radiation from a waveguide aperture into free space with (or without) a rectangular plate in its near field, we have considered only the particular case of air-dielectric patch antenna.

Fig. 2.4 shows the geometry for the measurement of a compo-
nent E_m of electric field at a point $\bar{r}_m$ in the region $z > 0$.
This measurement may be carried out by placing an electric dipole
$I\bar{l}_m \delta(\bar{r}-\bar{r}_m)$ at $\bar{r}_m$ and applying the reciprocity theorem to its
field and to the original field. The two sets of sources here
are the dipole at $\bar{r}_m$ and the electric current $\bar{J}_p$ on the patch
and magnetic current $\bar{M}_s$ on the surface S, radiating in the
presence of a continuous ground plane at $z = 0$. On application
of image theory the ground plane can be removed and the two
sets of sources become

1. electric dipole at $\bar{r}_m$

2. the magnetic current $-2\bar{M}_s$ over S, electric current $\bar{J}_p$
   over the patch and the electric current $-\bar{J}_p$ over the
   image of the patch.

Using the reciprocity theorem, the component of electric
field in the direction of $I\bar{l}_m$ at $\bar{r}_m$ due to the second set of
sources may be written as [20]

$$Il_m E_m = 2 \iint_S \bar{M}_s \cdot \bar{H}^m \, ds + \iint_{patch} \bar{J}_p \cdot \bar{E}_1^m \, ds - \iint_{\substack{Image\ of \\ patch}} \bar{J}_p \cdot \bar{E}_2^m \, ds$$

$$(2.133)$$

where $\bar{E}_1^m$ and $\bar{E}_2^m$ are respectively, the electric fields at patch
and its image due to the dipole at $\bar{r}_m$ while E_m denotes the compo-
nent of $\bar{E}_m$ in the direction of dipole. Since the patch is
parallel to XY plane (2.133) reduces to

$$Il_m \ E_m = 2 \iint_S \overline{M}_s \cdot \overline{H}^m \ ds + \iint_{patch} \overline{J}_p \cdot (\overline{E}^m_1 - \overline{E}^m_2) \ ds \qquad (2.134)$$

Substituting (2.10) and (2.11) in (2.134) we obtain

$$Il_m \ E_m = \sum_n I_n \iint_{patch} \overline{J}_n \cdot (\overline{E}^m_1 - \overline{E}^m_2) \ ds$$

$$+ 2 \sum_j V_j \iint_S \overline{M}_j \cdot \overline{H}^m \ ds \qquad (2.135)$$

Since the scalar products in the integrands of (2.135) would involve only the tangential component of fields, we can write

$$Il_m \ E_m = \sum_n I_n \ \langle \overline{J}_n , (\overline{E}^m_{1t} - \overline{E}^m_{2t}) \rangle + 2 \sum_j V_j \ \langle \overline{M}_j , \overline{H}^m_t \rangle \qquad (2.136)$$

or

$$Il_m \ E_m = [\vec{p}^{m1} \quad \vec{p}^{m2}] \begin{bmatrix} \vec{I} \\ \vec{V} \end{bmatrix} \qquad (2.137)$$

where

$$\vec{p}^{m1} = [\langle \overline{J}_n , (\overline{E}^m_{1t} - \overline{E}^m_{2t}) \rangle] \qquad (2.138)$$

$$\vec{p}^{m2} = [2 \langle \overline{M}_j , \overline{H}^m_t \rangle] \qquad (2.139)$$

In order to obtain a component $\overline{E}_m$ on the radiation sphere, we orient the dipole $I\overline{l}_m$ perpendicular to $\overline{r}_m$ and let $\overline{r}_m$ tend to infinity. At the same time $I\overline{l}_m$ is adjusted so that it produces a unit plane wave in the vicinity of the origin. The required dipole moment is given by

$$\frac{1}{Il_m} = - \frac{j\omega\mu}{4\pi r_m} e^{-jk_o r_m} \qquad (2.140)$$

and the plane wave produced in the vicinity of the origin is

$$\bar{E}^m = \hat{u}_m \ e^{-j\bar{k}_m \cdot \bar{r}} \qquad (2.141)$$

$$\bar{H}^m = \frac{1}{\eta}(\hat{k}_m \times \hat{u}_m) \ e^{-j\bar{k}_m \cdot \bar{r}} \qquad (2.142)$$

where $\hat{u}_m$ is the unit vector specifying the polarisation of the wave, $\bar{k}_m$ is the wave number vector pointing in the direction of wave travel and $\bar{r}$ is the position vector of any general point on S or on patch. Substituting (2.140) in (2.137), we obtain

$$E_m = \frac{-j\omega\mu_o}{4\pi r_m} \ e^{-jk_o r_m} \ [\vec{P}^{m1} \quad \vec{P}^{m2}] \begin{bmatrix} \vec{I} \\ \vec{V} \end{bmatrix} \qquad (2.143)$$

$$= \frac{-jk_o\eta}{4\pi r_m} \ e^{-jk_o r_m} \ [\vec{P}^{m1} \quad \vec{P}^{m2}] \begin{bmatrix} \vec{I} \\ \vec{V} \end{bmatrix} \qquad (2.144)$$

Once the measurement vectors $\vec{P}^{m1}$ and $\vec{P}^{m2}$ are determined, the far zone electric field can be calculated using (2.144).

2.7.1 Determination of Measurement Vectors

In order to determine $\vec{P}^{m1}$ (equation (2.138)), we first determine $\bar{E}^m_{1t}$ and $\bar{E}^m_{2t}$. $\bar{E}^m_{1t}$ is the tangential component of electric field at any point on the patch. The position vector of any point on the patch is given by

$$\bar{r} = x\hat{x} + y\hat{y} + d\hat{z} \qquad (2.145)$$

For the geometry shown

$$\bar{k}_m = -k_o \ \hat{r}_m = -k_o \ [\cos\theta \ \hat{x} + \sin\theta \ \cos\varphi \ \hat{y} + \sin\theta \ \sin\varphi \ \hat{z}] \qquad (2.146)$$

Using (2.145) and (2.146) we may write

$$\bar{k}_m \cdot \bar{r} = -k_o \ [x\cos\theta + y\sin\theta \ \cos\varphi + d\sin\theta \ \sin\varphi] \qquad (2.147)$$

Similarly, $\bar{E}_{2t}^m$ is the tangential component of electric field at any point on the image of the patch. The position vector of any point on the image of the patch is given by

$$\bar{r} = x\hat{x} + y\hat{y} - d\hat{z} \qquad (2.148)$$

Using (2.146) and (2.148) we may write

$$\bar{k}_m \cdot \bar{r} = -k_o \ [x\cos\theta + y\sin\theta \ \cos\varphi - d\sin\theta \ \sin\varphi] \qquad (2.149)$$

Let $(P_n^{ml})_{yy}^y$ be the measurement vector due to y component of current on patch for y polarised wave in y = 0 plane ($\varphi = 90°$). Using (2.138), (2.141), (2.147) and (2.149) we can write

$$(P_n^{ml})_{yy}^y = \iint_{patch} \bar{J}_n^y \cdot \hat{y} \ \{e^{jk_o(x\cos\theta + d\sin\theta)}$$

$$- e^{jk_o(x\cos\theta - d\sin\theta)} \} \ dx \ dy \qquad (2.150)$$

which can be integrated directly to obtain

$$(P_n^{ml})_{yy}^y = [4j\sin(k_o d\sin\theta)] \left[\frac{\sin(\frac{k_o \Delta x_p \cos\theta}{2})}{(\frac{k_o \Delta x_p \cos\theta}{2})} \right] \times$$

$$\left[\frac{1 - \cos(k_e \Delta y_p)}{k_e \sin(k_e \Delta y_p)} \right] \qquad (2.151)$$

Let $(P_n^{ml})_{\varphi x}^y$ be the measurement vector due to y component of current on the patch for φ polarised wave in x = 0 plane ($\theta = 90°$), which can be written as

$$(P_n^{ml})_{\varphi x}^y = \iint\limits_{patch} \bar{J}_n^y \cdot \hat{\varphi} \{e^{jk_o(yCos\varphi+dSin\varphi)}$$

$$- e^{jk_o(yCos\varphi-dSin\varphi)} \} \, dx \, dy \qquad (2.152)$$

On integrating we get

$$(P_n^{ml})_{\varphi x}^y = [-4jSin(k_odSin\varphi)] \left[\frac{Sin\varphi}{\{(k_oCos\varphi)^2-k_e^2\}} \right] \times$$

$$\left[k_eCot(k_e\Delta y_p) - \frac{k_eCos(k_o\Delta y_pCos\varphi)}{Sin(k_e\Delta y_p)} \right] \times$$

$$e^{jk_o(y_{1p}+v\Delta y_p)Cos\varphi} \qquad (2.153)$$

In order to evaluate $\bar{P}^{m2}$ (eq. 2.139), we first determine $\bar{H}_t^m$, the tangential component of magnetic field at any point $\bar{r}$ on aperture. The position vector $\bar{r}$ is given by

$$\bar{r} = x\hat{x} + y\hat{y} \qquad (2.154)$$

Let $(P_j^{m2})_{yy}^x$ be the measurment vector due to x component of current on the aperture for the y polarised wave in y = 0 plane (φ=90°). The y polarised wave is given by (2.142) with $\hat{u}_m = \hat{y}$. Using (2.142), (2.146) and (2.154) we can write

$$\hat{k}_m \times \hat{u}_m = -Cos\theta \, \hat{z} + Sin\theta \, \hat{x} \qquad (2.155)$$

$$\bar{k}_m \cdot \bar{r} = -k_o[xCos\theta + ySin\theta] \qquad (2.156)$$

Thus, the measurement vector may be written as

$$(P_j^{m2})_{yy}^x = \frac{2Sin\theta}{n} \iint\limits_{s} \bar{M}_j^x \cdot \hat{x} \, e^{jk_oxCos\theta} \, dx \, dy \qquad (2.157)$$

which may be readily integrated to get

$$(P_j^{m2})_{yy}^x = 4 \frac{Sin\Theta}{\eta} \frac{1}{[(k_o Cos\Theta)^2 - k_{ap}^2]} \left[k_{ap} Cot(k_{ap}\Delta x) \right.$$

$$\left. - \frac{k_{ap} Cos(k_o \Delta x Cos\Theta)}{Sin(k_{ap}\Delta x)} \right] e^{jk_o(x_1 + s\Delta x)Cos\Theta} \qquad (2.158)$$

Let $(P_j^{m2})_{\varphi x}^x$ be the measurement vector due to the x component of current over the aperture for φ polarised wave in x = 0 plane (Θ=90°). The φ polarised wave is given by (2.142) with $\hat{u}$ = $\hat{\varphi}$. Therefore, we can write

$$(P_j^{m2})_{\varphi x}^x = \frac{2}{\eta} \iint_S \bar{M}_j^x \cdot \hat{\theta} \ e^{jk_o y Cos\varphi} \ dx \ dy \qquad (2.159)$$

On integrating (2.159), we get

$$(P_j^{m2})_{\varphi x}^x = - \frac{4}{\eta k_{ap}} \left[\frac{Sin(\frac{k_o \Delta y Cos\varphi}{2})}{(\frac{k_o \Delta y Cos\varphi}{2})} \right] \left[\frac{1}{Sin(k_{ap}\Delta x)} \right.$$

$$\left. - Cot(k_{ap}\Delta x) \right] e^{jk_o[y_1 + (t-\frac{1}{2})\Delta y]Cos\varphi} \qquad (2.160)$$

At this juncture it may be emphasized that the yy components of the measurement vector can be used to obtain the H field pattern and φx components can be used to determine the E field pattern.

2.7.2 Determination of Pattern Gain

The directive gain, $G(\Theta,\varphi)$ of a radiating system in a given direction is defined as the ratio of the radiation intensity in that direction to the average radiated power. Thus,

$$G(\theta,\varphi) = \frac{\psi(\theta,\varphi)}{\psi_{av}} \qquad (2.161)$$

If P_t is the total complex power radiated, than the average radiated power is

$$\psi_{av} = \frac{\text{Real}(P_t)}{4\pi} \qquad (2.162)$$

Also, the radiation intensity in a given direction is

$$\psi(\theta,\varphi) = \frac{r_m^2 \, |\bar{E}_m|^2}{\eta} \qquad (2.163)$$

where $\bar{E}_m$ is the electric field intensity at the measurement point and r_m is the distance of this point from the origin of coordinate system. Substituting (2.162) and (2.163) in (2.161) and using (2.144), we obtain

$$G(\theta,\varphi) = \frac{k_o^2 \eta}{4\pi \, \text{Real}(P_t)} \left| [\vec{p}^{m1} \quad \vec{p}^{m2}] \begin{bmatrix} \vec{I} \\ \vec{V} \end{bmatrix} \right|^2 \qquad (2.164)$$

2.7.3 Determination of Complex Power

The complex power, P_t transmitted through the aperture is

$$P_t = \iint_S \bar{E} \times \bar{H}^* \cdot \hat{z} \, ds \qquad (2.165)$$

where * denotes the complex conjugate. Using (2.1) P_t may be written as

$$P_t = \iint_S \bar{M}_s \cdot \bar{H}^* \, ds \qquad (2.166)$$

Using (2.4), (2.10) and (2.11), in (2.166), we obtain

$$P_t = \sum_{i=1}^{N_2} \sum_{n=1}^{N_1} V_i \, I_n^* \iint_S \overline{M}_i \cdot (\overline{H}_t^b(\overline{J}_n))^* \, ds$$

$$- \sum_{i=1}^{N_2} \sum_{i=1}^{N_2} V_i \, V_j^* \iint_S \overline{M}_i \cdot (\overline{H}_t^b(\overline{M}_j))^* \, ds \qquad (2.167)$$

Using (2.18) and (2.19) equation (2.167) can be written in the matrix form as

$$P_t = [\vec{I} \quad \vec{V}] \begin{bmatrix} 0 & 0 \\ [Y^b]^* & [T^b]^* \end{bmatrix} \begin{bmatrix} \vec{I}^* \\ \vec{V}^* \end{bmatrix} \qquad (2.168)$$

2.8 Summary

In this chapter moment method has been used to analyse a waveguide fed patch antenna. Although the basic formulation is quite general, the expressions have been developed for the specific case of a rectangular patch antenna excited via a rectangular aperture. Equations for the input characteristics namely, VSWR, input impedance and input reflection coefficient have been derived. Also, the expressions for the computation of far field quantities have been determined for the particular case of an air-dielectric patch antenna.
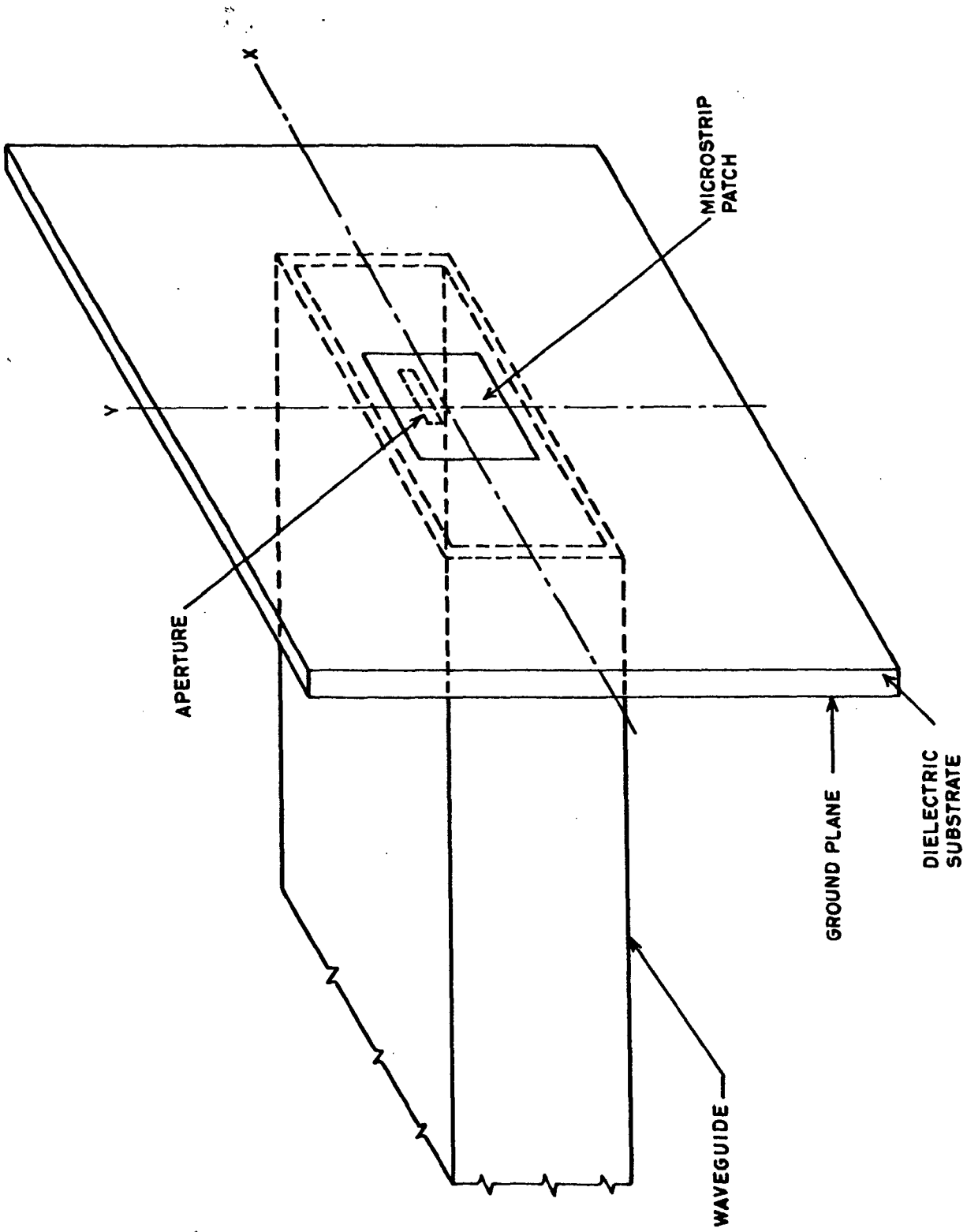
Fig.2.1: Waveguide fed microstrip patch antenna.

APERTURE

PATCH

WAVEGUIDE

L_{ap}

W_{ap} (x_c, y_c)

(x_{cp}, y_{cp})

W_p

b

L_p

a

(a) TOP VIEW

Z

APERTURE

PATCH

DIELECTRIC SUBSTRATE

d

X

GROUND PLANE

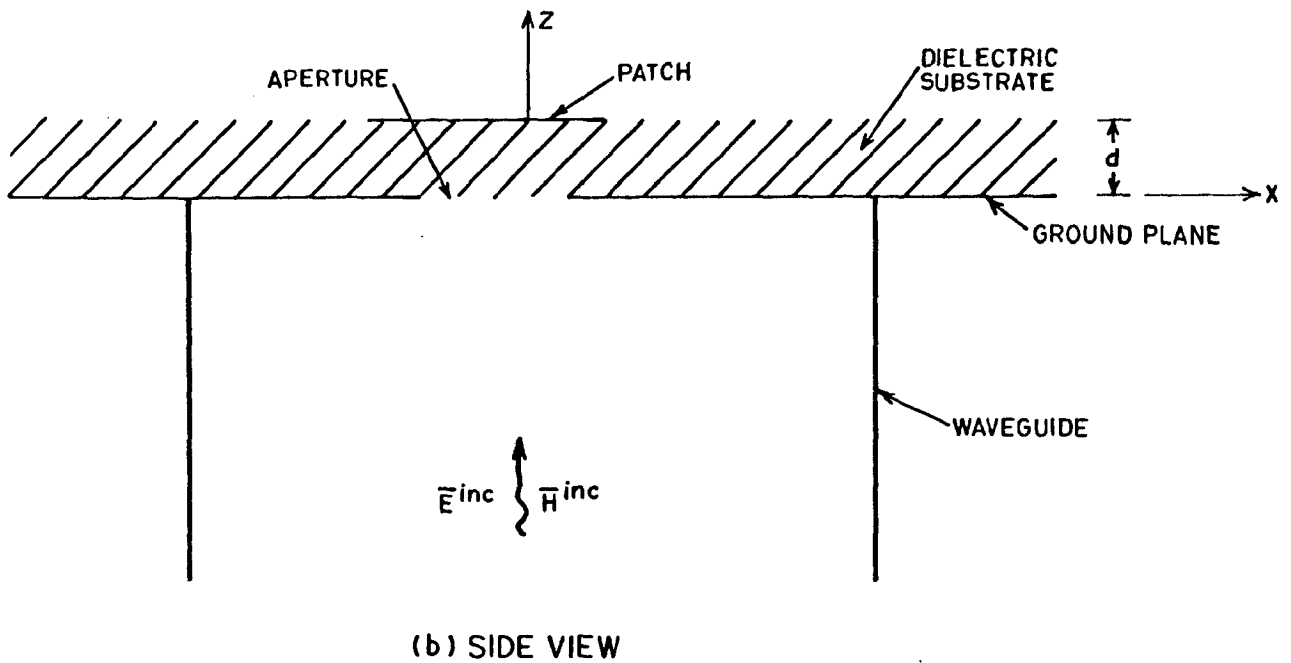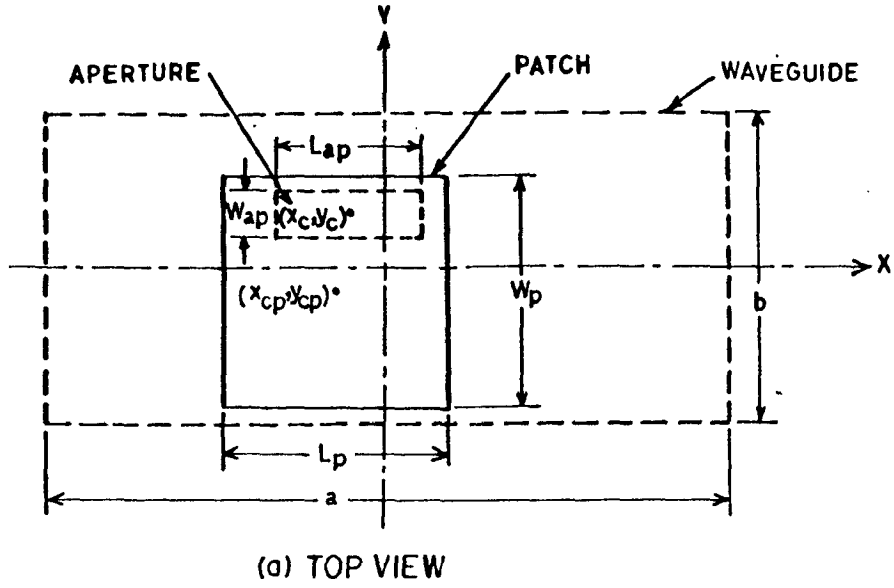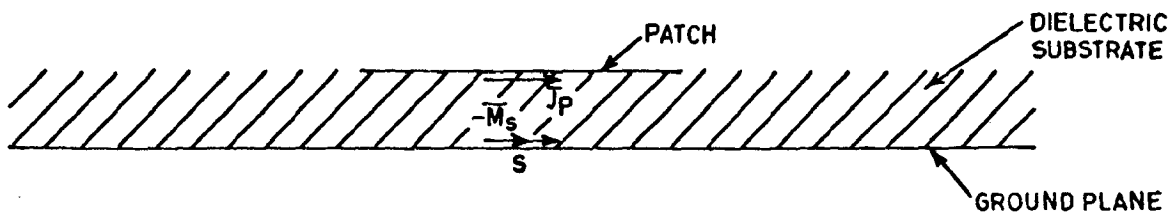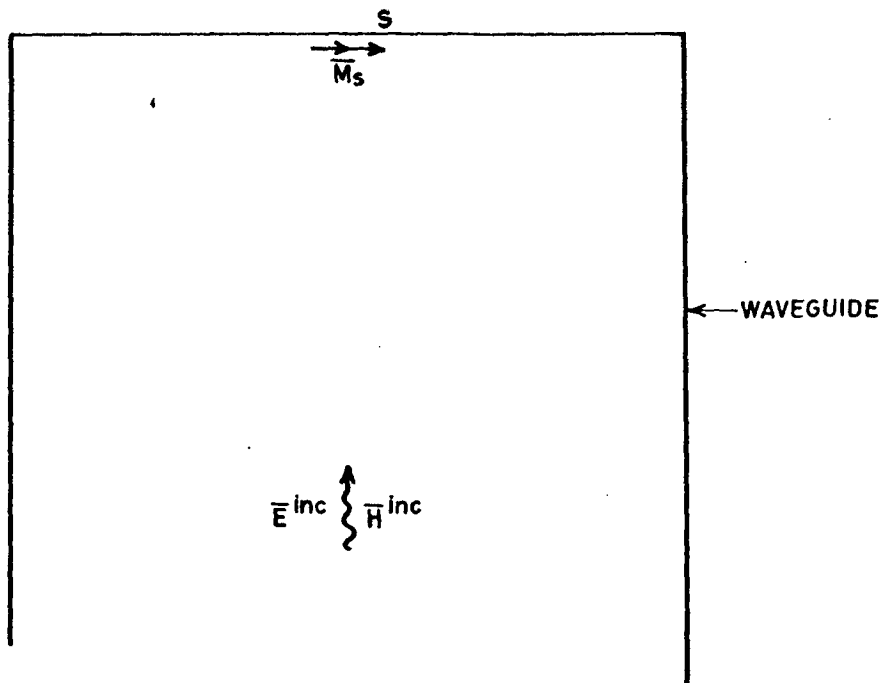WAVEGUIDE

$\bar{E}^{inc}$ $\bar{H}^{inc}$

(b) SIDE VIEW

Fig.2.2: Geometry of the original problem indicating various parameters and the coordinate system.

(a) Model valid for region 'b'
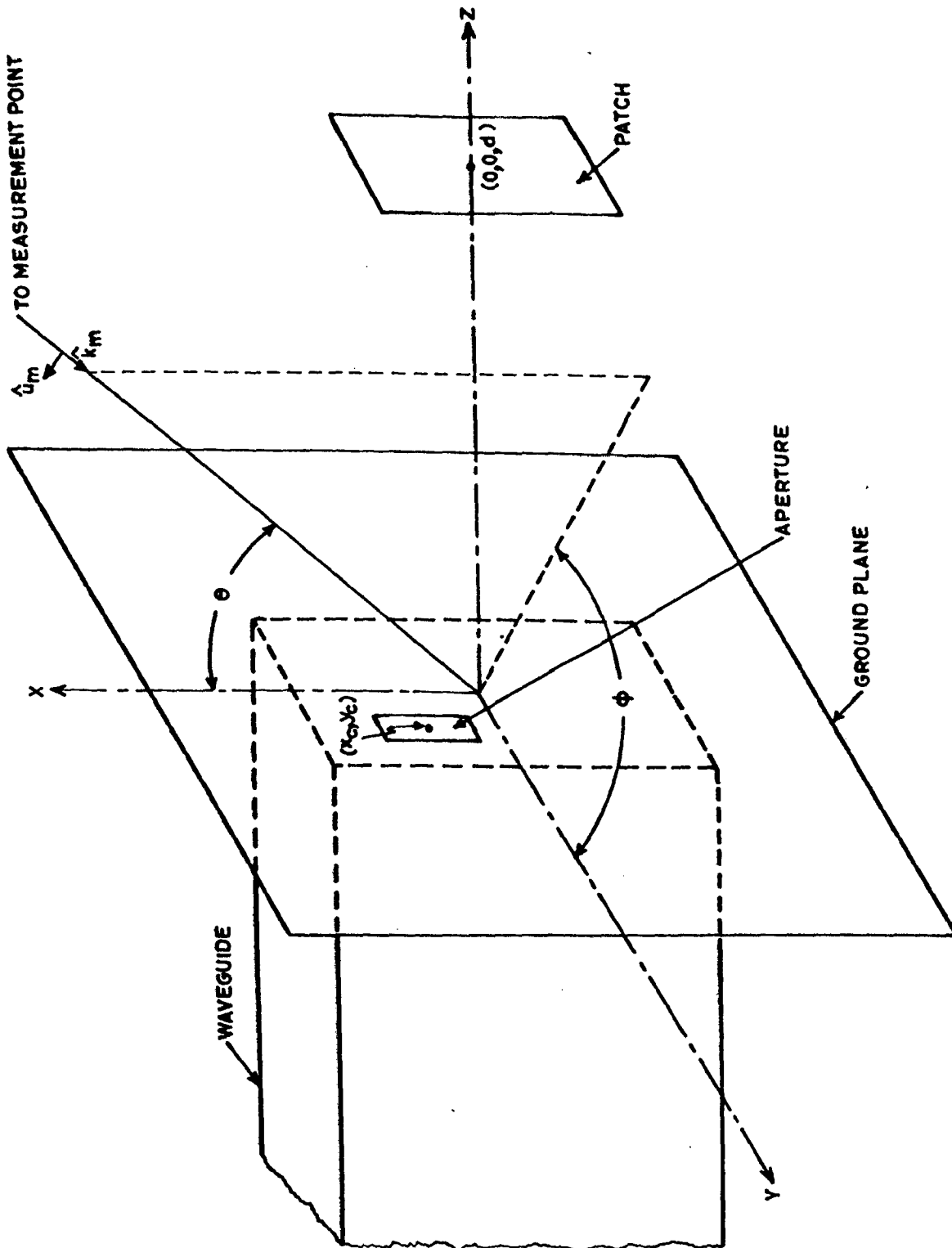

(b) Model valid for region 'a'

Fig. 2.3: Equivalent models.

49

Fig.2.4: Measurement vector geometry.

CHAPTER 3

NUMERICAL RESULTS

The analysis carried out in the previous chapter was implemented on a digital computer. The results obtained from this program were checked for the convergence and compared with the earlier published work [20,21]. For the purpose of comparison, different cases were considered, namely, an open waveguide radiating into free space with and without a reflector in front of it and an open waveguide radiating into a homogeneous medium of constitutive parameter $(\mu_o, \epsilon_o \epsilon_r)$. Finally, the program was used to generate test data for a patch antenna. In this chapter, the algorithm used to write the computer program has been explained with the help of flow charts and some numerical results are presented.

3.1 Numerical Considerations

Evaluation of the matrix elements for region 'b', namely, the elements of $[Z^b]$, $[Y^b]$, $[T^b]$ and $[C^b]$, requires the evaluation of integrals over α and β. One important consideration common to all these integrals is the presence of simple poles in the integrand. These are given by the zeros of T_e and T_m (Eqns. 2.70 and 2.71), which are functions of β alone (and not of α). These can be thought of as representing transverse electric (TE) and transverse magnetic (TM) surface wave poles, respectively, which are located in the complex β-plane.

From (2.68) and (2.69), we obtain

$$k_1^2 - k_2^2 = AC^2 \tag{3.1}$$

where

$$k_1^2 = \varepsilon_r k_o^2 - \beta^2 \; ; \quad k_2^2 = k_o^2 - \beta^2 \quad \text{and} \quad AC^2 = (\varepsilon_r - 1)k_o^2$$

In order to determine the roots of T_e, k_2 is substituted from (2.70) in (3.1), giving the characteristic equation

$$\sqrt{(AC)^2 - (k_1 d)^2} + k_1 d \, \cot(k_1 d) = 0 \tag{3.2}$$

Similarly, the characteristic equation for finding the roots of T_m, is obtained by substituting k_2 from (2.71) in (3.1) and is given by

$$-\varepsilon_r \sqrt{(AC)^2 - (k_1 d)^2} + k_1 d \, \tan(k_1 d) = 0 \tag{3.3}$$

Solution of the above equations yields the values of k_1, from which β can be determined. It has been shown by previous workers [22] that the number of poles is given by

$$N_{TE} = \begin{bmatrix} 0 & ; \quad \text{for} \quad AC < \pi/2 \\ n & ; \quad \text{for} \quad (n-\tfrac{1}{2})\pi < AC < (n+\tfrac{1}{2})\pi \end{bmatrix} \tag{3.4}$$

$$N_{TM} = n+1 \; ; \quad \text{for} \quad n\pi < AC < (n+1)\pi \tag{3.5}$$

where N_{TE} and N_{TM} are, respectively, the number of TE and TM surface wave poles. Since the first TM surface wave pole has a zero cutoff frequency, there is always at least one surface wave pole (unless $\varepsilon_r = 1$) [23]. These poles occur for real values of $\beta = \beta_{oi}$ such that $k_o \leq \beta_{oi} < \sqrt{\varepsilon_r} k_o$, if $\tan \delta = 0$ (no loss).

If dielectric loss is present, the poles move off the real axis to $\beta = \beta_{oi} - j\gamma$, $\gamma > 0$. To avoid numerical difficulties while integrating over β, the integration in the immediate vicinity of the poles is performed analytically. For example, if one TE and one TM pole are present at $\beta_1 = \beta_{o1} - j\gamma$ and $\beta_2 = \beta_{o2} - j\gamma$, respectively, then the integral given by (2.96) can be written in the form

$$\int_{\alpha=0}^{\pi/2} \int_{\beta=0}^{\infty} (\ ) \, d\beta \, d\alpha = \int_{\alpha=0}^{\pi/2} \left\{ \int_{\beta=0}^{\beta_{o1}-\delta} (\ ) \, d\beta + \int_{\beta_{o1}-\delta}^{\beta_{o1}+\delta} (\ ) \, d\beta \right.$$

$$\left. \int_{\beta_{o1}+\delta}^{\beta_{o2}-\delta} (\ ) \, d\beta + \int_{\beta_{o2}-\delta}^{\beta_{o2}+\delta} (\ ) \, d\beta + \int_{\beta_{o2}+\delta}^{\infty} (\ ) \, d\beta \right\} \, d\alpha \qquad (3.6)$$

The second and the fourth integral on the right-hand side of (3.6) can be written as

$$I_{\delta 1} = \int_{\beta_{o1}-\delta}^{\beta_{o1}+\delta} (\ ) \, d\beta = \int_{\beta_{o1}-\delta}^{\beta_{o1}+\delta} \frac{f_1(\beta)}{T_m(\beta)} \, d\beta \qquad (3.7)$$

and

$$I_{\delta 2} = \int_{\beta_{o2}-\delta}^{\beta_{o2}+\delta} (\ ) \, d\beta = \int_{\beta_{o2}-\delta}^{\beta_{o2}+\delta} \frac{f_2(\beta)}{T_e(\beta)} \, d\beta \qquad (3.8)$$

where $f_1(\beta)$ and $f_2(\beta)$ represent the non-singular portions of the integrand.

To evaluate the integral in the vicinity of a pole say $I_{\delta 1}$, the function $T_m(\beta)$ is expanded in a Taylor series around its zero, β_1. Thus, the equation (3.7) can be written as

$$I_{\delta 1} = f(\beta_1) \int_{\beta_{ol}-\delta}^{\beta_{ol}+\delta} \frac{1}{T_m(\beta_1)+(\beta-\beta_1)T'_m(\beta)\Big|_{\beta_1}+\cdots} \, d\beta \qquad (3.9)$$

where prime indicates differentiation with respect to β.
Considering only two terms in the Taylor series expansion and noting that $T_m(\beta_1) = 0$, we get

$$I_{\delta 1} = \frac{f(\beta_1)}{T'_m(\beta_1)} \int_{\beta_{ol}-\delta}^{\beta_{ol}+\delta} \frac{1}{(\beta-\beta_1)} \, d\beta \qquad (3.10)$$

which may be readily integrated to get

$$I_{\delta 1} = \frac{f(\beta_{ol}-j\gamma)}{T'_m(\beta_{ol}-j\gamma)} \ln \left\{\frac{\delta+j\gamma}{-\delta+j\gamma}\right\} \qquad (3.11)$$

(3.11) can be written in the form

$$I_{\delta 1} = \frac{f(\beta_{ol}-j\gamma)}{T'_m(\beta_{ol}-j\gamma)} \ln [re^{j\theta}] \qquad (3.12)$$

with

$$r = 1$$

$$\theta = \tan^{-1}\left\{\frac{-2\gamma\delta}{\gamma^2-\delta^2}\right\} \qquad (3.13)$$

Substituting (3.13) in (3.12) and simplifying, we get

$$I_{\delta 1} = \frac{j\,f(\beta_{ol}-j\gamma)}{T'_m(\beta_{ol}-j\gamma)} \tan^{-1}\left\{\frac{-2\gamma\delta}{\gamma^2-\delta^2}\right\} \qquad (3.14)$$

For the no loss case, which has been assumed in the present analysis, (3.14) reduces to

$$I_{\delta 1} = \frac{-j\pi \; f(\beta_{ol})}{T'_m(\beta_{ol})}$$

(3.15)

The integration in the vicinity of a TE pole can be carried out in a similar manner.

The integration from 0 to the first pole, in between the poles and after the last pole upto ∞ has been carried out numerically, using the N-point Gauss quadrature technique (Fig. 3.1). The convergence has been assumed to occur when the value of an element changes by less than 0.5% over an integration interval of $10k_o$. This usually occurs in the range $100k_o \leq \beta \leq 200k_o$.

3.2 Computer Program

Figs. 3.2 through 3.12 explain the logic used to develop the computer program. For convenience, the program has been broken up into a number of subroutines which are called from the main program. The data, such as the dimensions of the waveguide, patch and aperture, the dielectric constant and the thickness of the dielectric slab, etc., are read in the subroutine READAT. All the data are read in terms of wavelength, and are then converted in terms of the operating wavenumber (k_o) in the subroutine PROCES, which also computes the intermediate results required in the other subroutine by calling STORE. The computation of the zeros of T_e and T_m is carried out in the subroutine ROOT, using the Newton-Raphson method. The method requires an initial guess, which is accepted at this stage by the computer. The subroutines ZMN, TIN and

YBIJ, respectively, compute the elements of the matrices $[Z^b]$, $[T^b]$ and $[Y^b]$. These subroutines call the integration routine GQN, which performs the integration using N-point Gauss quadrature technique. Depending on the origin of the call for this routine, different functions are used as the integrand. When the dielectric constant is unity, no poles are encountered and hence a direct integration in two dimensions is carried out to evaluate the matrix elements using the subroutine GQER1. It is worth noting here that, due to the symmetry of the Green's function and the use of Galerkin's method, only one row of $[Z^b]$ and $[Y^b]$ matrices need to be computed. The other elements are filled up using the elements of this row. The elements of the matrix $[C^b]$ are obtained from $C^b_{ij} = -T^b_{ji}$. A call to the subroutine YAIJ results in the computation of the elements of the matrix $[Y^a]$ and the excitation vector $[\vec{I}^i]$. In this case, only the lower triangular part of $[Y^a]$ is computed and the remaining elements are filled up using these elements. Finally, the subroutine RESULT stores these intermediate matrices in a one dimensional array, which is inverted using the subroutine INVRT. The inverted matrix is used to compute the complex coefficients of the currents on the patch and the aperture, which are then used for the computation of antenna parameters.

3.3 Convergence of the Procedure

The convergence of the imaginary part of the self impedance of a microstrip antenna is shown in Fig. 3.13 as a function of β/k_o. For comparison, the results obtained by

Pozar [21] are also plotted in the same figure. These results
were obtained by using a 10-point Gauss quadrature routine with
the effective dielectric constant taken as $e_{re} = (e_r+1)/2$.
The real part of the self impedance converged to 0.1666 very
fast ($\beta/k_o < 10$). It was also found that increasing the number
of points for integration does not change the results appre-
ciably.

To check the convergence of other parameters, we have
considered the following four situations.

1. An open waveguide, ($a=L_{ap}=7.5mm$; $b=W_{ap}=1.5mm$),radiating
   into free space.

2. An open waveguide, ($a=L_{ap}=22.86mm$; $b=W_{ap}=10.16mm$),
   radiating into free space.

3. An open waveguide, ($a=L_{ap}=22.86mm$; $b=W_{ap}=10.16mm$),
   radiating into a homogeneous medium of dielectric
   constant, $e_r = 2.2$.

4. An open waveguide, ($a=L_{ap}=22.86mm$; $b=W_{ap}=10.16mm$),
   with a reflector (or patch), ($L_p=12mm$; $W_p=9mm$), in
   front of it, at a distance $d=1.5mm$, such that the
   centre of the reflector coincided with the axis of
   the waveguide and radiating into free space.

In all the four cases, the open end of the waveguide was assumed
to be terminated in an infinite ground plane and the operating
frequency was 10 GHz.

The convergence of the reflection coefficient for Case 1, as a function of the number of subsections over the aperture along the x direction, L_x, is shown in Fig. 3.14. The number of subsections along y direction, L_y, has been chosen to be unity. It is seen that the results obtained by the present procedure, using piecewise sinusoidal (PWS) functions, show oscillatory behaviour. For comparison, the results obtained by Sinha [20] are also plotted in the same figure.

In order to determine the source of the oscillatory behaviour, a number of numerical tests were carried out on this problem. First, the numerical values of the elements of the matrix $[Y^a]$, obtained from the present method and the method of [20], were compared and found to be almost same. The small difference in numerical values can be attributed to the fact that rooftop (RT) functions have been utilised in [20] while PWS functions have been used in our case. This was confirmed by using RT functions in the present method. The reflection coefficient obtained from the present method using RT functions has also been plotted in the Fig. 3.13, which also shows oscillatory beghaviour. Thus, one may conclude that the matrix $[Y^a]$ is not responsible for the peculiar nature of the reflection coefficient in Fig. 3.14.

The elements of $[Y^b]$, on the other hand, obtained from the present method using PWS functions and from [20], were of the same order but having quite different numerical values. This discrepancy could be attributed to the numerical errors

introduced while performing the integration, and was confirmed by analytically taking the Fourier transform of a known function, $\exp(-|x|-|y|)$, and then evaluating the inverse Fourier transform using 12-point numerical integration. The real part in the results showed about one percent deviation from the expected results but the imaginary part, rather than being zero, was found to be of the order of 10^{-2}. When the number of points of integration was increased to 20, the accuracy of the results also improved. These tests confirmed the satisfactory functioning of the integration routine, apart from confirming the presence of slight numerical errors.

Since the reflection coefficient curve underwent sudden jumps for $L_x=11$ and 17, it was conjuctured that the ill-conditioning of the admittance matrix might be the cause for this behaviour. However, inspection of the condition number, $(\| [Y] \| . \| [Y]^{-1} \|)$ revealed that the matrix behaved well at these points too. An attempt was then made to study the behaviour of the error matrix, [ERR], given by

$$[ERR] = [Y^b_{ij}]_1 - [Y^b_{ij}]_2$$

where the subscripts 1 and 2 correspond to the present method with PWS functions and [20], respectively. We defined

$$N_{ERR} = \sqrt{\sum_{i,j} |[ERR]|^2}$$

for the error matrix. It was predicted that, any sudden change in the elements of [ERR] should be reflected in the value of

N_{ERR}. However, the values of N_{ERR} did not show any peculiar behaviour when L_x was 11 and 17.

Fig. 3.15 shows the normalized equivalent magnetic current on the aperture. The normalisation factor is the root-mean-square value of the incident field. That is, M has been normalized with respect to

$$\sqrt{\frac{1}{ab} \iint_{guide} |\bar{E}^{inc}|^2 \, dx \, dy}$$

where the integration is over the waveguide cross-section. The results obtained from this method using PWS functions are found to be in close agreement with those obtained from [20].

The radiation patterns obtained from this method, using PWS functions, and those obtained from [20] are shown in Fig. 3.16 where a good agreement between the two is seen. It may be noted that even at L_x=11 and 17, radiation patterns obtained from the two methods were in good agreement.

In the previous example, the dimensions of the waveguide and the frequency were such that only the evanescent modes could exist in it. As the next example, an open waveguide radiating into free space, with a propagating TE_{10} incident mode was considered (Case 2), for which the reflection coefficient, normalized equivalent magnetic current on the aperture and the radiation patterns are plotted in Figs. 3.17 through 3.19, respectively. Even in this case, the reflection coefficient shows a slightly oscillatory behaviour, but with a reduced

amplitude as L_x is increased. On the other hand, the equivalent magnetic current on the aperture and the radiation patterns obtained from this method using PWS functions are seen to be in close agreement with those obtained from [20].

The reflection coefficient is plotted in Fig. 3.20 as a function of L_x, for the case of a open waveguide radiating into a homogeneous medium (Case 3), and is found to be constant within the plotting accuracy. In this case, which was approximated by considering a very thick ($3\lambda_0$) dielectric slab to be present in front of the open waveguide, a large discrepancy is observed in the values of the reflection coefficient and the aperture current distribution (Fig. 3.21) obtained from the present method and those obtained from [20].

As a last example, the convergence of reflection coefficient for the case of an open waveguide radiating into free space with a reflector in front of it (Case 4) is shown in Fig. 3.22. The results of [20] show no convergence in reflection coefficient when the number of subsections along the y direction on the aperture is unity. This indicates that y-currents on the aperture and x-currents on the patch are to be considered in the analysis. Again in this case, the present procedure with PWS functions did not show convergence in the reflection coefficient when the number of subsections, along the y-direction, on the patch was increased (Fig. 3.22(b)). Figs. 3.23 and 3.24 show the distribution of normalized equivalent currents on the aperture and the patch, respectively.

The current over the patch is normalized with respect to the rms value of the incident magnetic field in the waveguide. In this case, a marked discrepancy was seen between the currents obtained by the present method with PWS functions and [20]. However, the radiation patterns (Fig. 3.25), obtained using the present method with PWS functions and [20] were in close agreement.

3.4 Waveguide Fed Patch Antenna

Although, the input reflection coefficient did not show any convergence, the program was used to study the variation of input impedance with frequency for a waveguide fed patch antenna.

We considered a patch, (L_p=9.189mm; W_p=11.8585mm), with aperture, (L_{ap}=11.43mm; W_{ap}=1.5mm), in the ground plane of a dielectric substrate of thickness 1.5mm and dielectric constant, ε_r=2.2, fed by a waveguide, (a=22.86mm; b=10.16mm), such that the centre of the patch coincided with the centre of the aperture and the axis of the waveguide. Fig. 3.26 shows the input characteristics, namely, the input VSWR and the real and the imaginary parts of the input impedance as a function of frequency using the effective dielectric constant ε_{re}=(ε_r+1)/2. A well pronounced parallel resonance is observed at 15.3 GHz. Although, another parallel resonance is observed around 26.2 GHz, it is not very well pronounced. Further, a series resonance is also seen to occur between the two parallel resonant points.

Several authors have mentioned that (2.39) is a better approximation for ϵ_{re}. So an effort was made to study the effect of this choice on the resonant frequency of the patch antenna. Fig. 3.27 is a plot of comparison of the input characteristics, around resonance, for the two choices of ϵ_{re}. Although the shape of the curves remains the same, the resonant frequency undergoes a definite shift when ϵ_{re} as given by (2.39) is used.

3.5 Summary

In this chapter, numerical considerations for the development of a computer program, for the analysis presented in the previous chapter, has been explained along with the logic flow diagrams. The results obtained from this program, apart from checking for the convergence, have been compared with the published work by considering different situations. Finally, test data has been presented for a waveguide fed patch antenna.
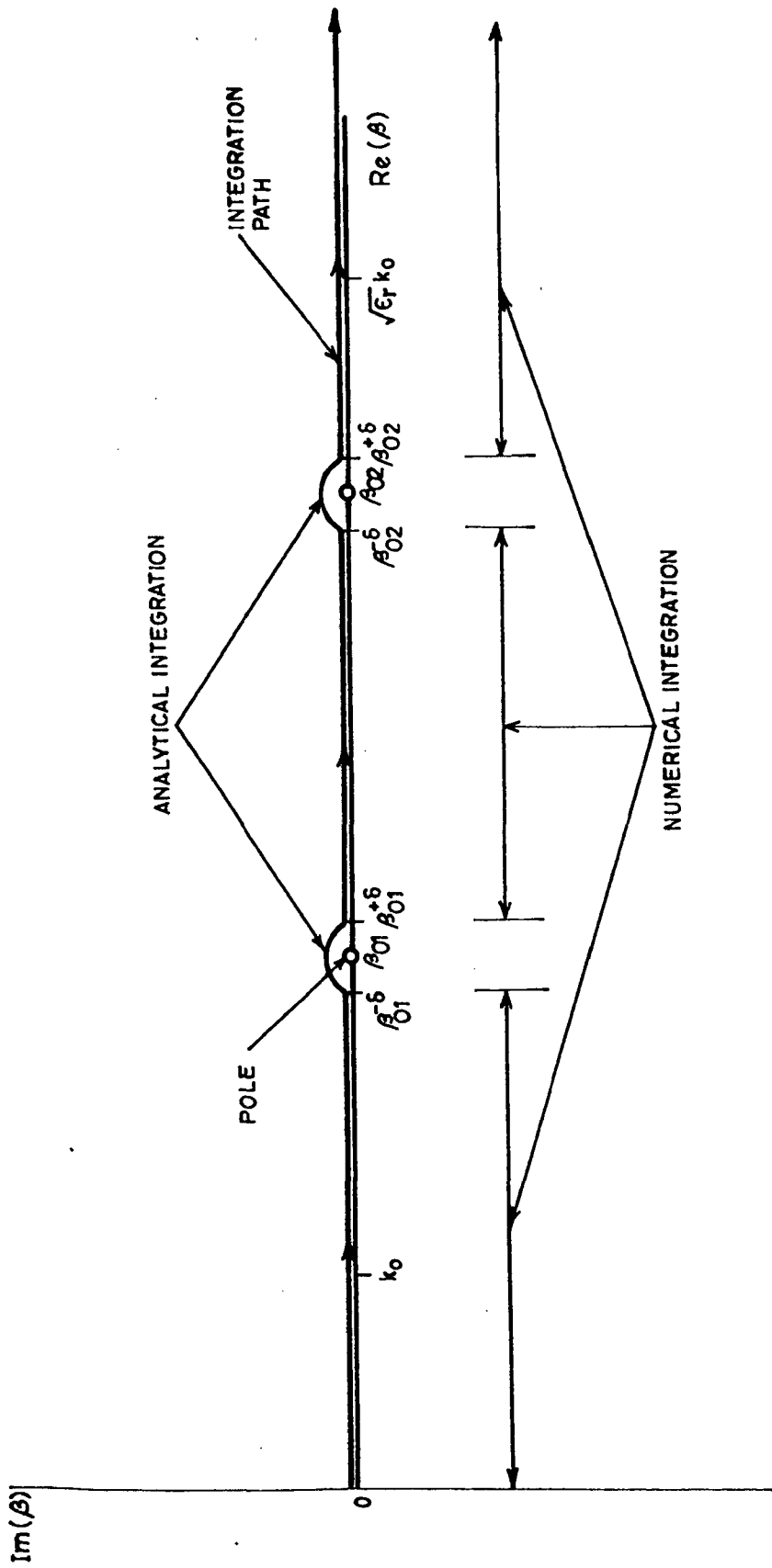
Fig. 3.1: Location of poles in the complex β plane and the path of integration.
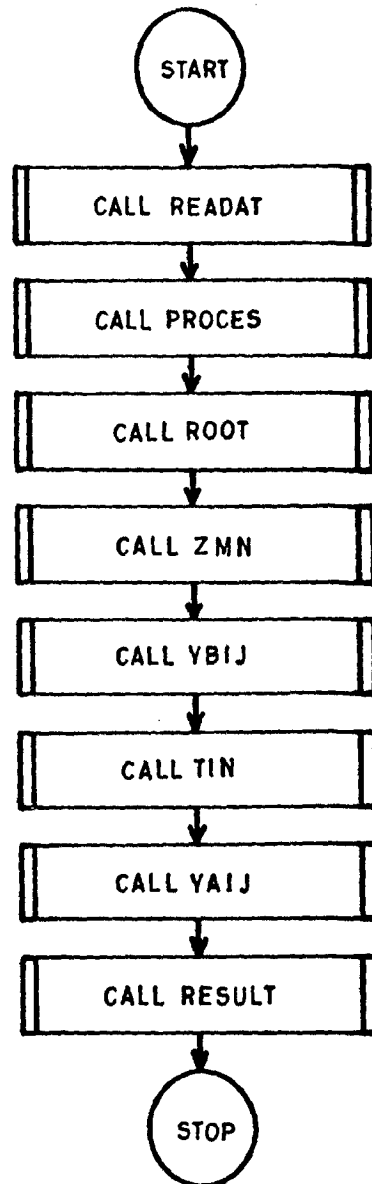
Fig.3.2:Main program.
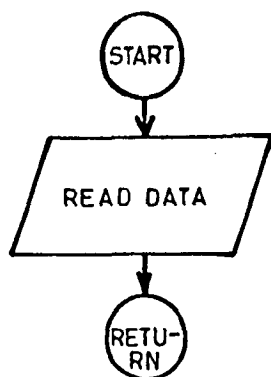
Fig.3.3:READAT.
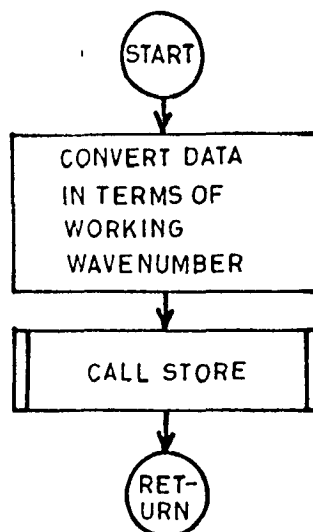
Fig.3.4:PROCES.

Fig.3.5:ROOT.

Fig.3.6:ZMN.

START

FUNC ← 'TXY'

IS $\epsilon_r = 1$?

NO   YES

CALL GQN

CALL GQER1

$C_{ni}^{b} \leftarrow -T_{in}^{b}$

RETU-RN

Fig.3.7: TIN.

START

FUNC ← 'YBXX'

INITIALISE INDICES FOR COMPUTATION OF ONE ROW OF $[Y^b]$

CALL GQN

FILL UP OTHER ROWS OF $[Y^b]$
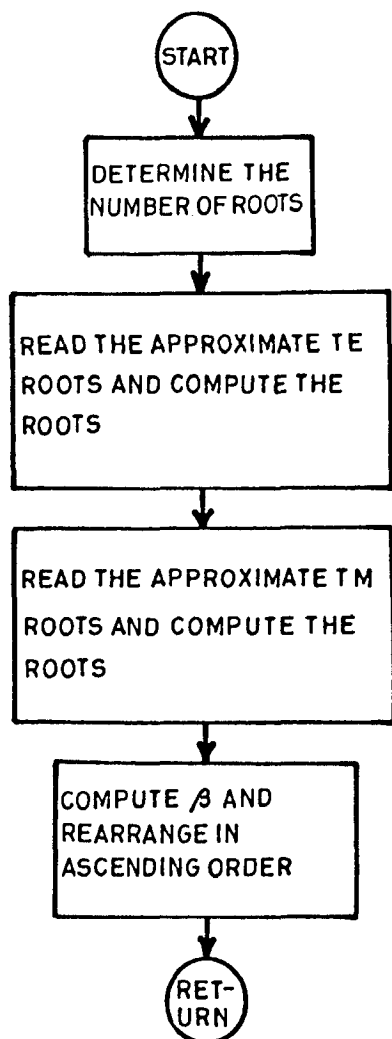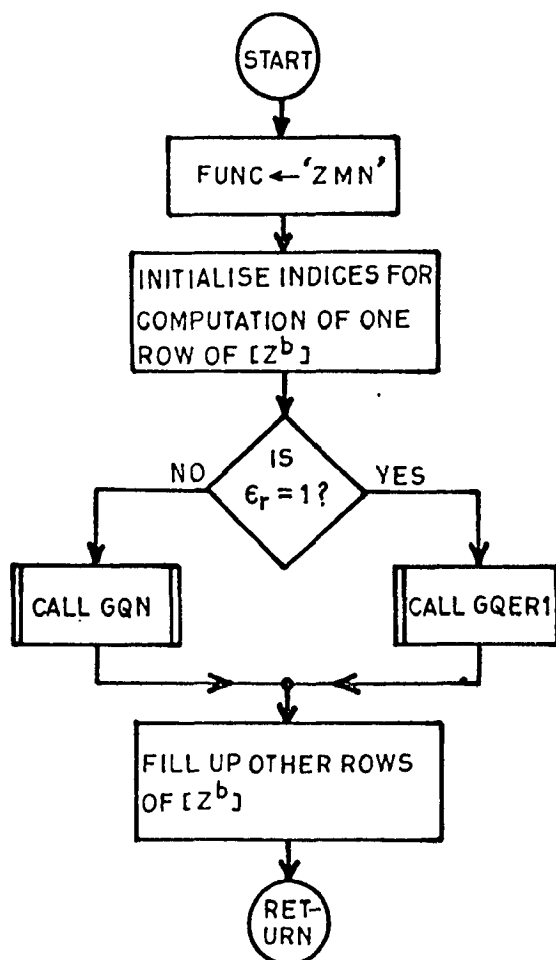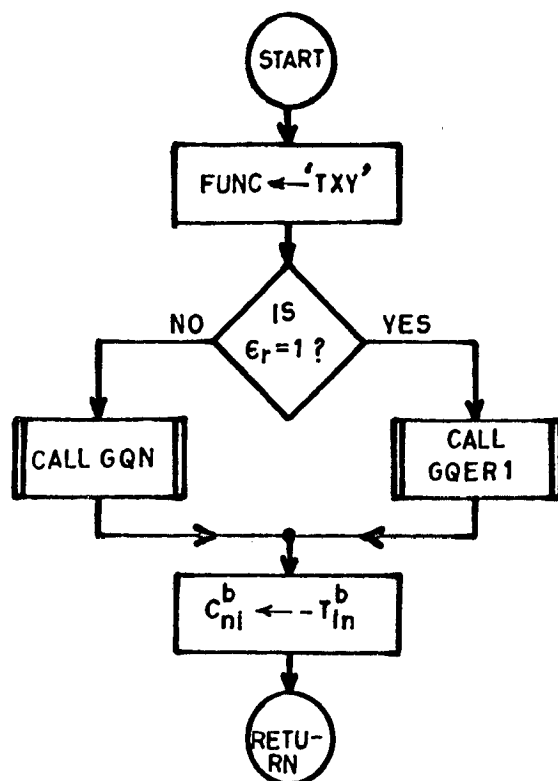
RETU-RN
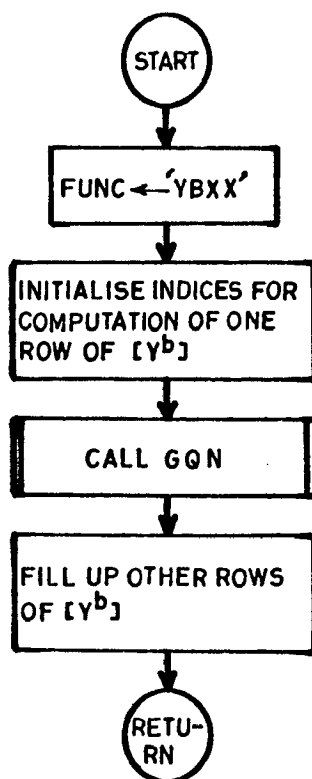
Fig.3.8: YBIJ.
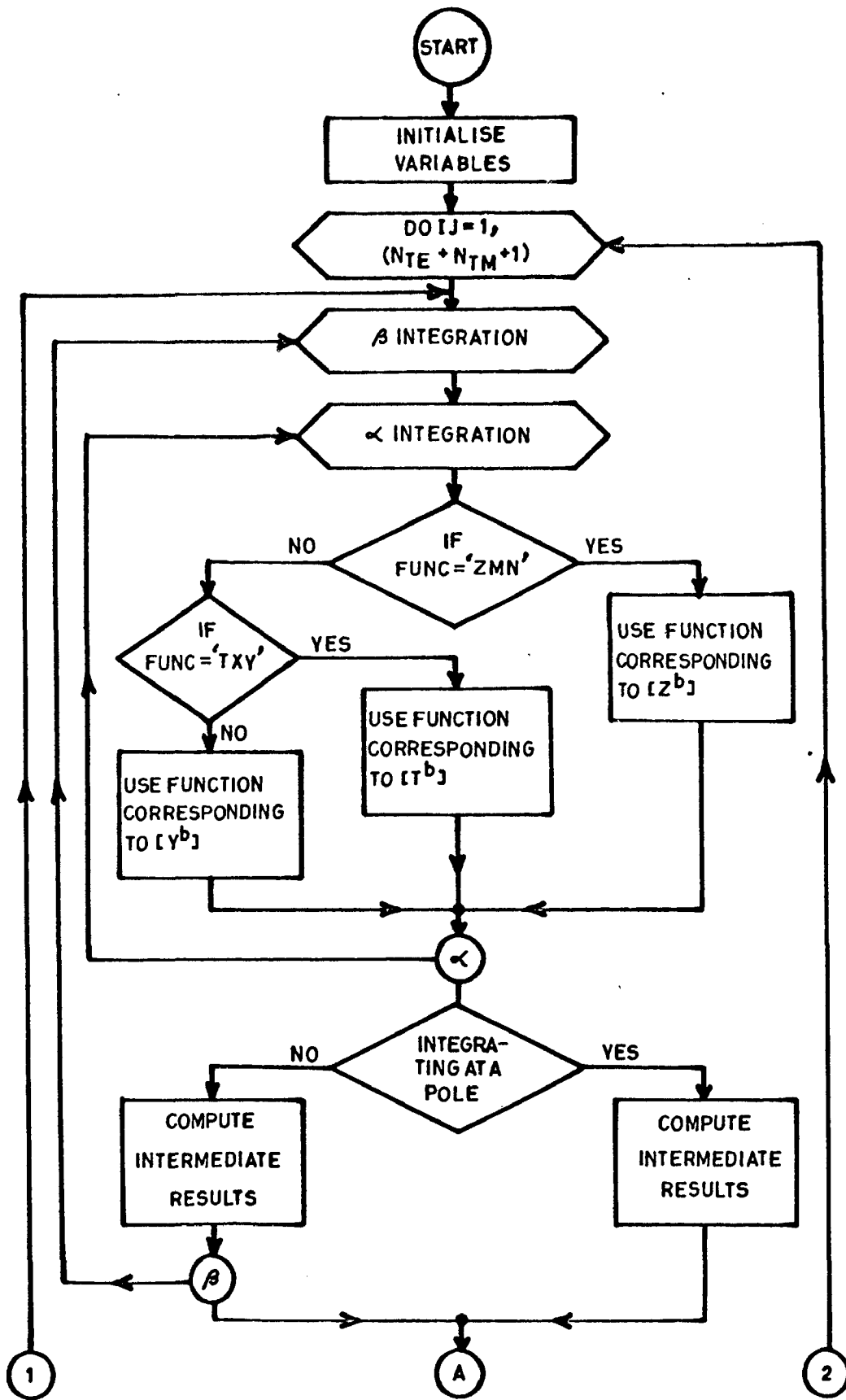
Fig. 3.9: G Q N.
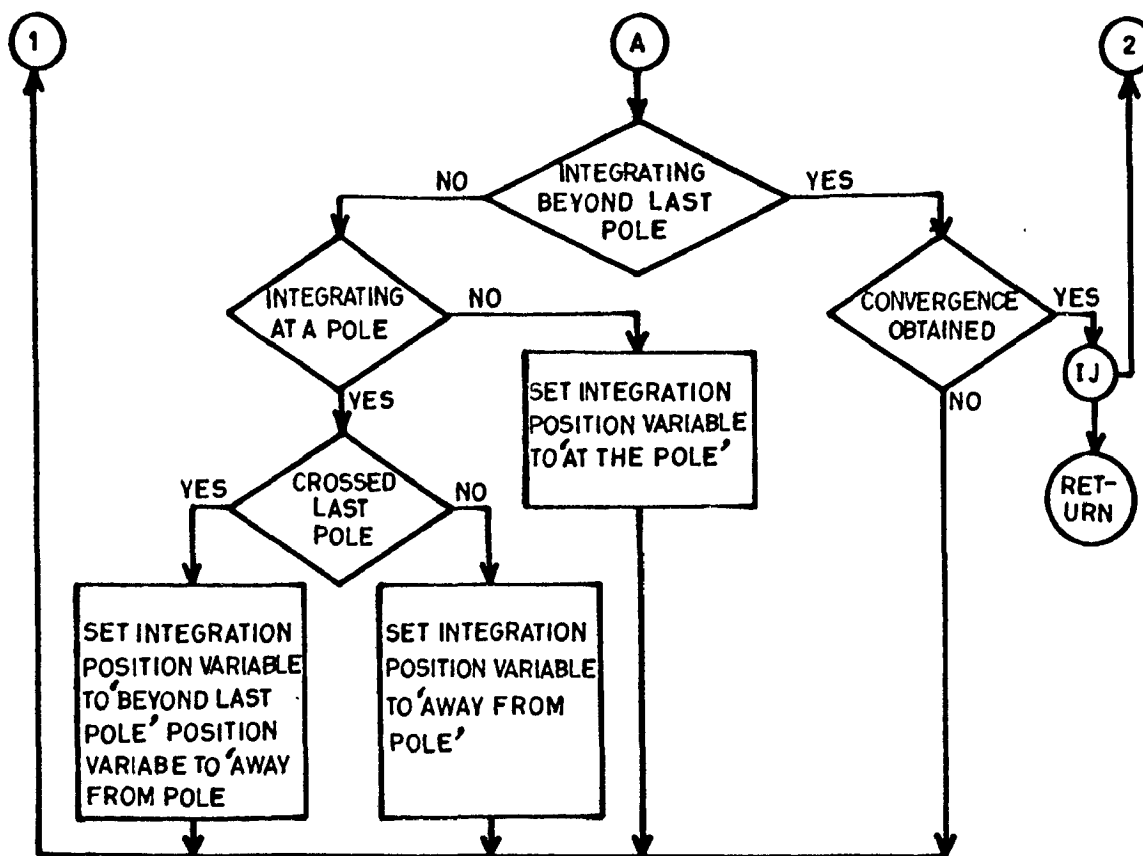
Fig. 3.9:(Continued).

Fig.3.10: GQER1.

START

COMPUTE THE LOWER TRIANGULAR PART OF $[Y^a]$, A_{lo} AND $[\overrightarrow{T}^i]$

FILL UP REMAINING ELEMENTS OF $[Y^a]$

RET-
URN

Fig.3.11: YAIJ.

START

STORE THE ELEMENTS OF INTERMEDIATE MATRIC-
ES COLUMN WISE IN THE FINAL MATRIX

INVERT THE FINAL MATRIX AND COMPUTE THE
COMPLEX COEFFICIENTS OF CURRENT EXPANSION
FUNCTION

COMPUTE ANTENNA PARAMETERS

RET-
URN
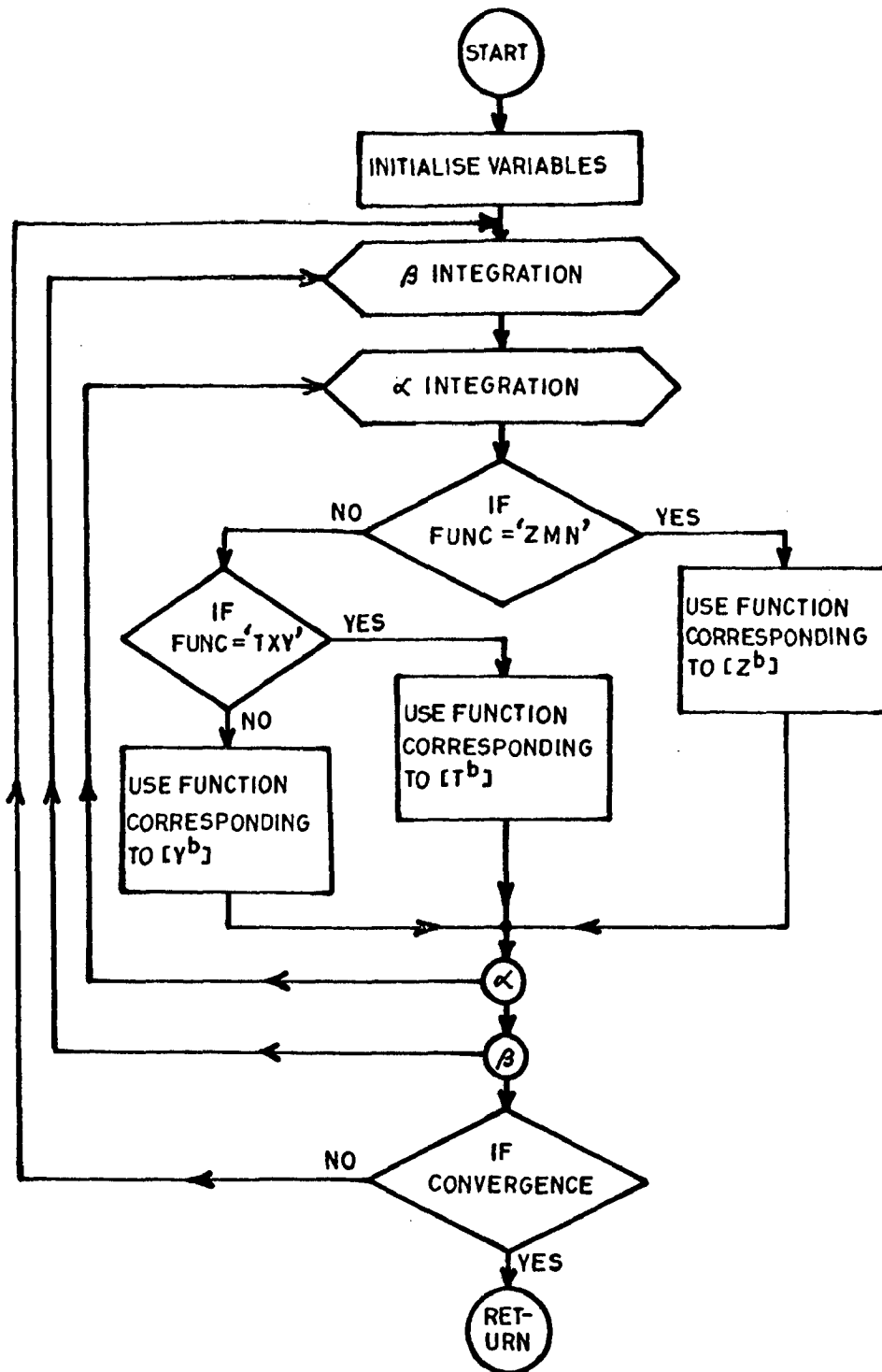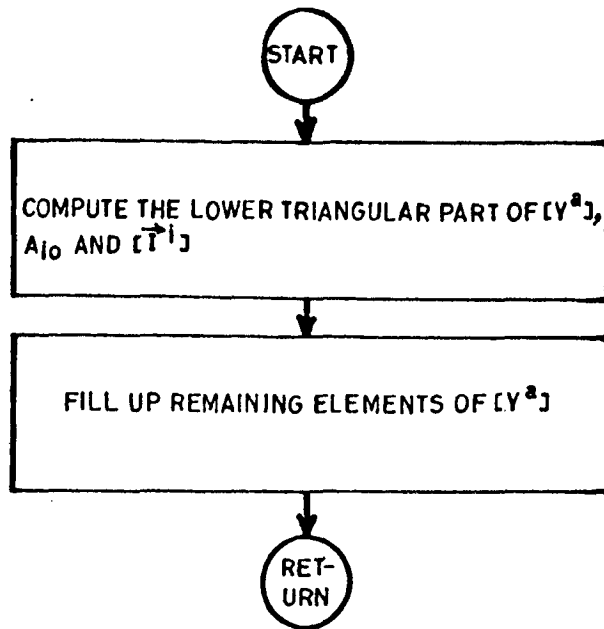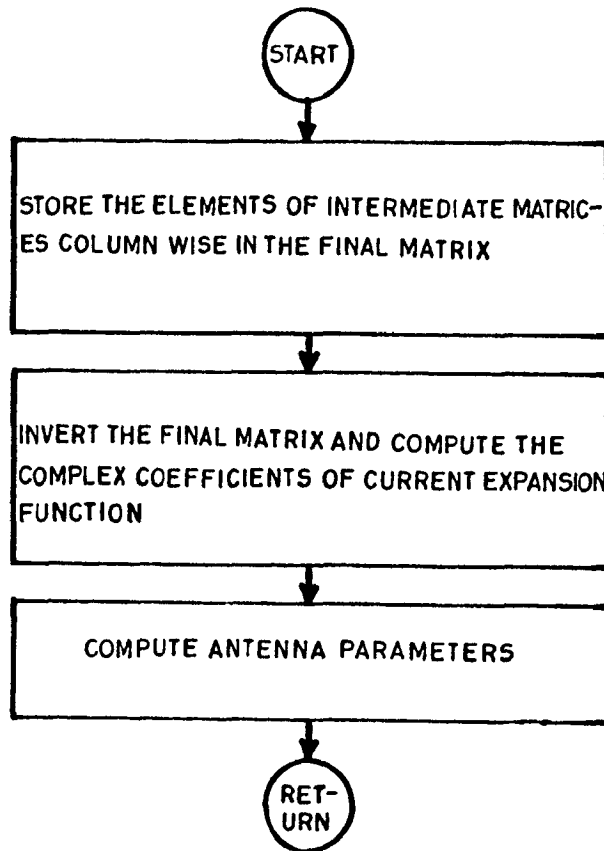
Fig.3.12 : Result.
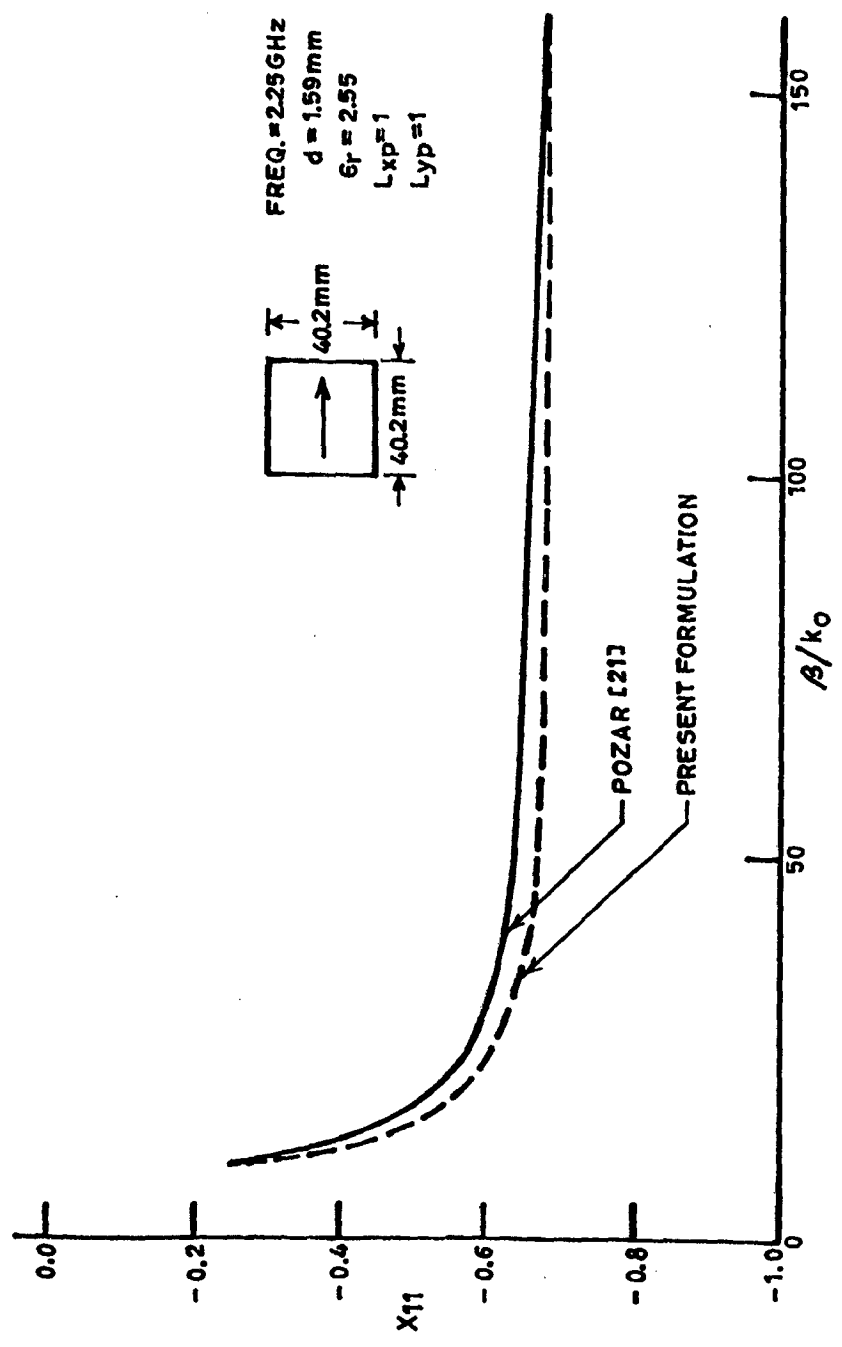
Fig.3.13:Convergence of the imaginary part of the self impedance of a microstrip patch antenna, $R_{11}=0.167\Omega$.
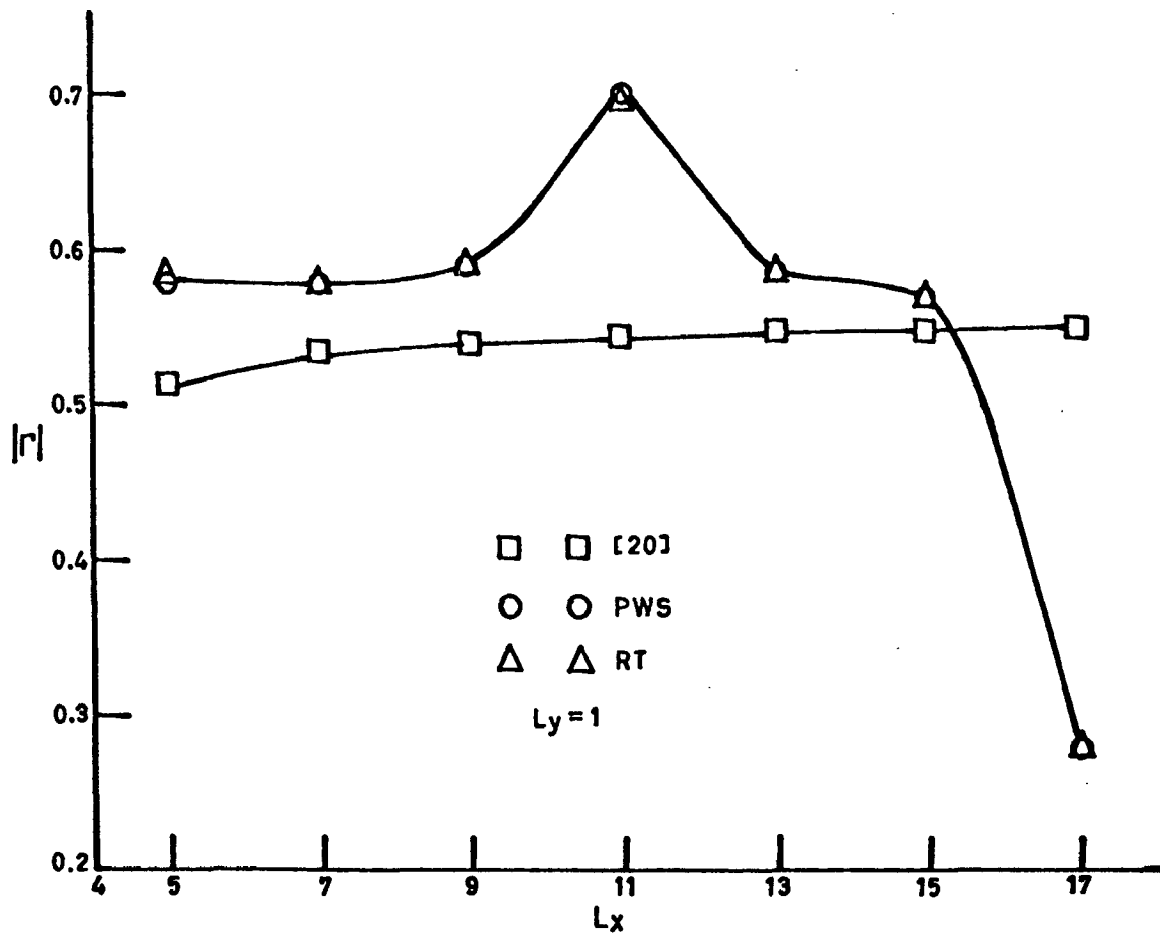
Fig.3.14:Convergence of reflection coefficient (Case1).
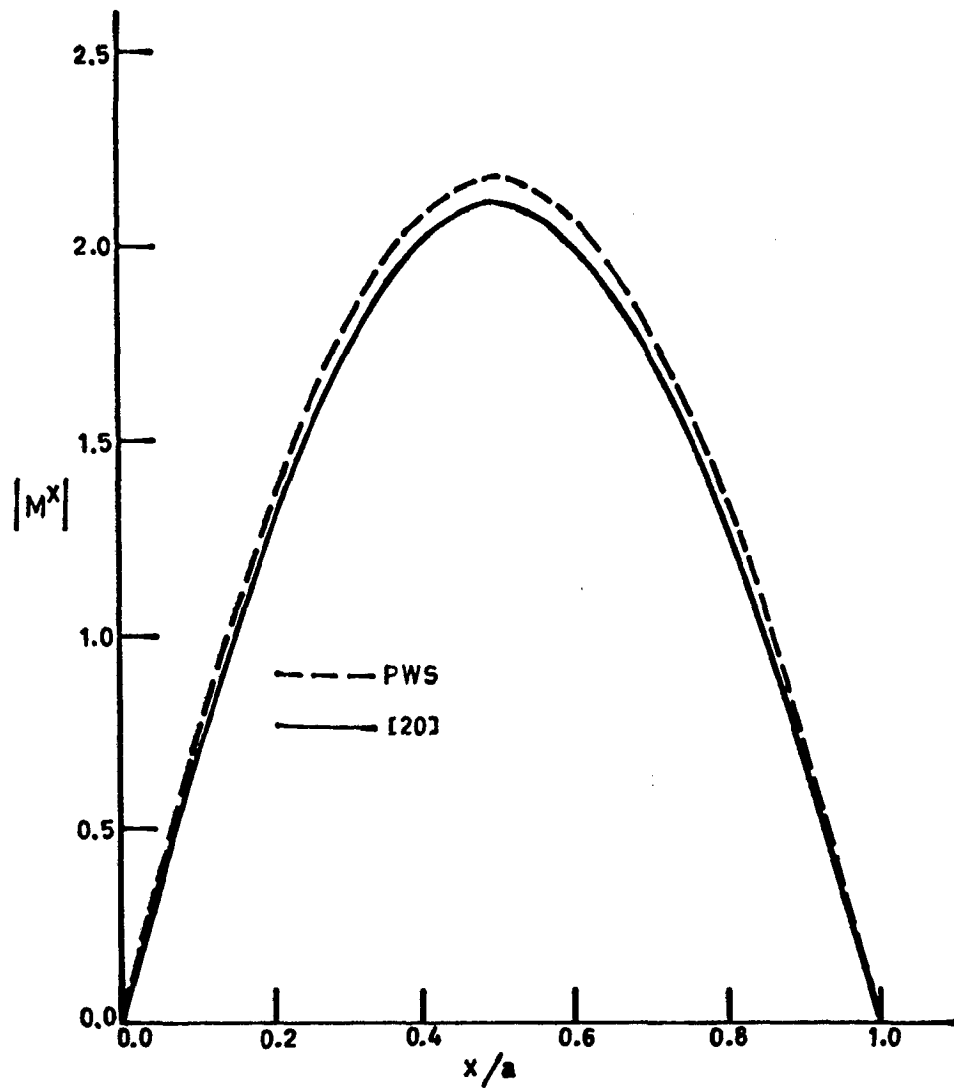
Fig.3.15: Distribution of normalized current on
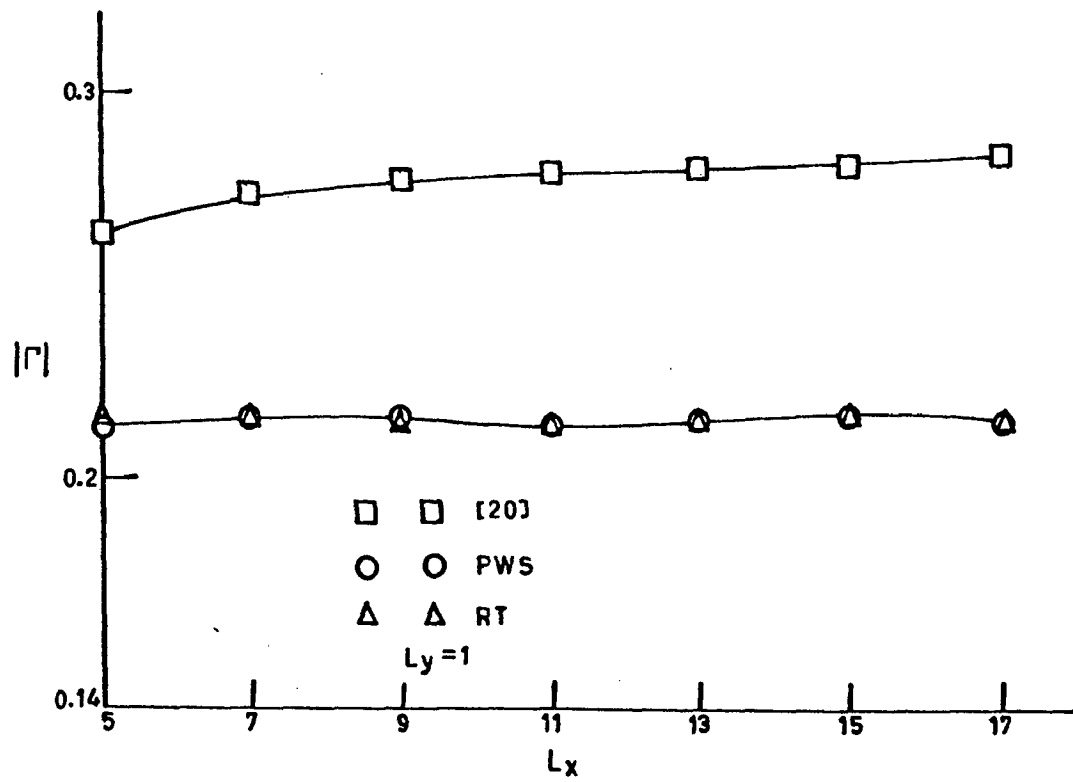the aperture (Case 1).
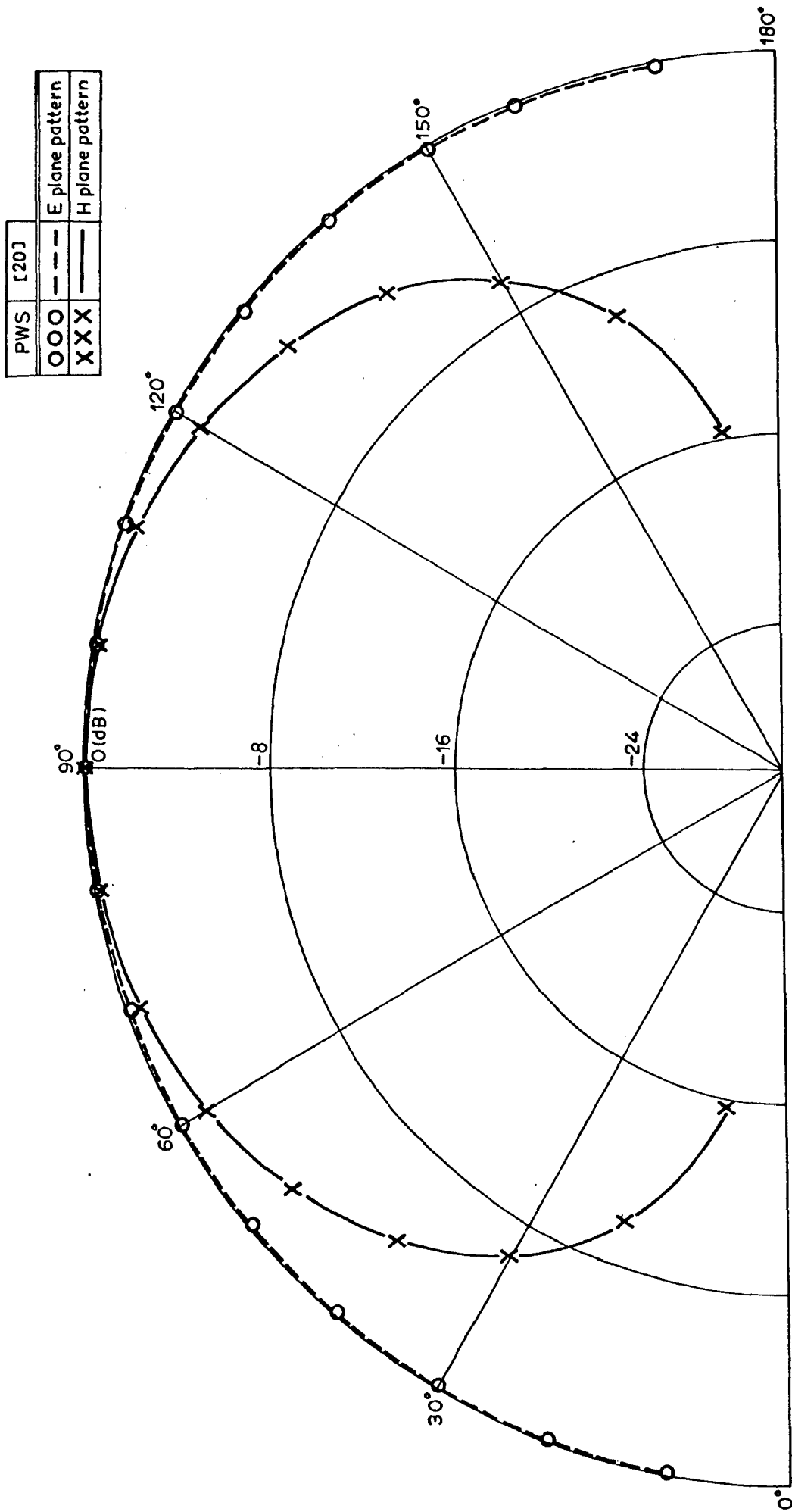
Fig.3.16:Radiation patterns (Case 1).

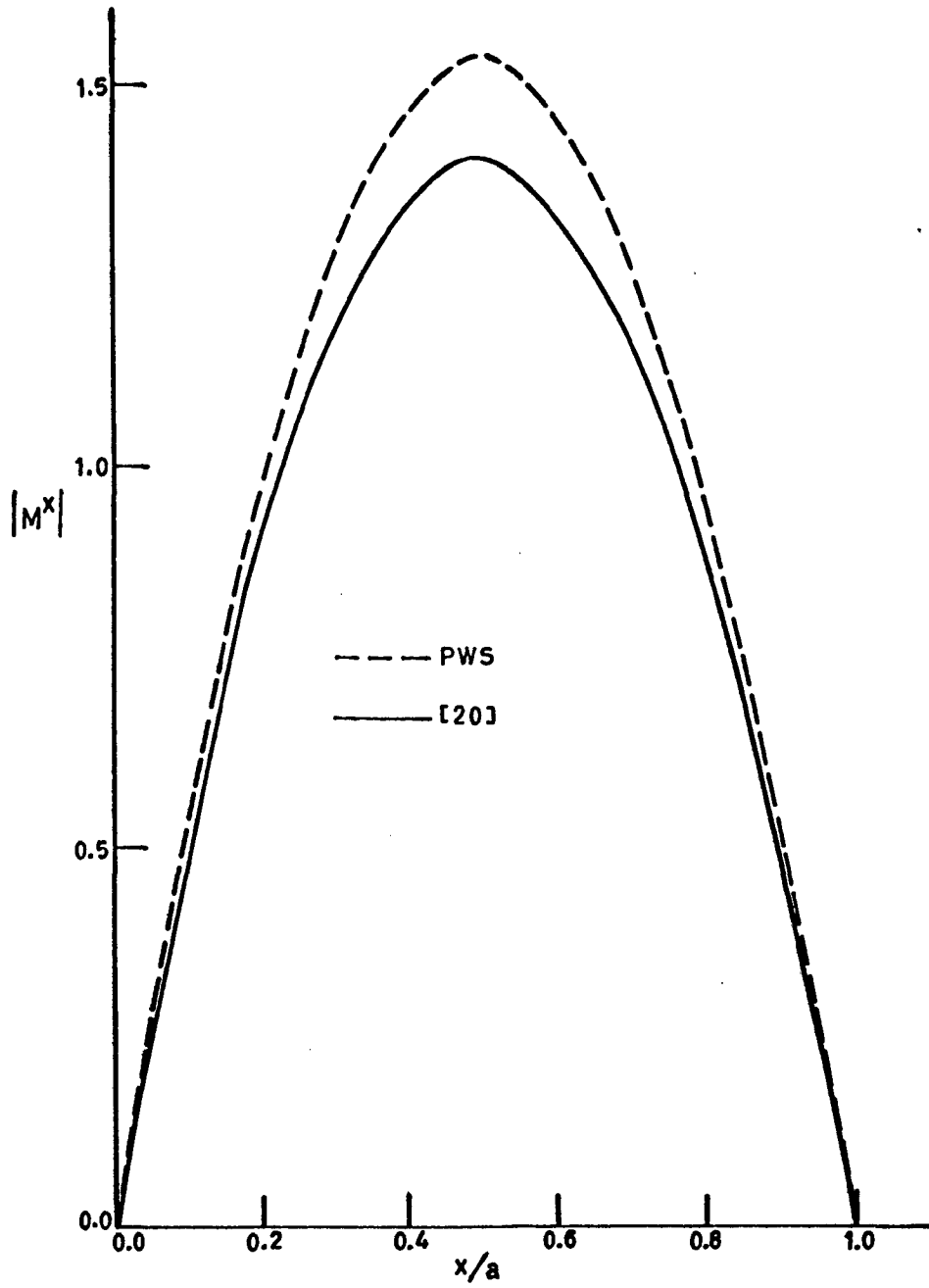Fig.3.17 : Convergence of reflection coefficient (Case 2).

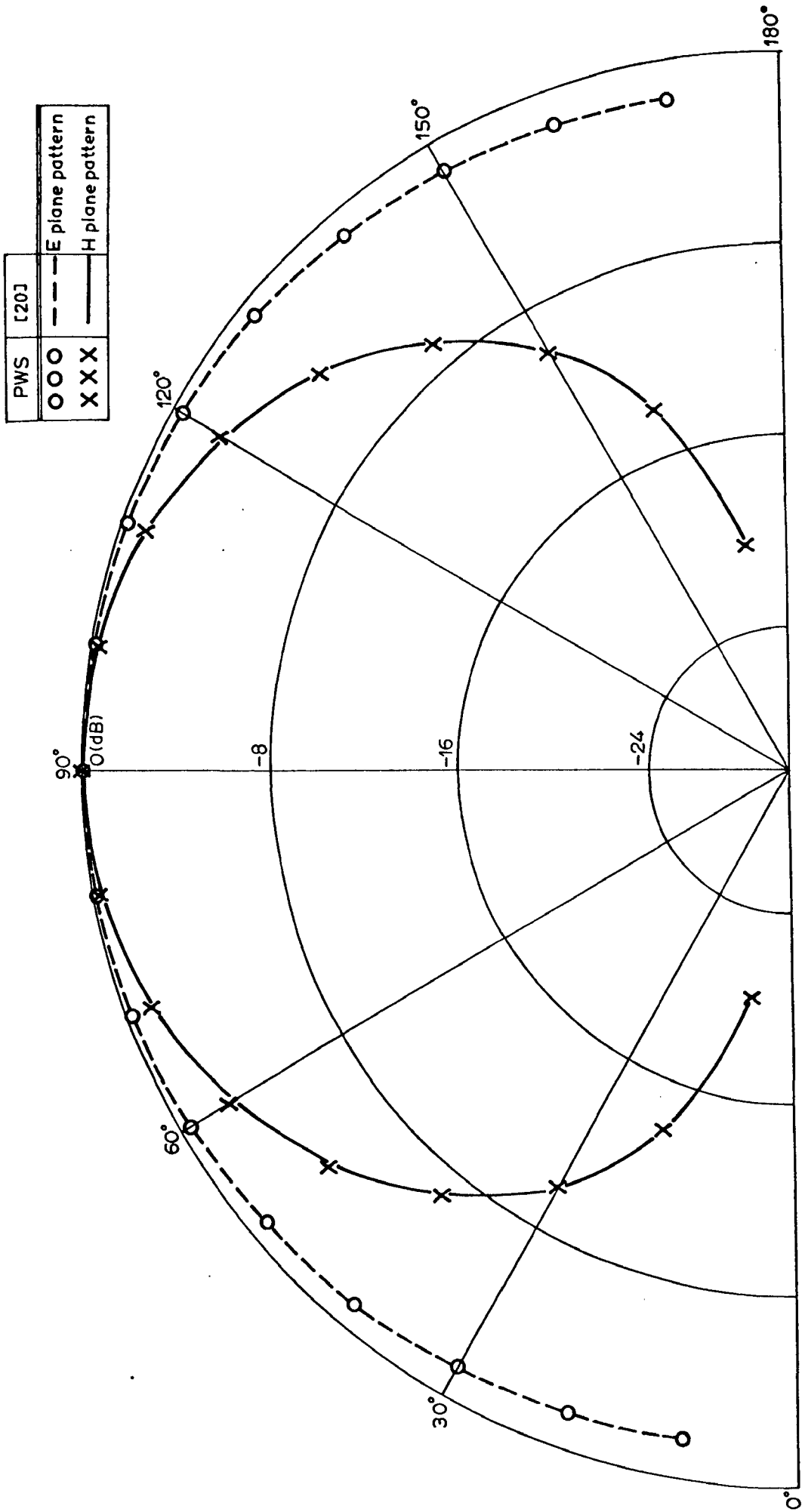Fig.3.18: Distribution of normalized current on the aperture (Case 2).

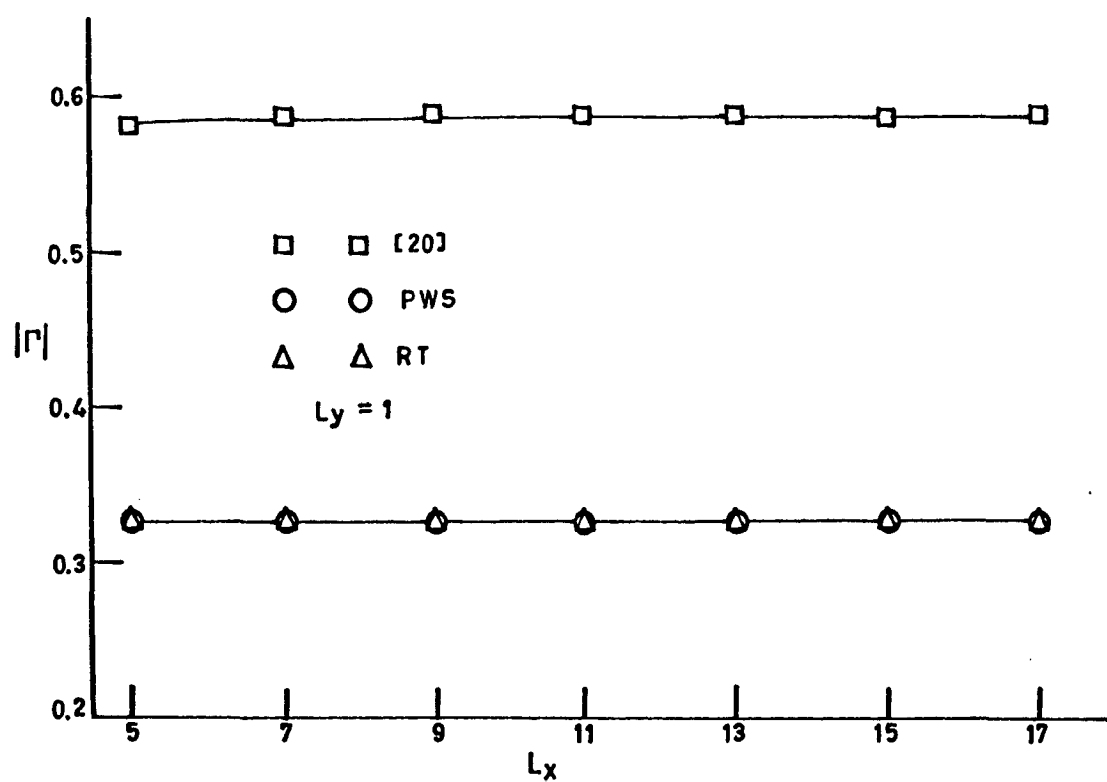| PWS	[20]	
O O O	– – – –	E plane pattern
X X X	———	H plane pattern

Fig.3.19: Radiation patterns (Case 2).

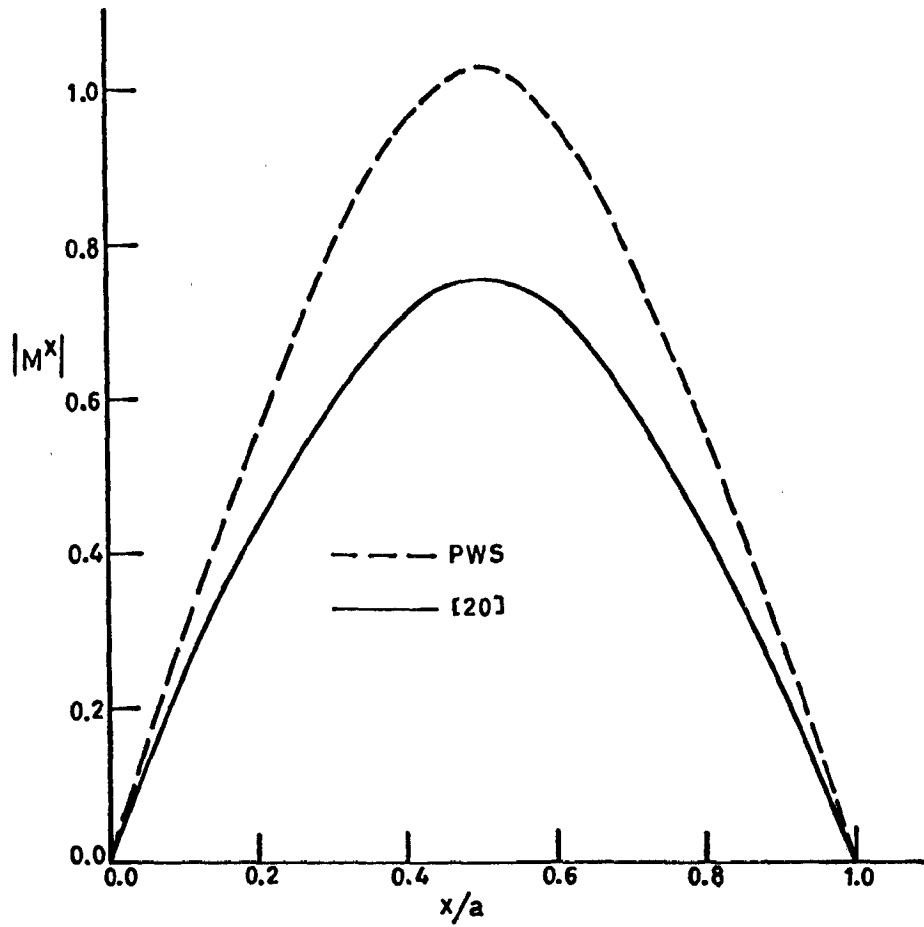Fig.3.20:Convergence of input reflection coefficient (Case3).

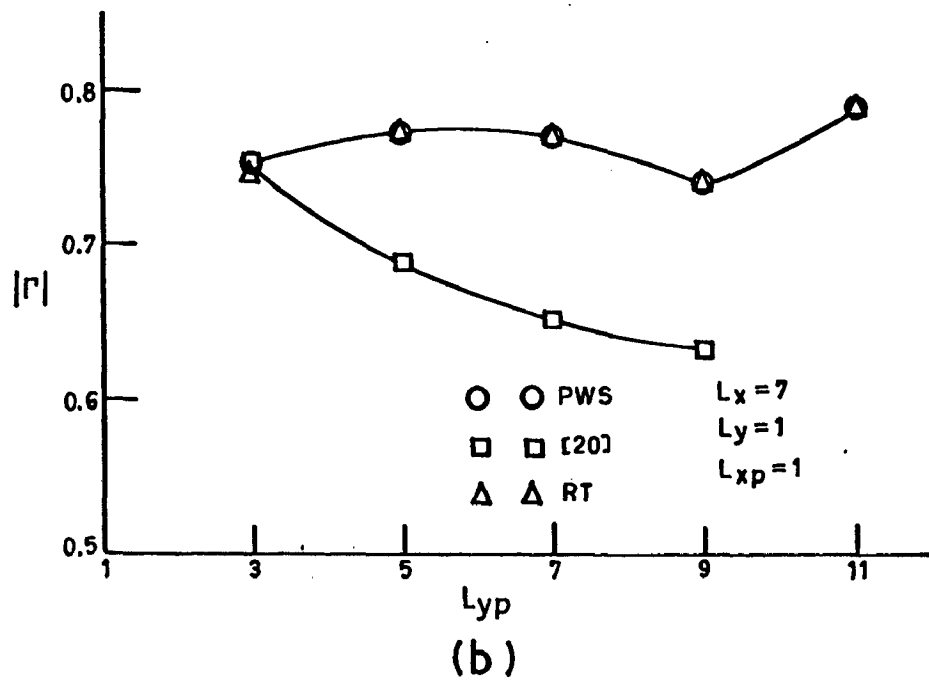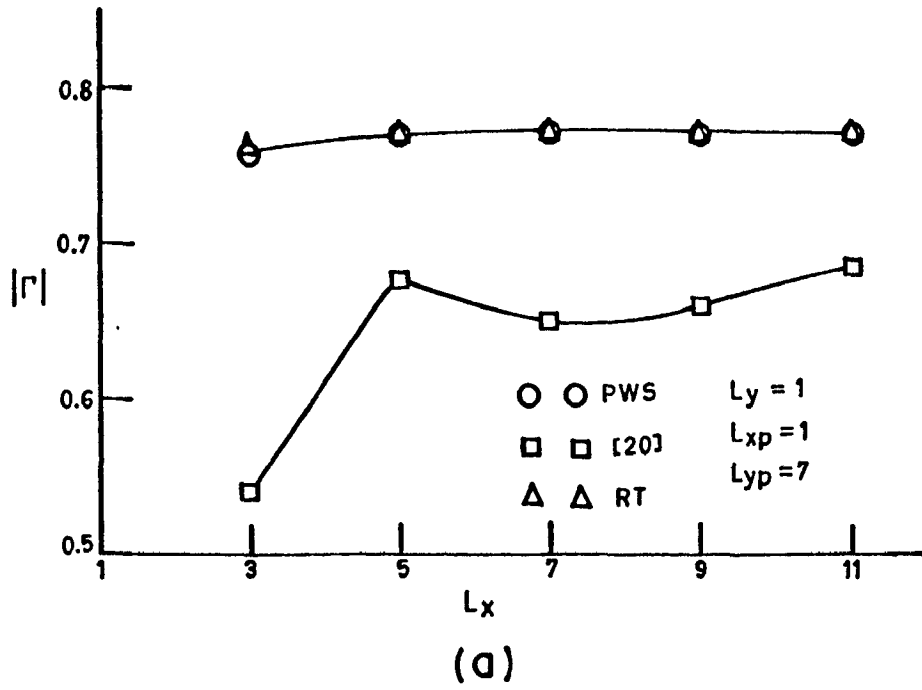Fig.3.21: Distribution of normalized aperture current (Case 3).

(a)

(b)

Fig.3.22: Convergence of reflection coefficient
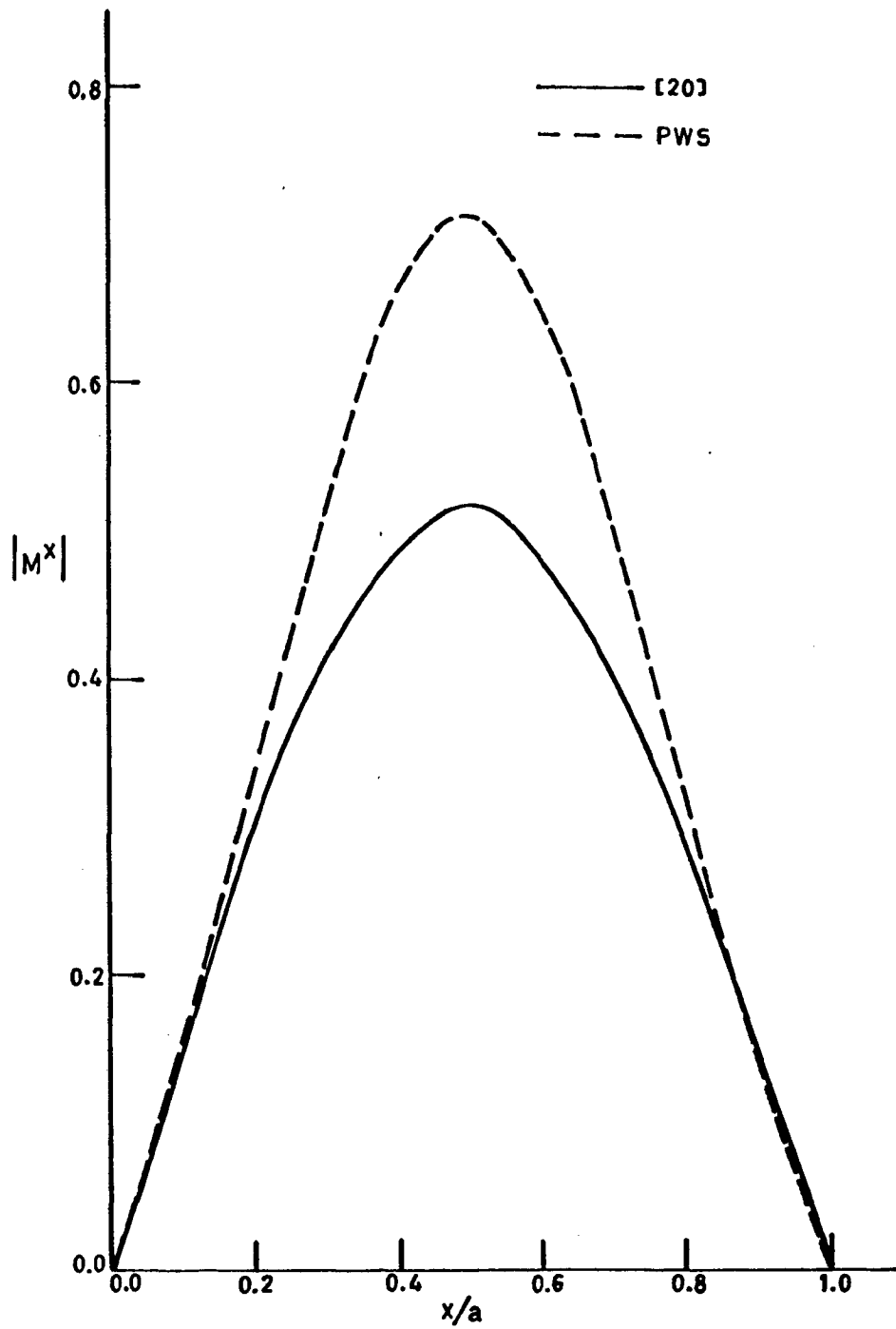(Case 4).

.Fig.3.23: Distribution of normalized current on
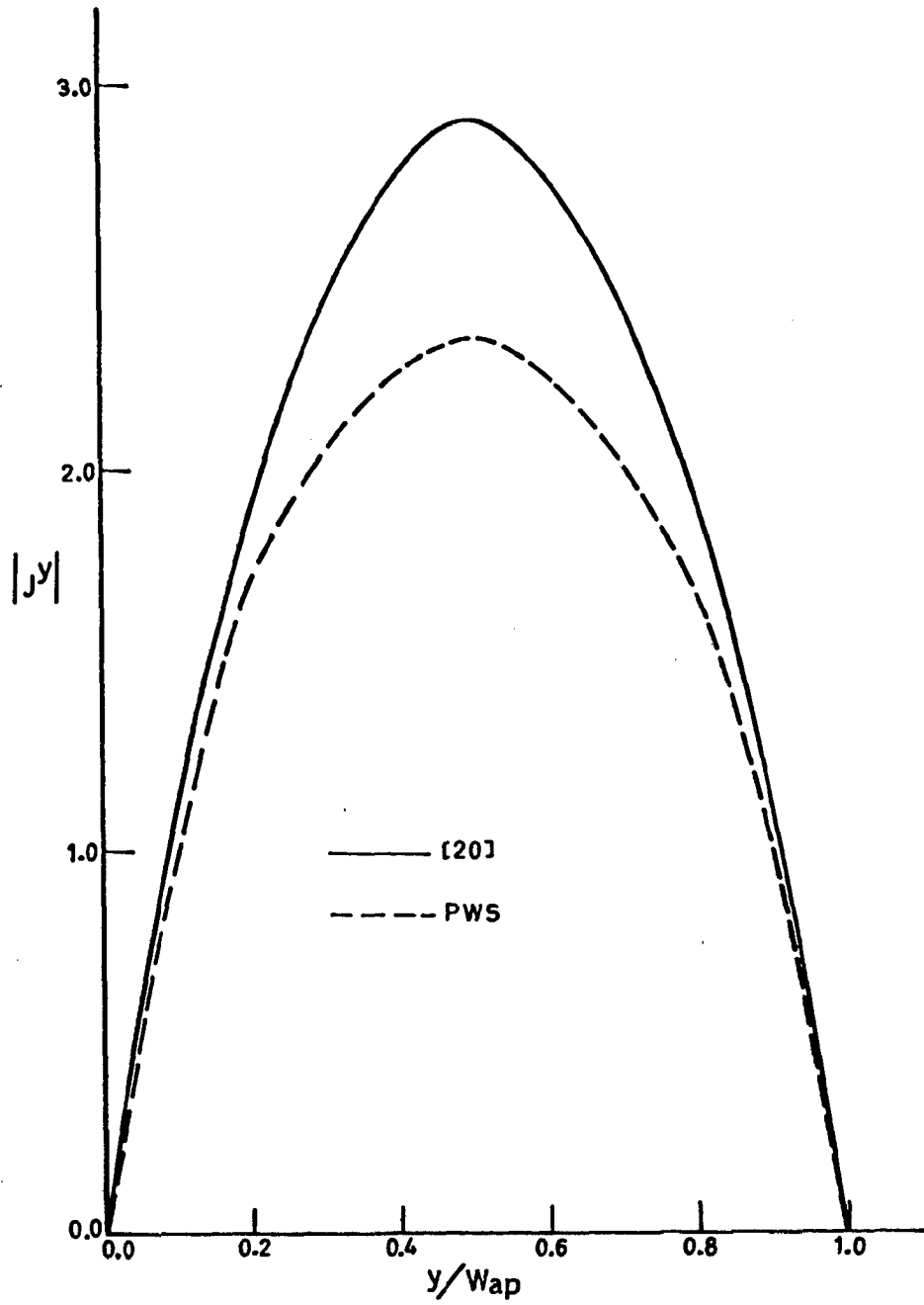the aperture (Case 4).

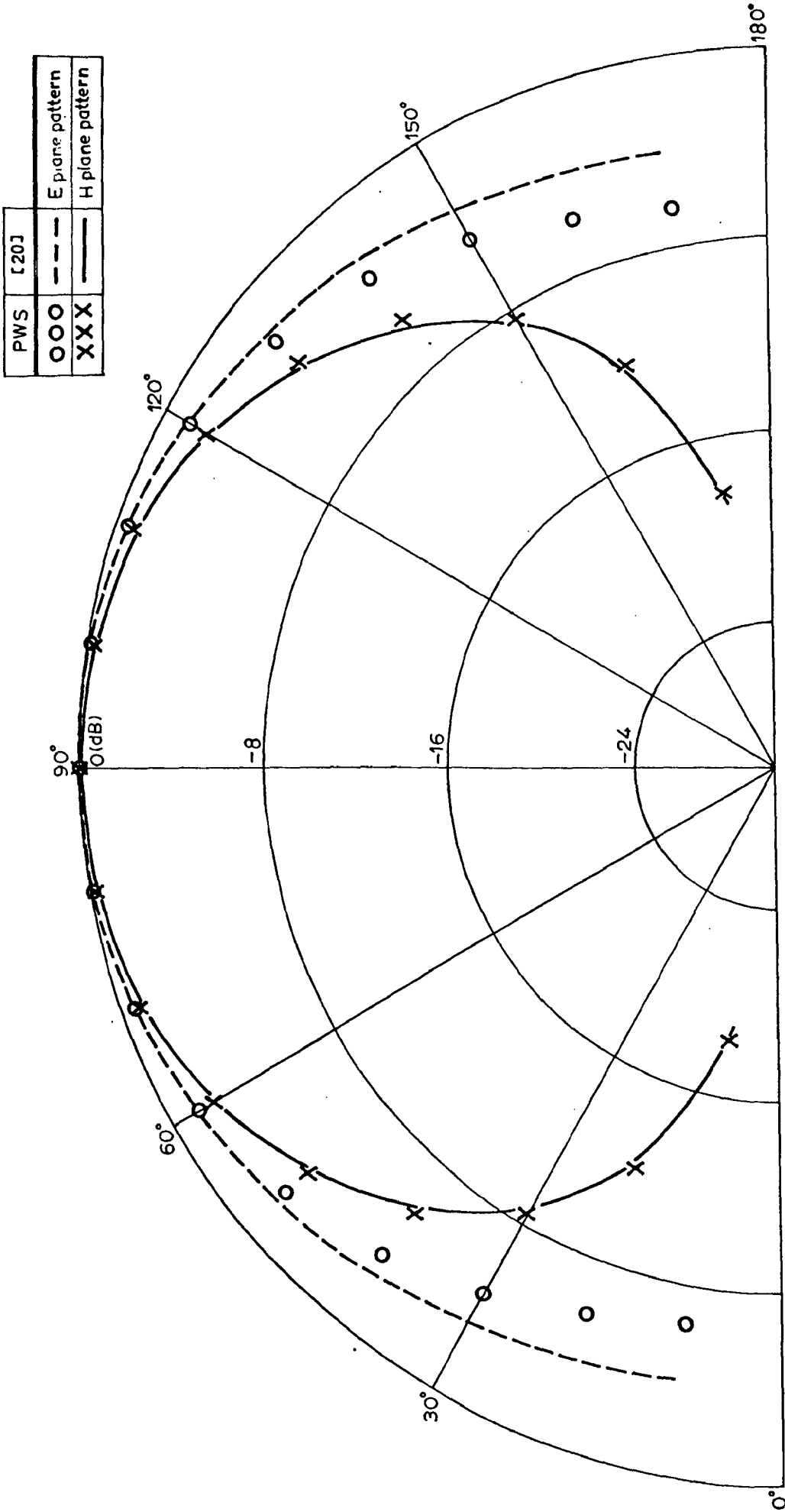Fig.3.24: Distribution of normalized current on
the patch (Case 4).

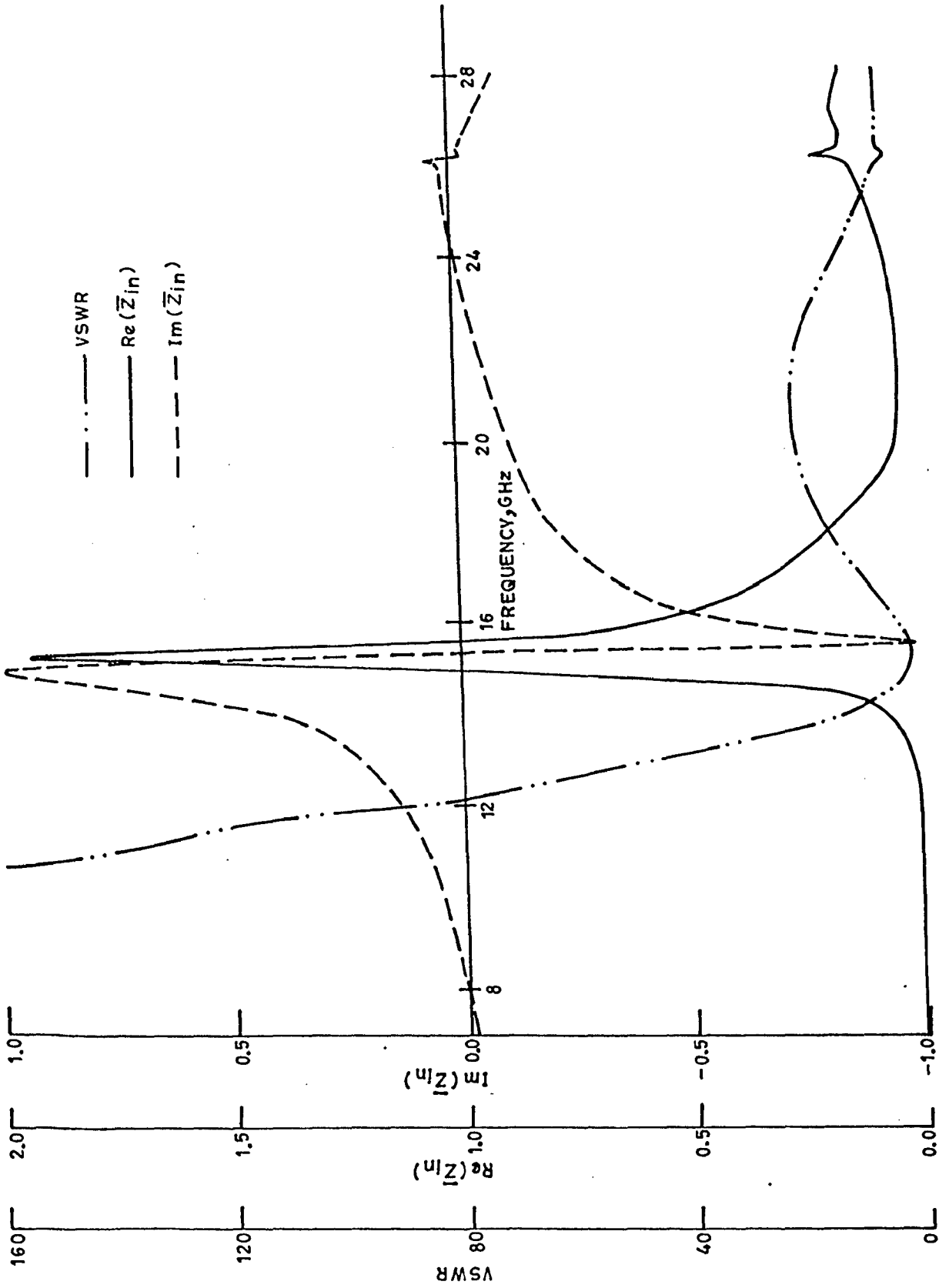Fig.3.25: Radiation patterns (Case 4).

83

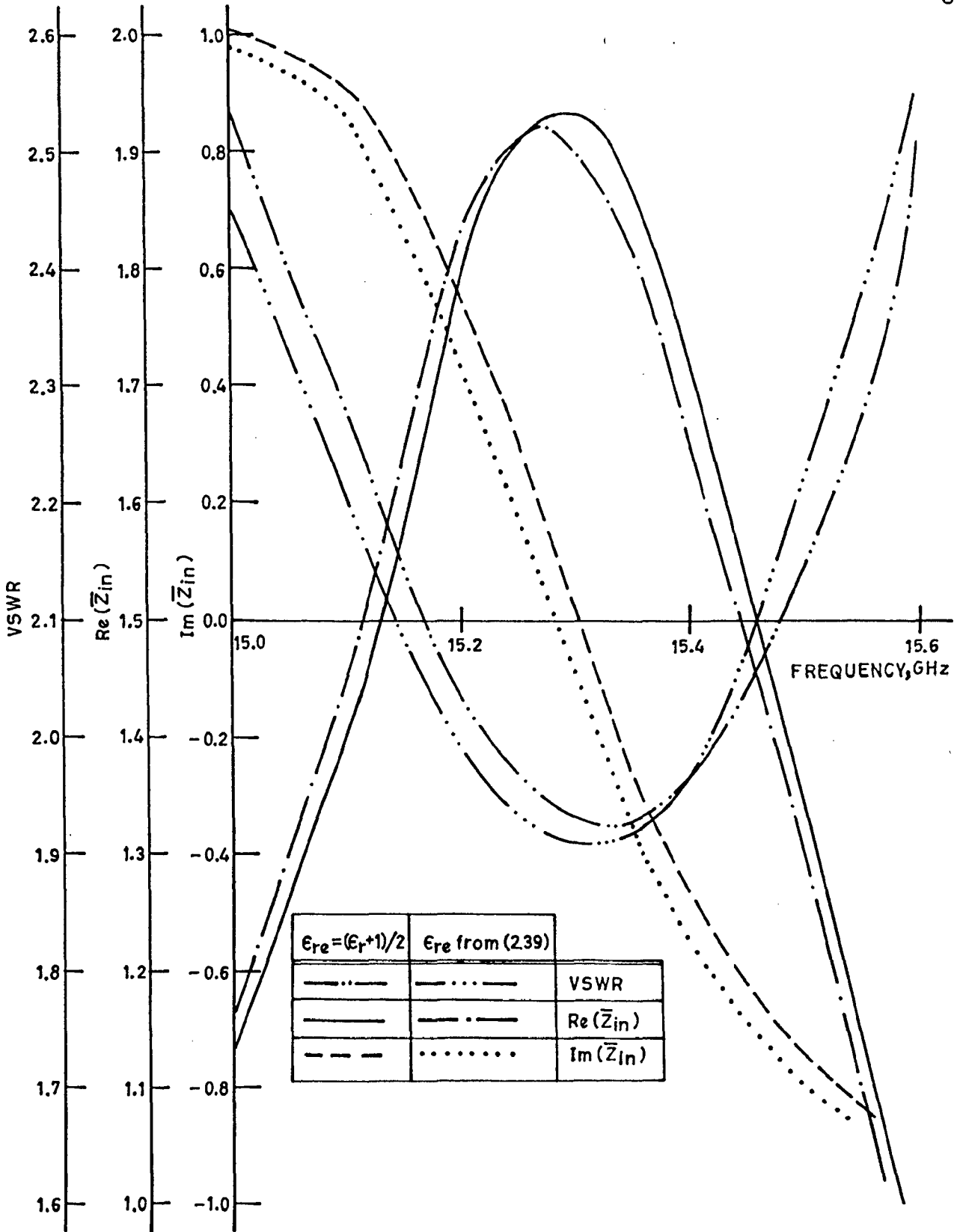Fig.3.26:Input characteristics of a waveguide fed patch antenna.

Fig.3.27: Input characteristics of a waveguide fed patch antenna around resonance.

CHAPTER 4

EXPERIMENTAL RESULTS

In this chapter, experimental results for a waveguide fed patch antenna are presented. Various antenna parameters, like the input voltage standing wave ratio (VSWR), input impedance, gain and radiation pattern of the antenna were measured in the laboratory. The effect of increasing the size of the ground plane was also studied. The fabrication technique used to construct the antenna is also explained alongwith the design procedure.

4.1 Design of the Radiating Element [24]

Polytetrafluoroethylene (PTFE) Glass Microfiber Reinforced RT Duroid 5880, having dimensions 6cm × 6cm, was used as the dielectric substrate. The parameters of the substrate relevant to the design procedure are,

Dielectric constant, e_r : 2.2 ± 0.02

Overall thickness   : 1.5mm

Cladding thickness, t   : 0.03556mm

Dielectric thickness, h   : 1.42888mm.

The aim was to design a patch having a TM_{01} mode resonant frequency of 10 GHz. Fig. 4.1 illustrates the experimental patch antenna, where L is the dimension of the radiating edge and W is the dimension of the non-radiating edge. The length of the radiating edge, L is given by

$$L = \frac{c}{2f_r} \left(\frac{\varepsilon_r+1}{2}\right)^{-\frac{1}{2}}$$ (4.1)

where

c : velocity of light in vacuum (m/s)

f_r : resonant frequency (Hz)

The line extension, ΔW, due to fringing effects is

$$\Delta W = h \times 0.412 \frac{(\varepsilon_e+0.3)(L/h+0.264)}{(\varepsilon_e-0.258)(L/h+0.8)}$$ (4.2)

where ε_e is the effective dielectric constant, given by

$$\varepsilon_e = \left(\frac{\varepsilon_r+1}{2}\right) + \left(\frac{\varepsilon_r-1}{2}\right)\left(1 + \frac{10h}{L}\right)^{-\frac{1}{2}} - \frac{\varepsilon_r-1}{4.6}\left(\frac{t/h}{L/h}\right)$$ (4.3)

The length of the non-radiating edge is now obtained from

$$W = \frac{c}{2f_r \varepsilon_e} - 2\Delta W$$ (4.4)

Using (4.1) through (4.4) the patch dimensions are determined. For the chosen data, these values are

L = 11.8585mm

W = 9.1895mm

The patch antenna is coupled to a standard X-band waveguide (a = 22.86mm, b = 10.16mm) via a rectangular aperture in its ground plane. The aperture, having dimensions AL = 11.43mm, AW = 1.5mm, is so located·that the centres of the patch and the aperture coincide with the axis of the waveguide.

4.2 Fabrication

The fabrication of a microstrip antenna is a very systematic exercise, involving a number of steps. These are explained below.

4.2.1 Artwork

The artwork is the drawing of the microstrip antenna. This is prepared either on a tracing sheet or on a tracing film. The tracing sheet deforms, by absorbing moisture, when exposed to humid atmosphere. Hence tracing film was used for this purpose. The tracing film has a ground and a shiny surface. The artwork is prepared on the ground surface.

Depending on the actual size, the scale for the artwork is chosen. For the present work a 4:1 scale was chosen. A rubylith film [25] was simulated using the tracing film by pasting opaque cellophane tapes on it. The patch was created on the film by cutting out the unwanted portions of the tape. This was found to give better edges than the 'printed circuit board' drafting aids. The actual dimensions were decided with the help of vernier calipers having a least count of 0.01mm. A travelling microscope would have improved the accuracy.

On another piece of film, the aperture area was marked using the same technique. A number of markings in the form of crosses (+) were made on both the films with the help of a drawing pen (Rotring, variant-B, art.1102). These markings were used to align the two masks while printing the image on the substrate.

4.2.2 <u>Mask Preparation</u>

The next stage is to reduce the artwork to the actual size and prepare the masks. The reduction and mask preparation follows the usual black and white photography technique. Since the patch area consisted of too many narrow strips, direct illumination and exposure of the artwork did not produce good quality masks. Hence, an indirect procedure was followed. A contact print was obtained by illuminating the artwork from bottom. This print had a uniform surface and, hence, could be reduced to the actual size without any difficulty.

4.2.3 <u>Screen Preparation and Printing on to the Substrate</u>

Once the masks are ready, the images on the masks have to be transferred on to the substrate. This was accomplished by screen printing technique. The basic concept of screen printing process is that of forcing a viscous material through predetermined openings in a stencil screen to obtain the desired image on the substrate. The screen was prepared by placing a positive of the mask on a screen printing film and exposing them to light. The exposed part of the film hardened and the unexposed portion dissolved in the developer. This was pasted on a porous screen made up of silk thread and allowed to dry. This is called the screen. Next, the screen was placed above the substrate, which was first cleaned to remove dirt and grease, and a special dye was squeezed over the screen. The dye passing through the openings in the film deposited on the substrate and was allowed to dry.

The screen for the other side was also prepared using the same technique. The other side of the substrate was also printed after aligning the two images, which was carried out with the help of markings on the second screen and the holes drilled through the substrate. When the dye was completely dry, visual inspection was carried out to locate any pin holes, which were covered up with the dye.

4.2.4 Etching

The next step is to remove or etch out the unwanted portion of copper from the substrate which is not covered by the dye. Ferric chloride was used as the etchent. The substrate was introduced into the ferric chloride solution which was occasionally stirred to increase the speed of etching. The completion of etching was detected by visual inspection. After the completion of etching, the dye on the substrate was removed with the help of a solvent to expose the patch and the ground plane.

4.2.5 Power Launcher

A rectangular waveguide was soldered to the ground plane of the antenna in such a way that the axis of the guide aligned with the centre of the aperture. The alignment was done with the help of markings on the waveguide and the ground plane. To obtain a good contact between the two, the waveguide walls were made very sharp at the end by filing (Fig. 4.1). Visual inspection of the inside of the waveguide revealed that there

were no holes in the joint and no solder had leaked into the guide, ensuring a good joint.

4.3 Experimental Setup

In this section the experimental setup used to measure the different parameters has been illustrated.   Since the standard techniques were followed [26] to perform the measurements, only the precautions are listed in this section.

4.3.1 VSWR and Impedance Measurement

Fig. 4.2 illustrates the experimental setup used to measure the VSWR and the input impedance. Since any disturbance in front of the antenna changes the input characteristics, microwave absorbers were placed in front of the antenna.

4.3.2 Radiation Pattern Measurement

The setup shown in Fig. 4.3 was used to measure the radiation pattern.   The test antenna, placed on a turntable with graduations, was utilised as the transmitting antenna. Both the antennas were polarization matched and aligned.   The distance between the two antennas was kept greater than $2D^2/\lambda$; where D is the longer antenna dimension and λ is the operating wavelength.   When the turntable is rotated to measure the radiation pattern, the transmitting antenna should not change its orientation.   This was ensured by securely padding the fixture used to hold the antenna. The frequency meter in this setup was placed on the receiver side as there was no space on the turntable.

4.4 Results and Discussion

Experiments were carried out to study the behaviour of the patch with a small ground plane and with an extended ground plane (EGP). Various parameters like the input VSWR, input impedance, gain and radiation patterns were measured.

Fig. 4.4 illustrates the input characteristics of a waveguide fed patch antenna with a 6cm × 6cm ground plane. Three different parameters, namely, the VSWR, real part of input impedance (resistance) and imaginary part of input impedance (reactance) are plotted in the same graph as a function of frequency. The input impedance plot indicates the presence of alternate parallel and series resonant frequencies. The series resonance is characterised by a low value of resistance and the reactance changing from capacitive to inductive. On the other hand, a peak value of resistance alongwith the reactance changing from inductive to capacitive denotes a parallel resonant frequency. The parallel resonance points are arising due to the excitation of different modes. The resonant frequency of a tuned circuit is defined as the frequency at which the input impedance has no reactive part ($f_{X=0}$). In microstrip antennas, however, this frequency may not coincide with the frequency at which the real part of the input impedance reaches a peak ($f_{R=max}$) because of reactive loading due to the feed. To avoid any ambiguity, we have chosen the resonant frequency as the one at which the real part of the input impedance reaches a peak [27]. The variation of input

impedance with frequency is also plotted on Smith charts (Fig. 4.5). It is seen that the loci of the input impedance are circular in nature and symmetric about the X = 0 line. However, there is a large impedance mismatch at all the frequencies, resulting in a high reflection loss.

Both the E- and the H-plane radiation patterns were measured at various series and parallel resonant frequencies and are shown in Figs. 4.6-4.12. Using a standard gain horn (Scientific Atlanta Model 12-8.2) as a reference, the gain of the patch antenna was measured at each of these frequencies in the broad-side direction. For the purpose of comparison, the various antenna parameters are tabulated in Table 4.1.

A study of the radiation patterns reveals that both the E- and the H-plane patterns are quite broad and exhibit amplitude fluctuations. These fluctuations can be attributed to the finite size of the ground plane, which causes the diffraction of the surface waves. As the operating frequency is increased, the electrical thickness of the substrate increases. This results in increased surface wave powers and, therefore, the undulations in the pattern increase in amplitude. Also, it is observed that, in general, the undulations are more pronounced at series resonant frequencies, although at 10.6 GHz, a parallel resonant frequency, the undulations are found to be quite high.

In the case of a co-axial feed patch antenna, the patch dimensions determine the resonant frequency of a mode, but the

TABLE 4.1 CHARACTERISTICS OF A RECTANGULAR PATCH ANTENNA COUPLED TO A WAVEGUIDE VIA AN APERTURE IN ITS GROUND PLANE

Frequency GHz	Resonance	VSWR	Re($\overline{Z}_{in}$)	Im($\overline{Z}_{in}$)	Gain dB	Reflection loss dB	Gain after mismatch correction dB	10 dB beamwidth degrees		After tuning out the VSWR with a slide screw tuner		Extended ground plane Gain dB	10 dB beamwidth degrees	
								E	H	VSWR	Gain dB		E	H
8.6	parallel	17.3	0.315	-2.1	1.37	6.84	8.21	155	138	2.2	6.27	0.87	173	140
9.2	parallel	37.03	0.56	-4.45	-1.88	7.79	5.91	159	133	1.12	3.52	-3.98	175	134
9.5	series	11.6	0.085	+0.1	-3.757	5.34	1.583	140	112	3.6	2.24	-5.66	164	122
9.86	parallel	36.0	0.47	-2.0	-6.95	9.78	2.83	155	133	2.0	1.8	-8.2	165	129
10.3	series	9.27	0.125	+0.4	-7.4	4.54	-2.86	25	40	1.95	-4.6	-8.1	68	44
10.6	parallel	14.35	1.1	+0.35	-8.04	6.133	-1.9	132	112	1.75	-6.34	-8.74	128	118
11.0	series	27.05	0.035	0.0	-6.4	8.62	2.22	60	74	2.7	-1.9	-9.2	91	97

Note: reflection loss $= 20 \log \left| \dfrac{1}{\sqrt{1-\Gamma^2}} \right|$ and $\Gamma = \dfrac{VSWR-1}{VSWR+1}$

Gain after
mismatch correction = gain + reflection loss

94

feed location determines as to which mode will be excited. Thus, the overall radiation pattern depends upon the feed-patch interaction. In the present case, the feed-patch interaction is much more complex since the self susceptance of the aperture is also a strong function of frequency. It is conjectured that here a number of modes are being simultaneously excited, albeit with varying amplitudes, affecting the input impedance and the radiation pattern. The most smooth pattern was obtained at 8.6 GHz, where the measured gain was also positive (Table 4.1). Since the input impedance was initially measured with 200 MHz increments in frequency, this frequency was estimated as a parallel resonant frequency. However, measurements with smaller frequency increments (50 MHz) revealed that the resonance actually occurs at 8.5 GHz. It is, therefore, believed that the fundamental TM_{01} mode is being excited at this frequency. The low value of gain at broad-side can be attributed to a high reflection loss. When the reflection loss is taken into account, the gain is of the order of 8 dB, with respect to an isotropic antenna, at 8.6 GHz. However, at 10.3 GHz and above, the gain comes out to be negative even after taking the reflection loss into account. This is because a large portion of the input power is being lost in the side lobes.

In order to reduce the reflection loss, a slide screw tuner was utilised to match the antenna. The corresponding VSWR and uncorrected gain are given in Table 4.1. The measured patterns at 8.6 GHz and 9.2 GHz (Figs. 4.13 and 4.14) indicate that the antenna has become more directive, thus, increasing

the gain substantially. However, a number of distinct and high side lobes appear in the visible region. It seems that the inclusion of the tuner affects the loading of the patch and drastically changes the current distribution.

The effect of increasing the size of the ground plane was also studied by soldering a 18cm × 18cm × 1.59mm brass sheet to the ground plane of the antenna. The radiation patterns at various series and parallel resonant frequencies (Figs. 4.15-4.21) show that the patterns have become comparatively smooth. This is due to the reduction in the secondary radiations caused by the diffraction of surface waves at the edge of the substrate. Asymmetry in the H-plane pattern at 8.6 GHz may be due to reflections from the ground. It can, therefore, be concluded that improved results shall be obtained by using a larger substrate.

The use of a slide screw tuner to match the antenna with EGP again resulted in high side lobe levels (Fig. 4.22).

Since both the E- and H-plane patterns have wide beam widths, reflection from ground and the walls have a considerable effect on the radiation pattern. The use of microwave absorbers would improve the results. Though the slide screw tuner provides a good match at the input, its use is not recommended as it changes the patch current distribution and hence the radiation pattern. An impedance transformer may perhaps be used to obtain a better match, but its effect on the patch current distribution is yet to be studied. Although maximum

care was taken while performing the experiments, accurate, reliable and repeatable results can only be obtained by using a network analyzer.

4.5 Summary

In this chapter, design and fabrication of a microstrip patch antenna coupled to a rectangular waveguide via an aperture in its ground plane have been explained. Various antenna parameters, like the input VSWR, input impedance, gain and radiation pattern have been presented. With the help of these results the TM_{01} mode resonant frequency has been determined. The effect of increasing the size of the ground plane and use of a slide screw tuner to obtain a match on the parameter has also been studied.
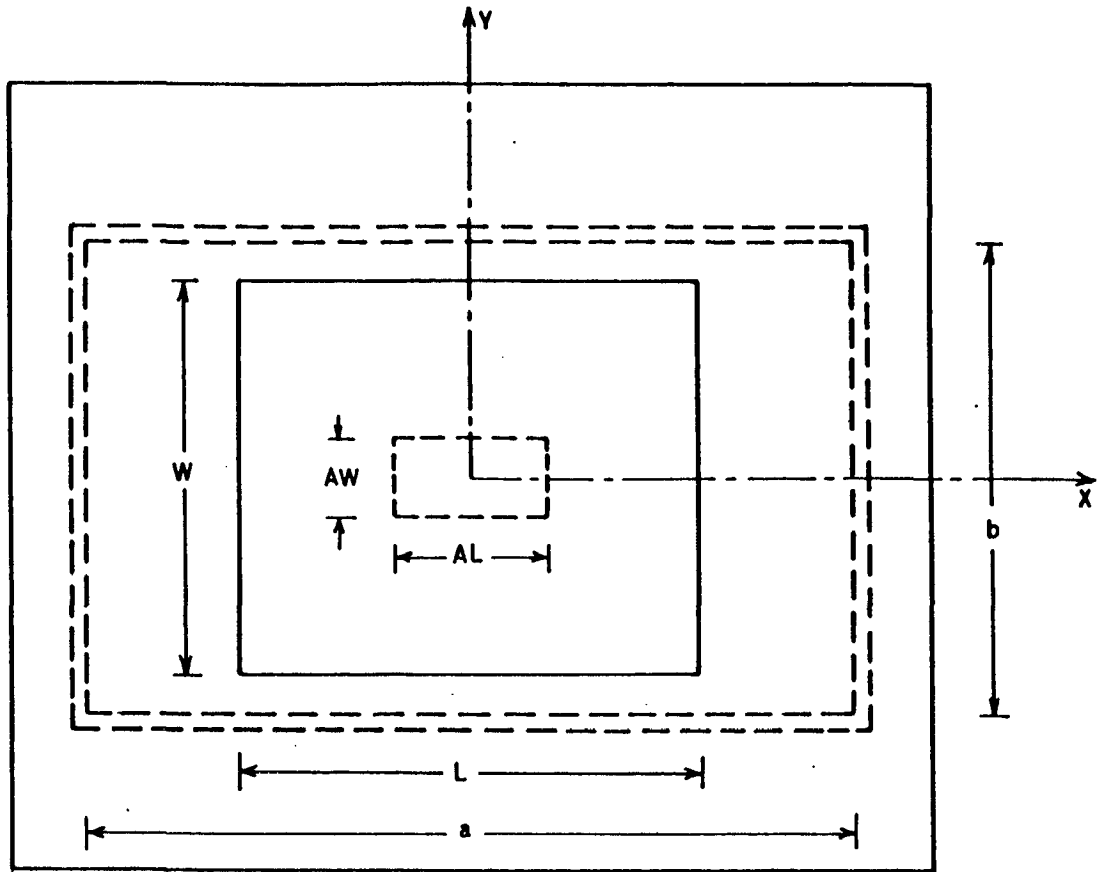
(a) TOP VIEW
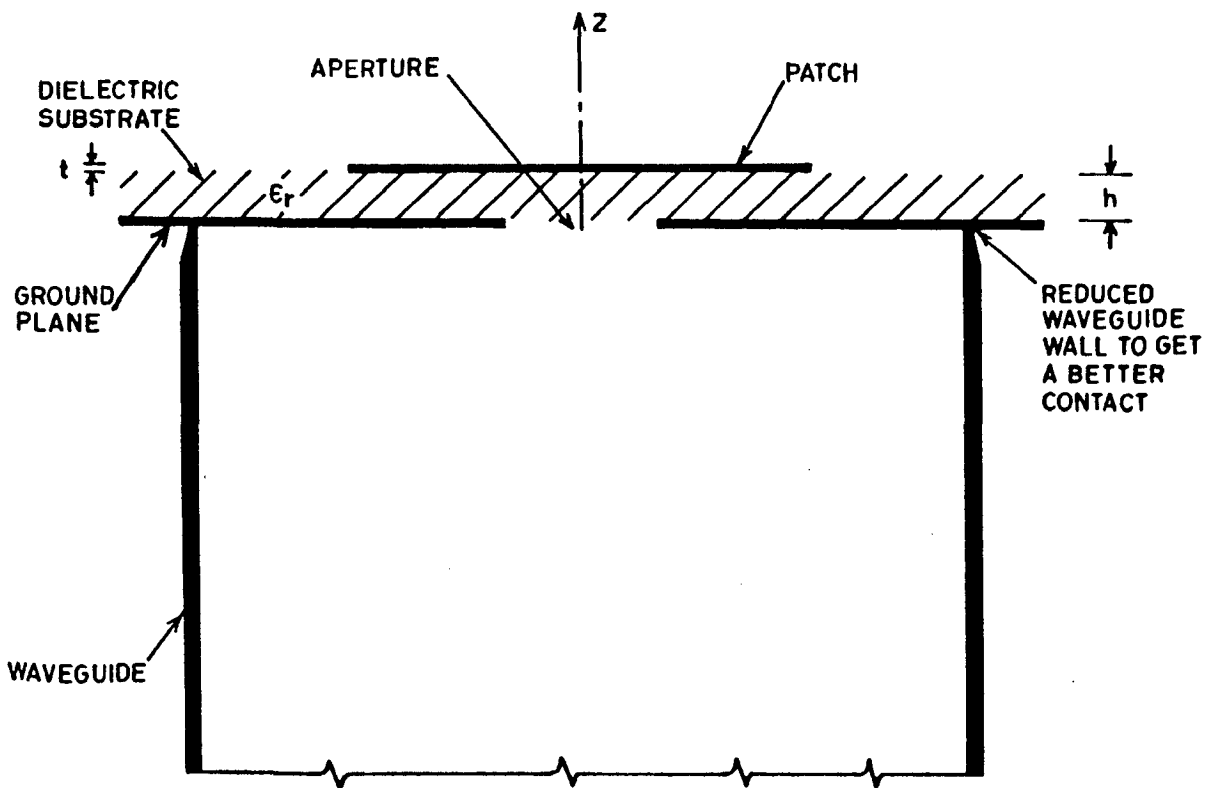
(b) SIDE VIEW

Fig.4.1: Microstrip patch antenna coupled to a rectangular waveguide via an aperture in the ground plane.
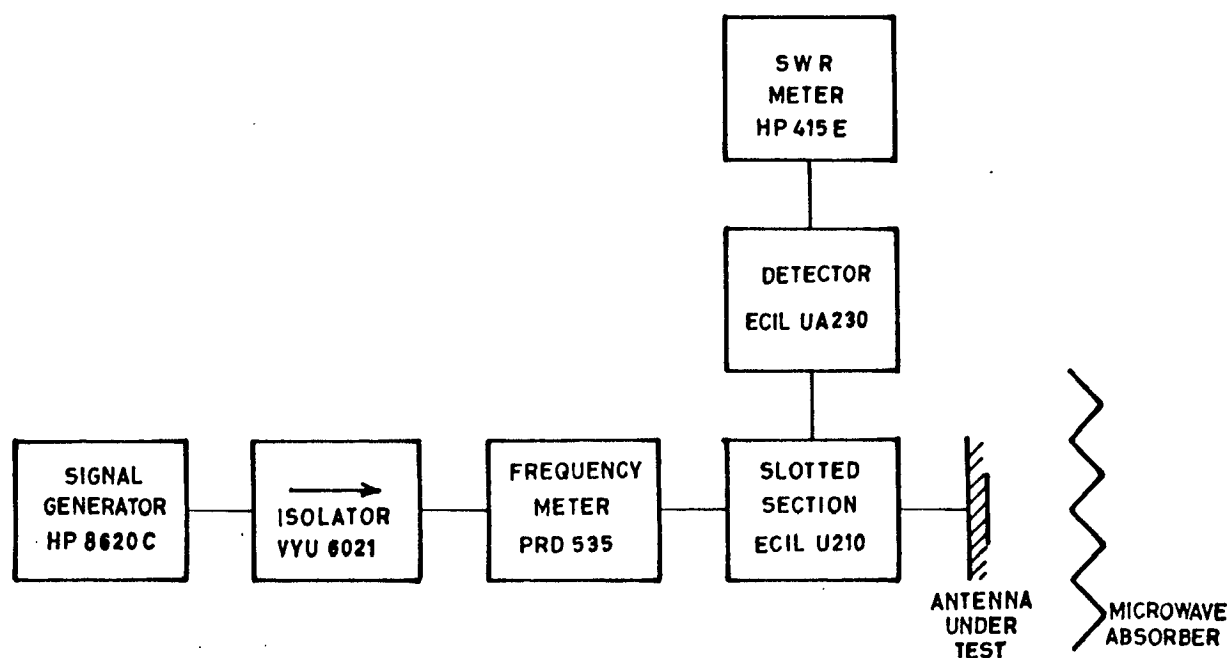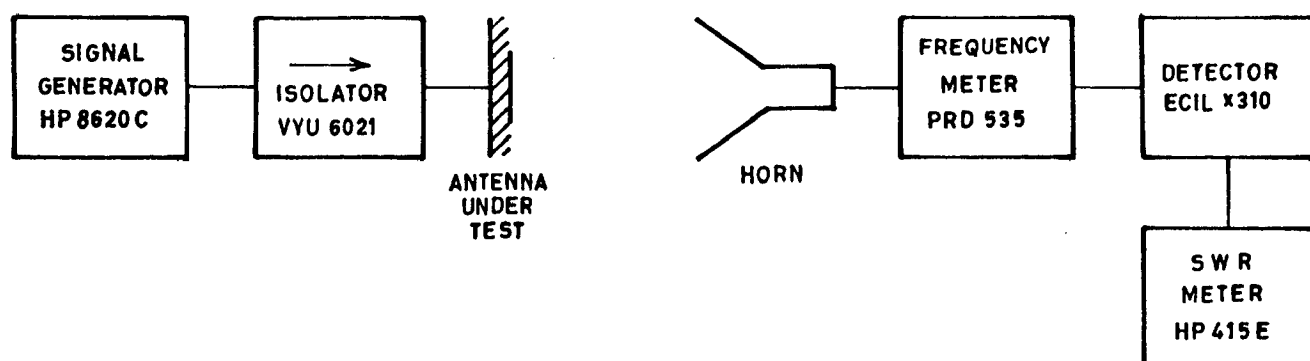
Fig.4.2: Measurement of VSWR and impedance.

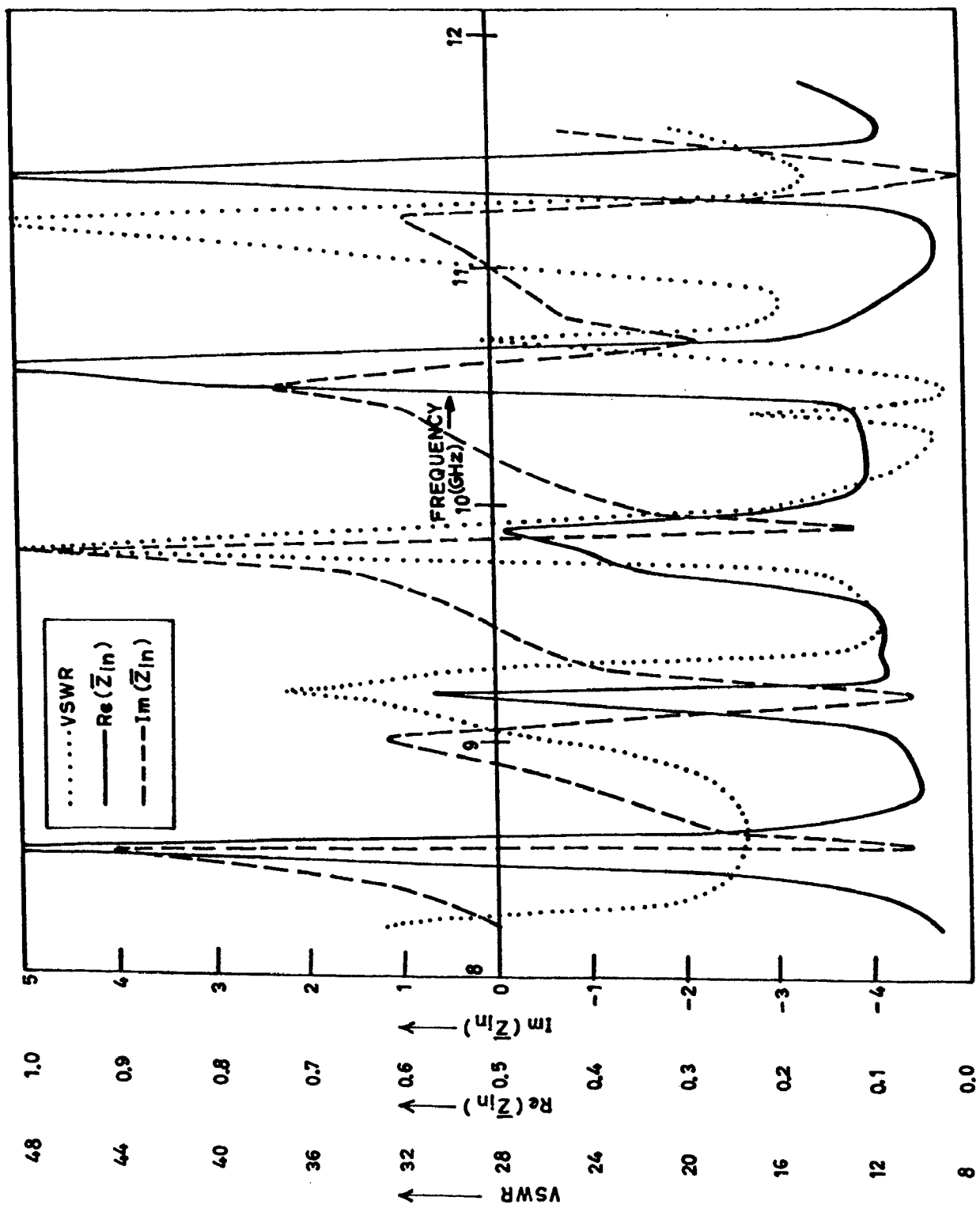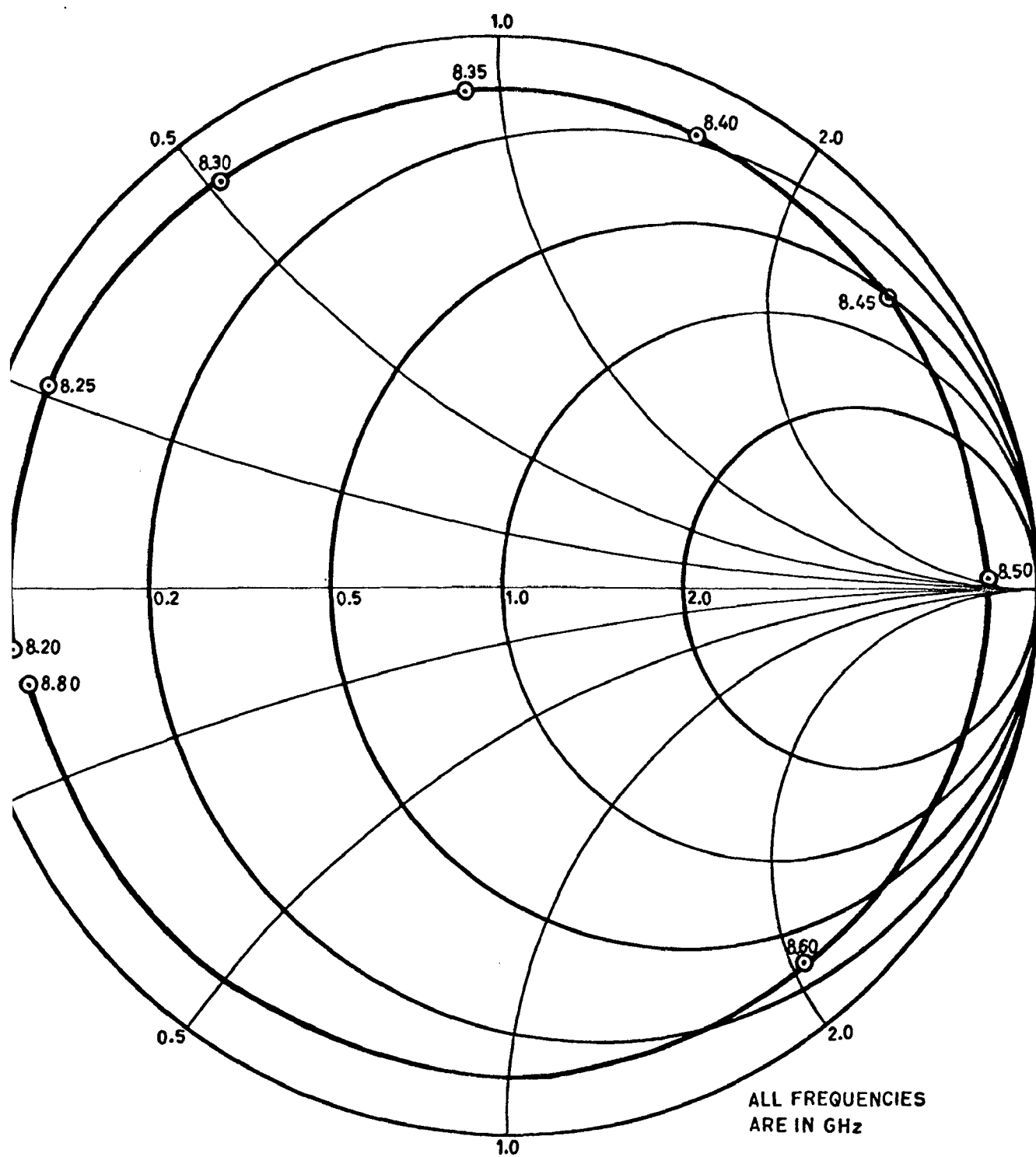Fig.4.3: Measurement of radiation pattern.

Fig.4.4: Input characteristics of a rectangular patch antenna coupled to a waveguide via an aperture in its ground plane as a function of frequency.

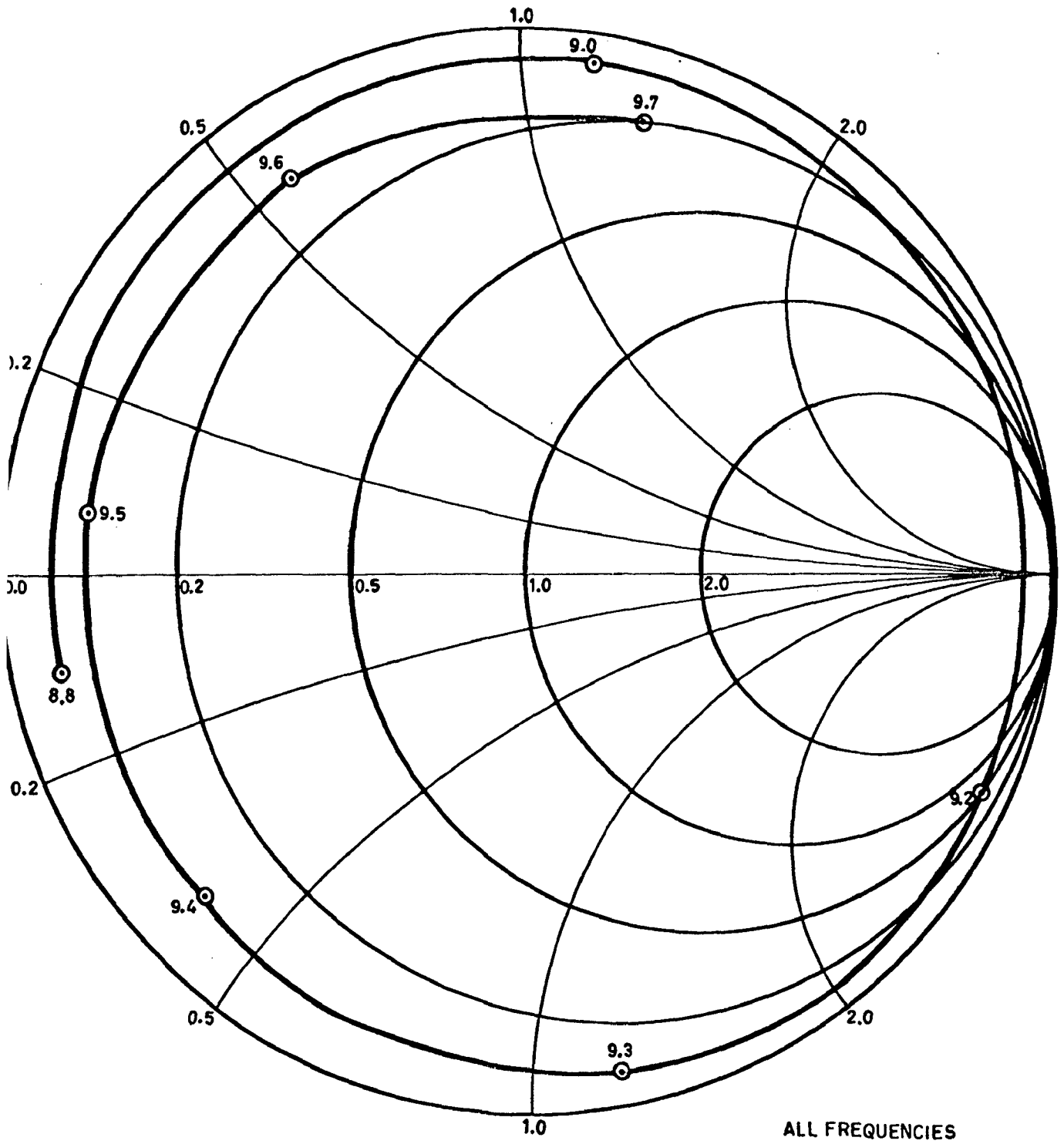1.5: Input impedance as a function of frequency for a patch antenna.
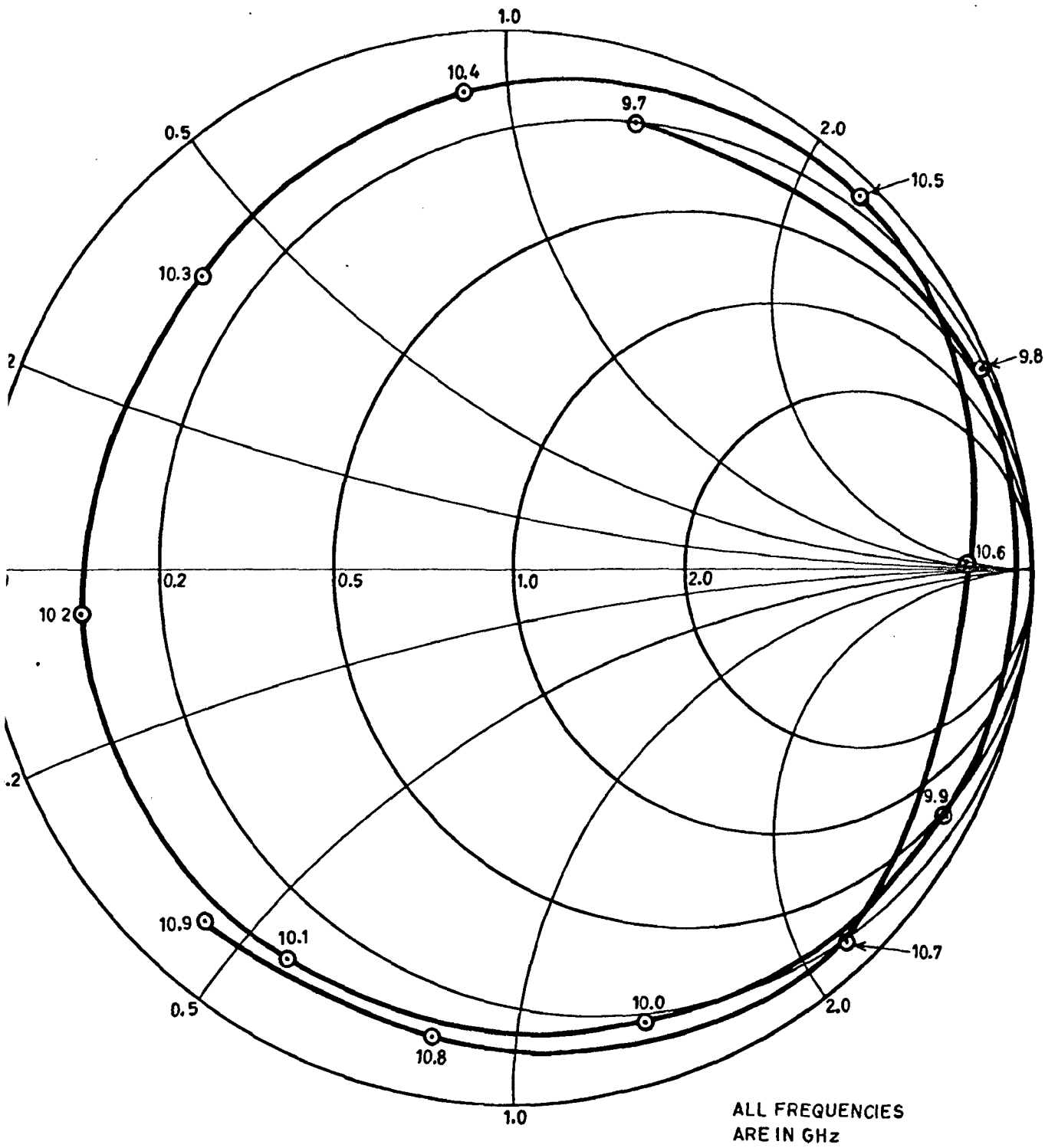
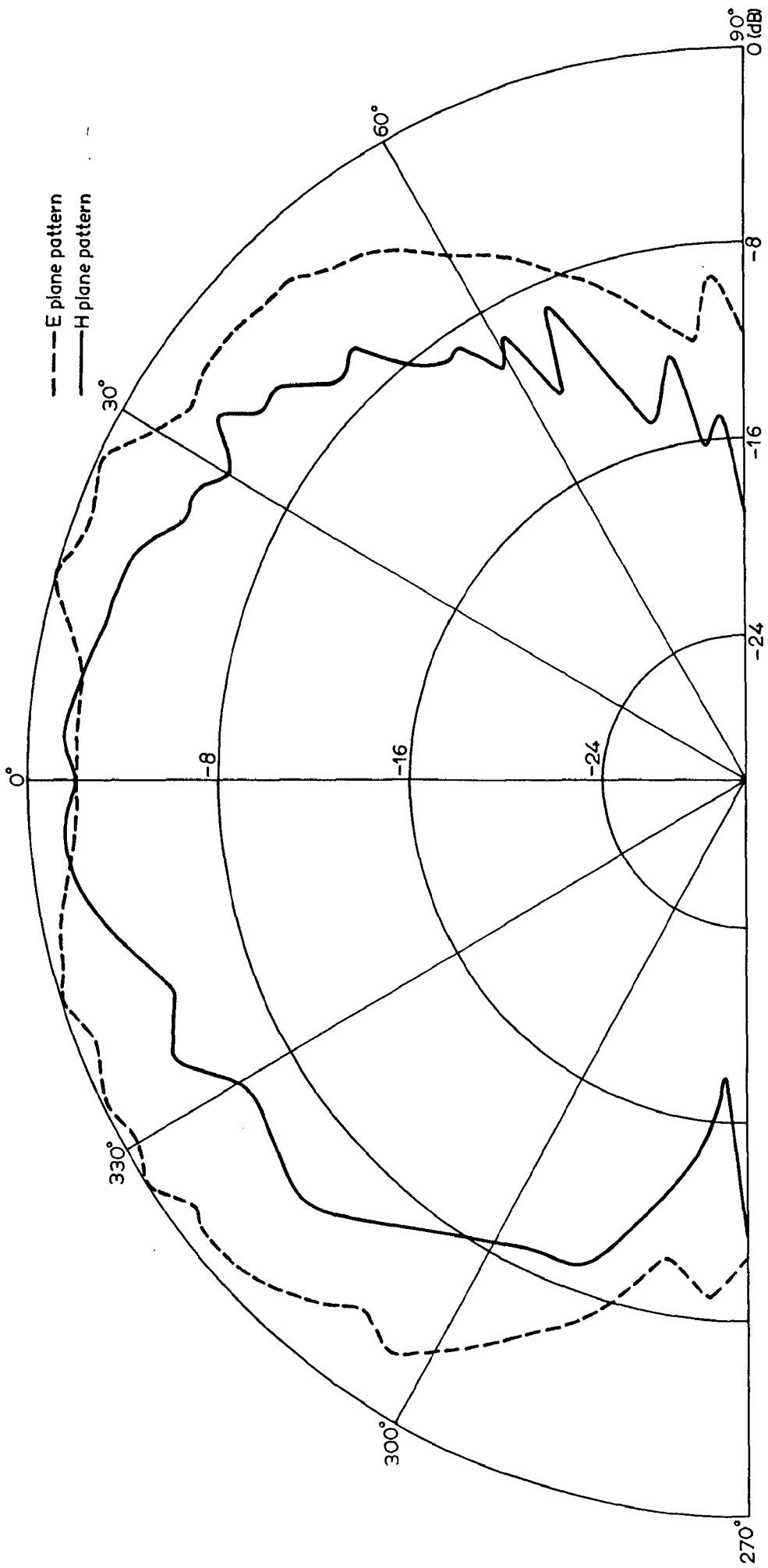Fig.4.5 (Continued)

Fig.4.5 (Continued)

Fig.4.6:Radiation patterns of a patch antenna at 8.6 GHz.
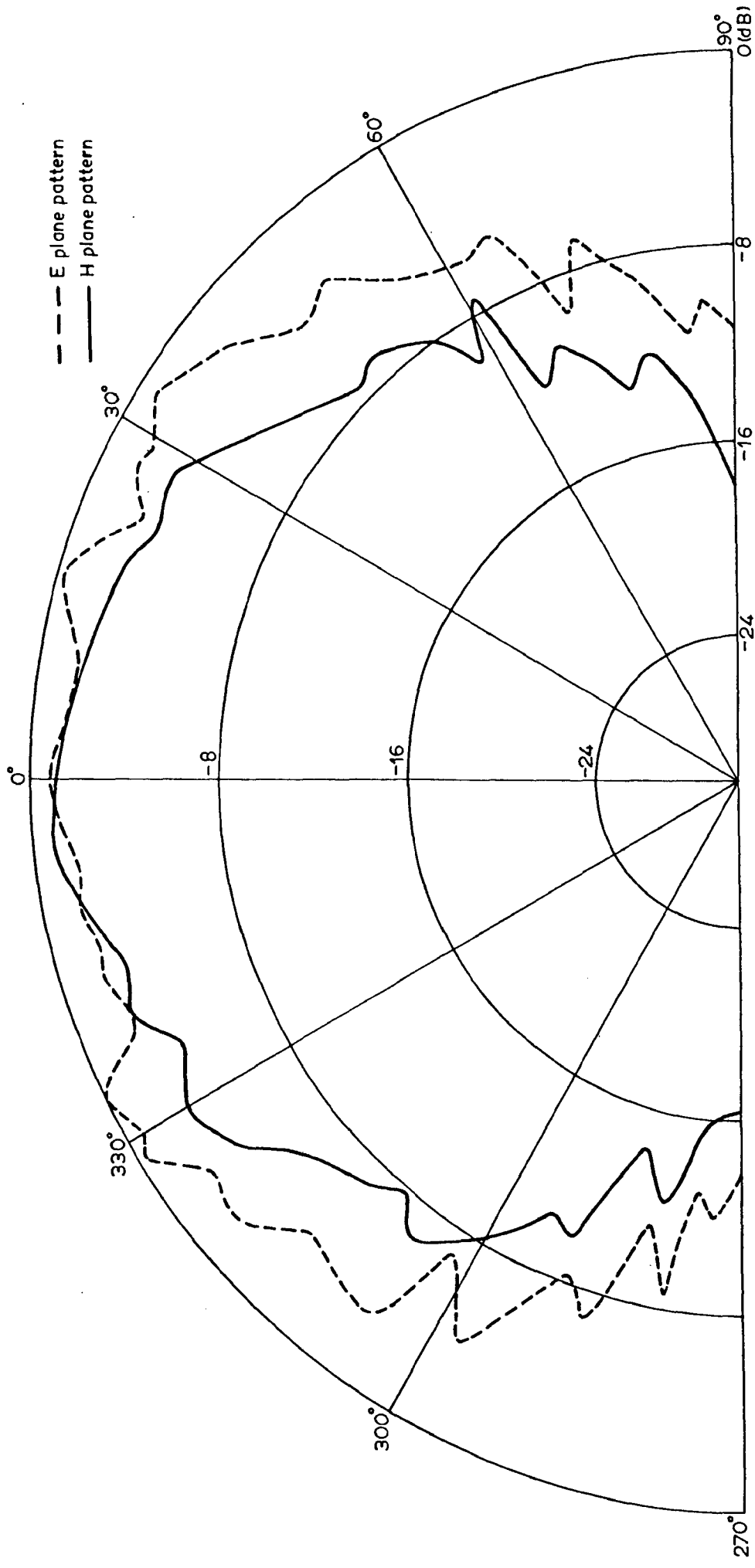
E plane pattern
H plane pattern

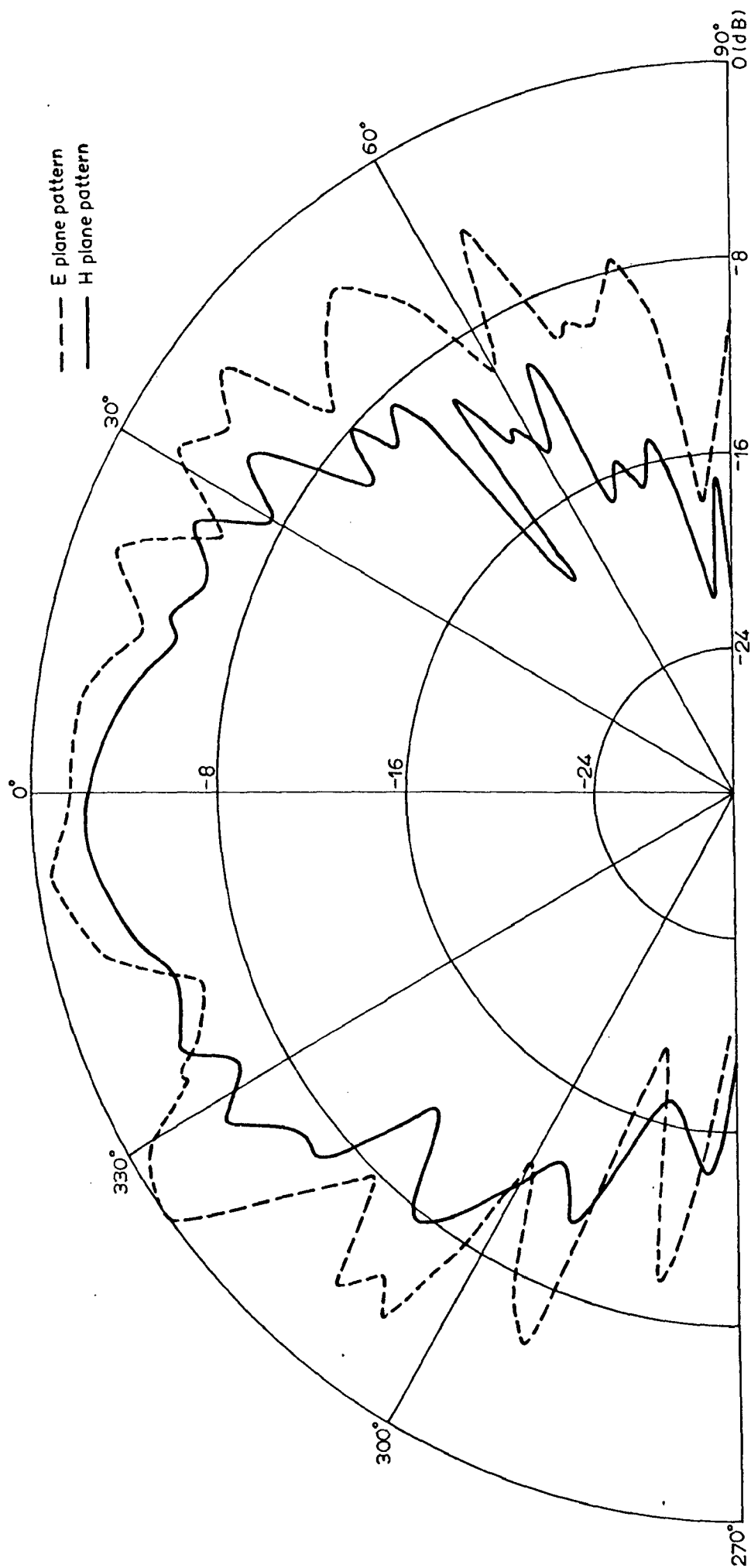Fig.4.7: Radiation patterns of a patch antenna at 9.2 GHz.

Fig.4.8 : Radiation patterns of a patch antenna at 9.5 GHz.
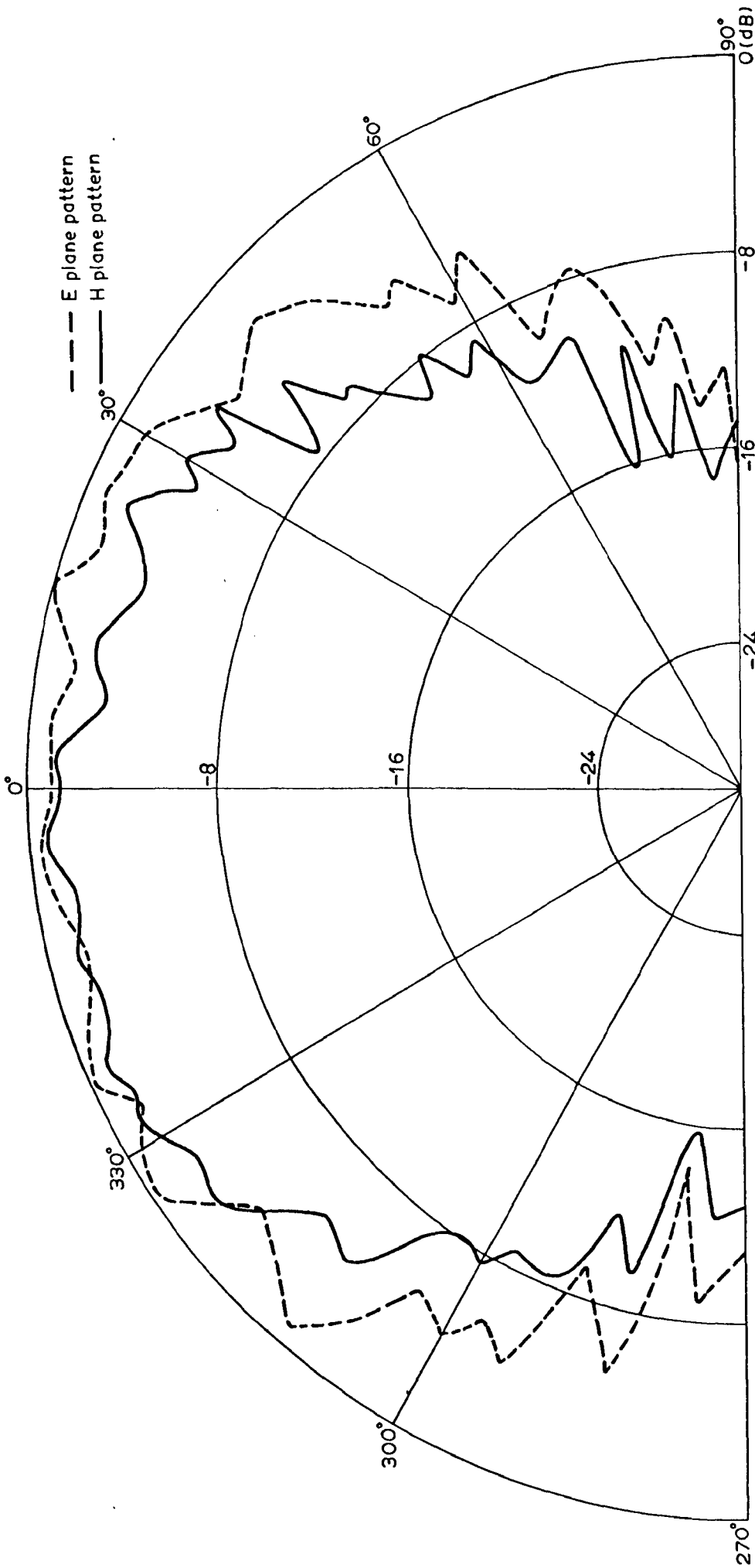
Fig.4.9 : Radiation patterns of a patch antenna at 9.86 GHz.

Fig.4.10: Radiation patterns of a patch antenna at 10.3 GHz.

Fig.4.11: Radiation patterns of a patch antenna at 10.6GHz.

Fig.4.12: Radiation patterns of a patch antenna at 11 GHz.
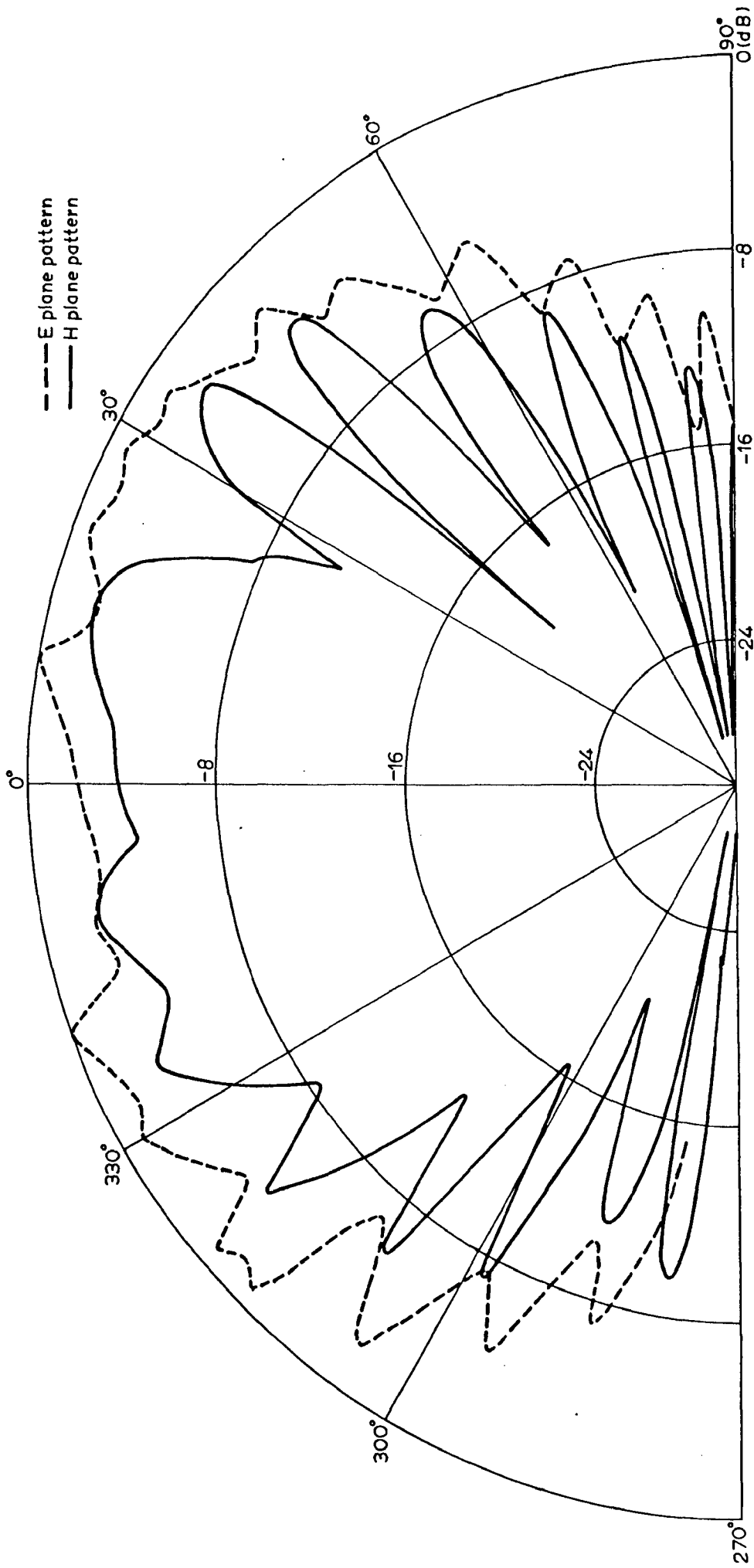
Fig.4.13 : Radiation patterns of a tuned patch antenna at 8.6GHz.
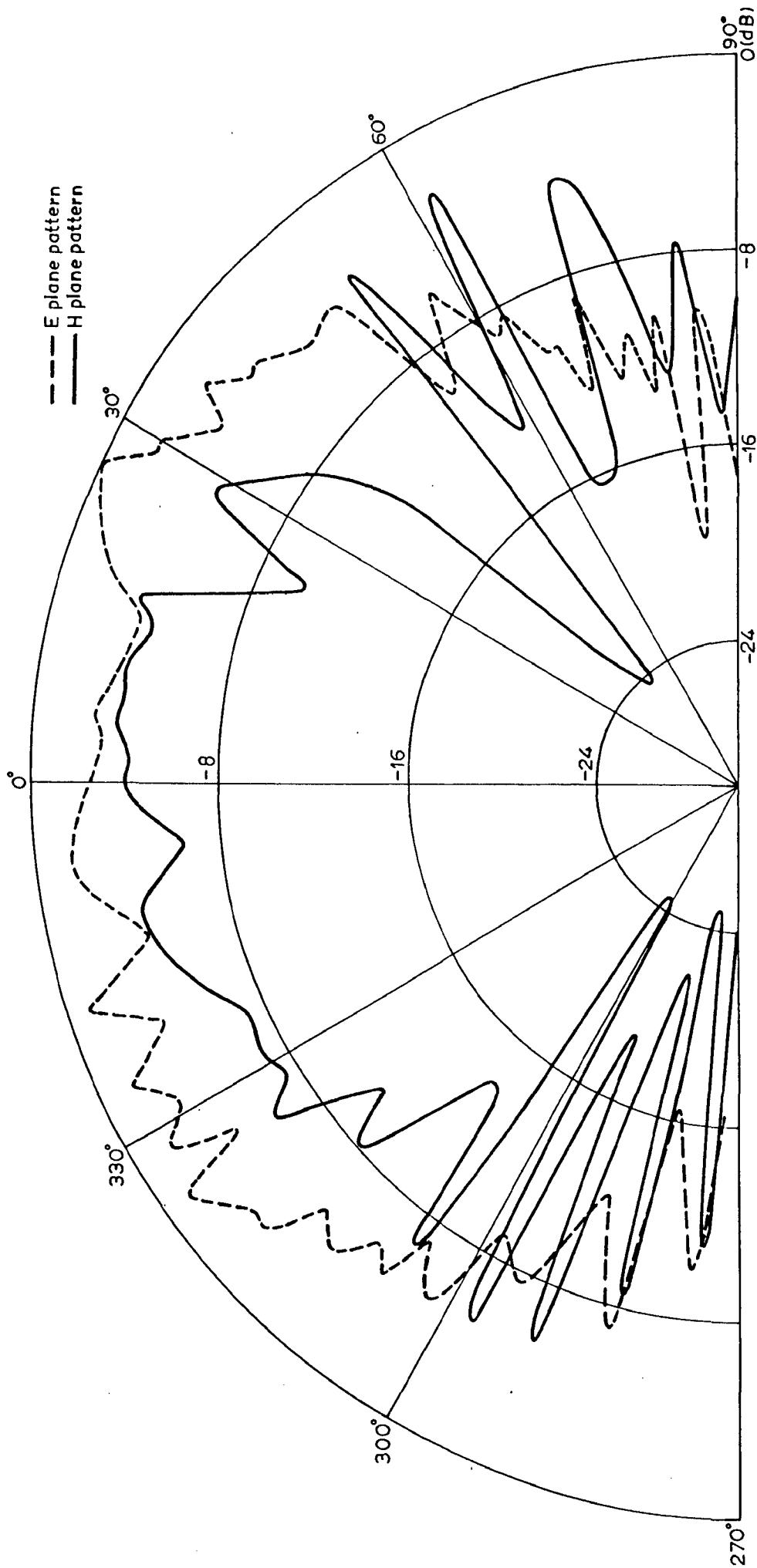
Fig.4.14: Radiation patterns of a tuned patch antenna at 9.2 GHz.

Fig.4.15:Radiation patterns of a patch antenna at 8.6GHz (EGP).

E plane pattern
H plane pattern
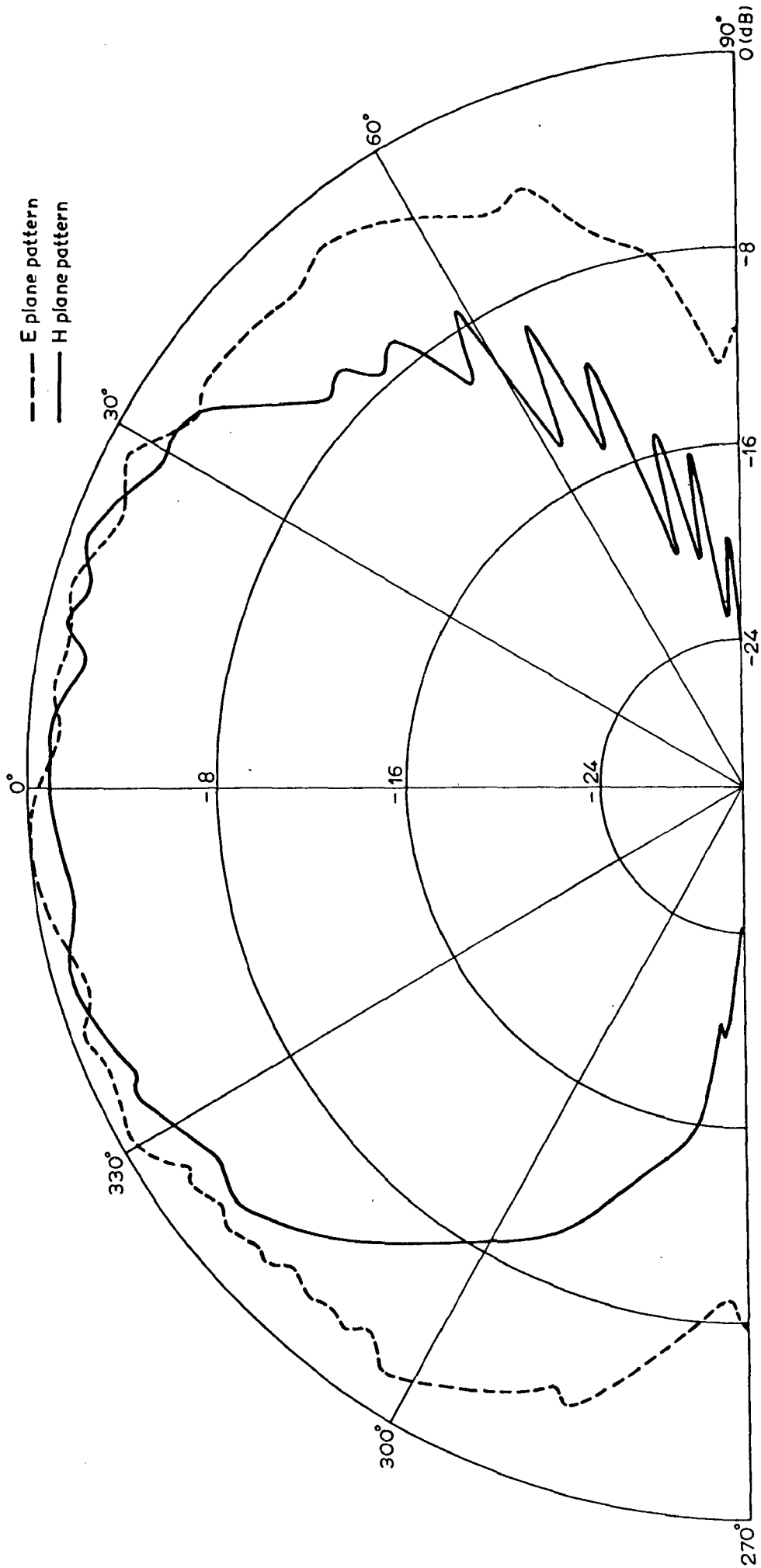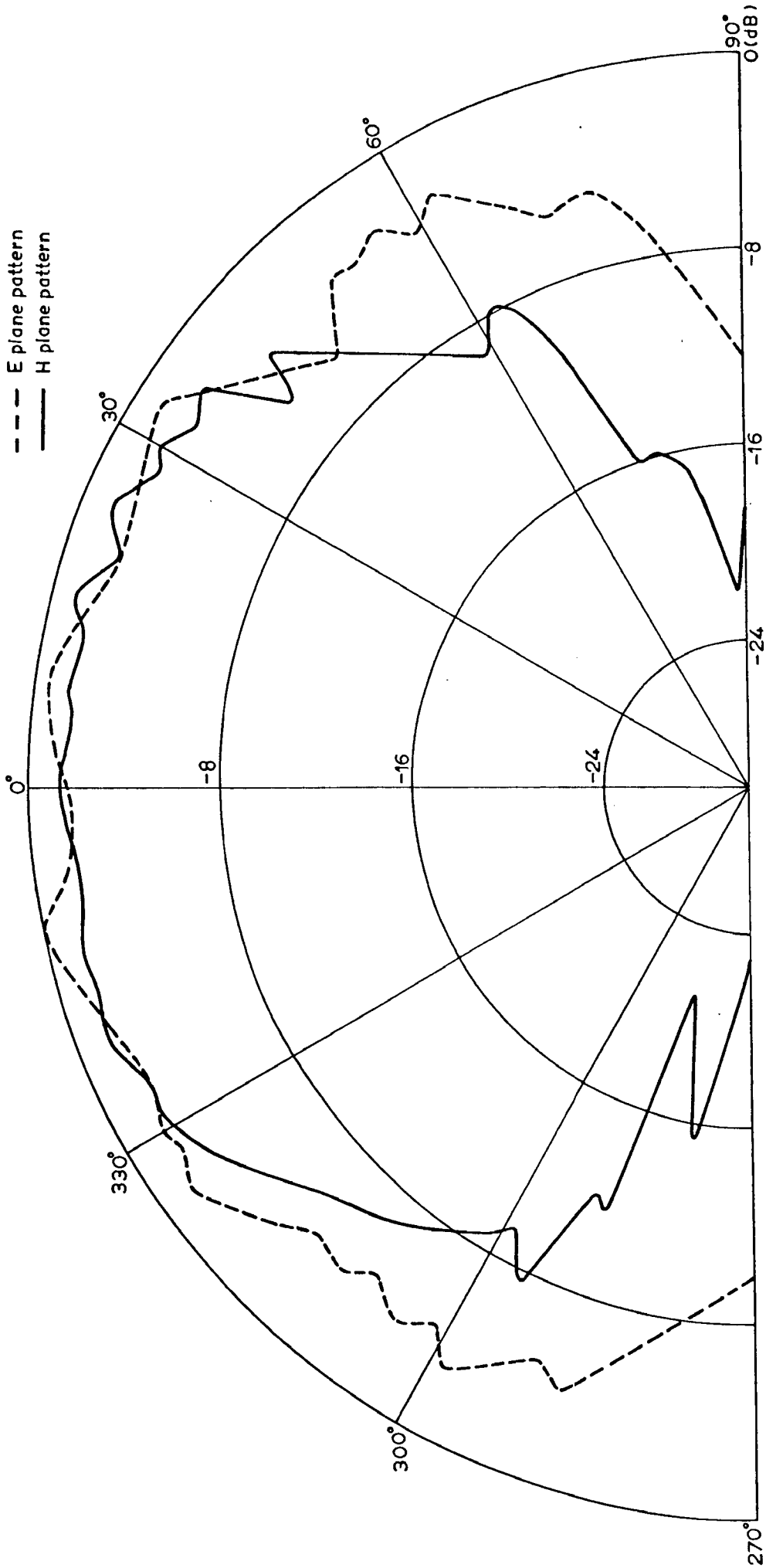
Fig.4.16: Radiation patterns of a patch antenna at 9.2 GHz (EGP).

Fig.4.17:Radiation patterns of a patch antenna at 9.5GHz (EGP).

Fig.4.18: Radiation patterns of a patch antenna at 9.86GHz (EGP).

E plane pattern
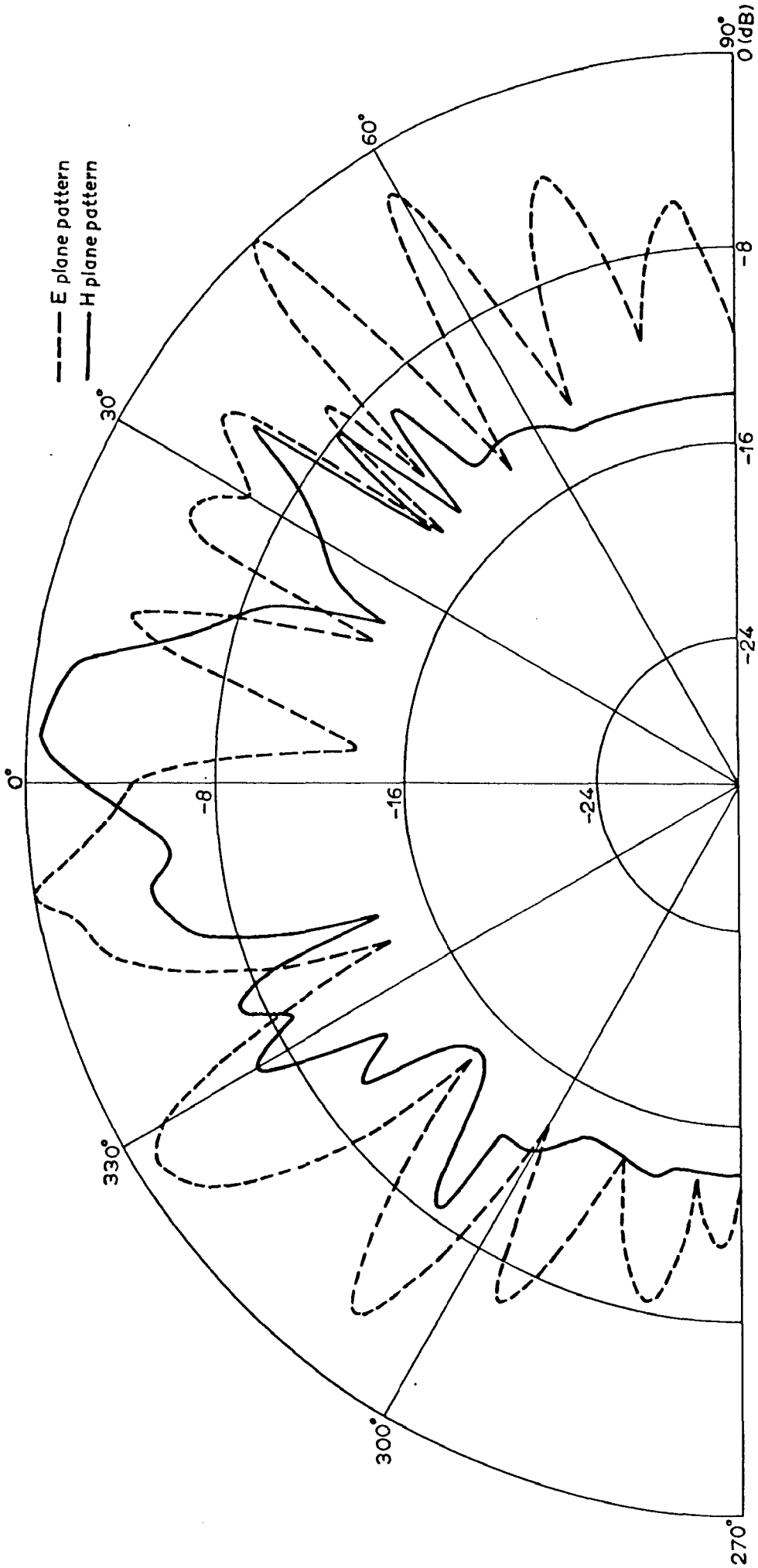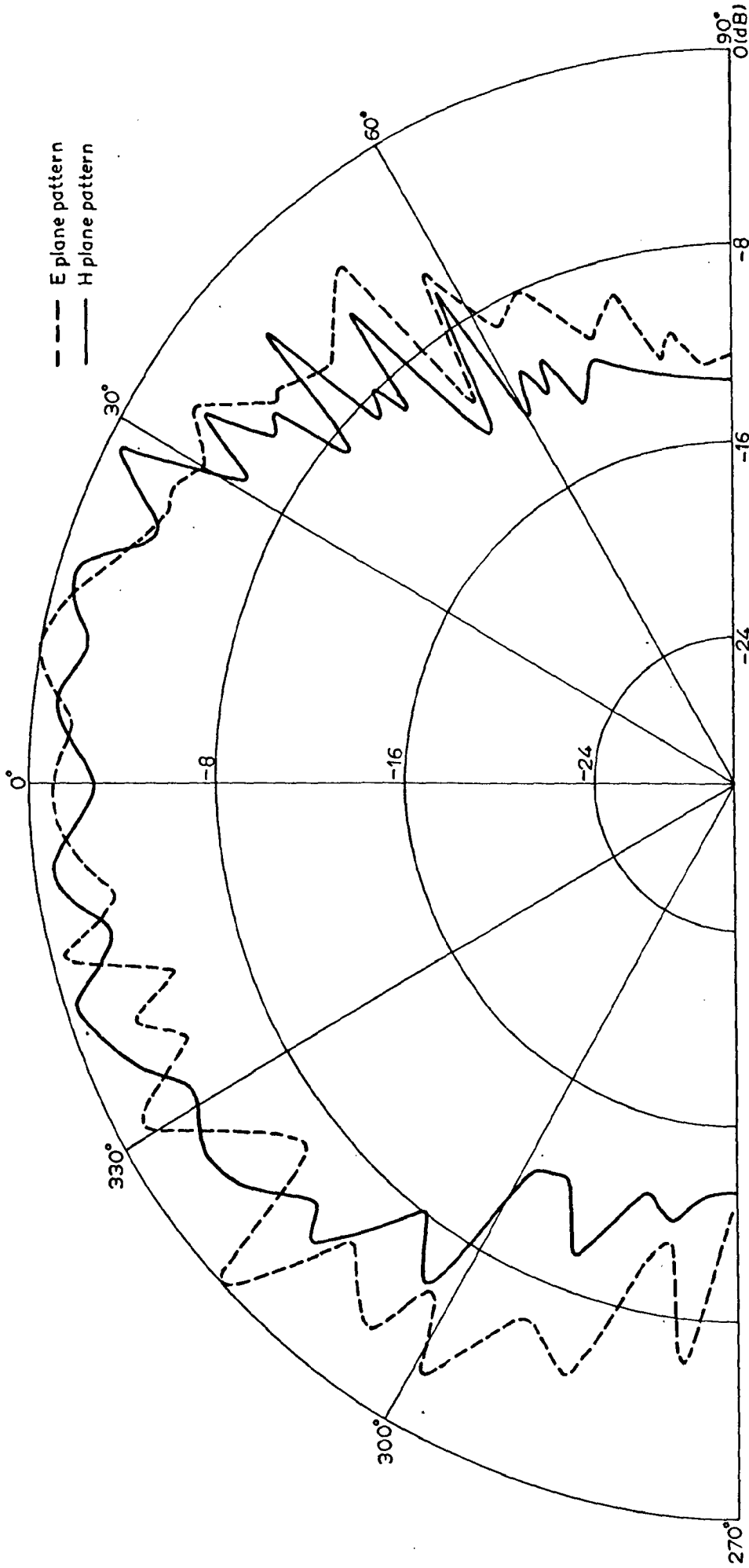H plane pattern

116
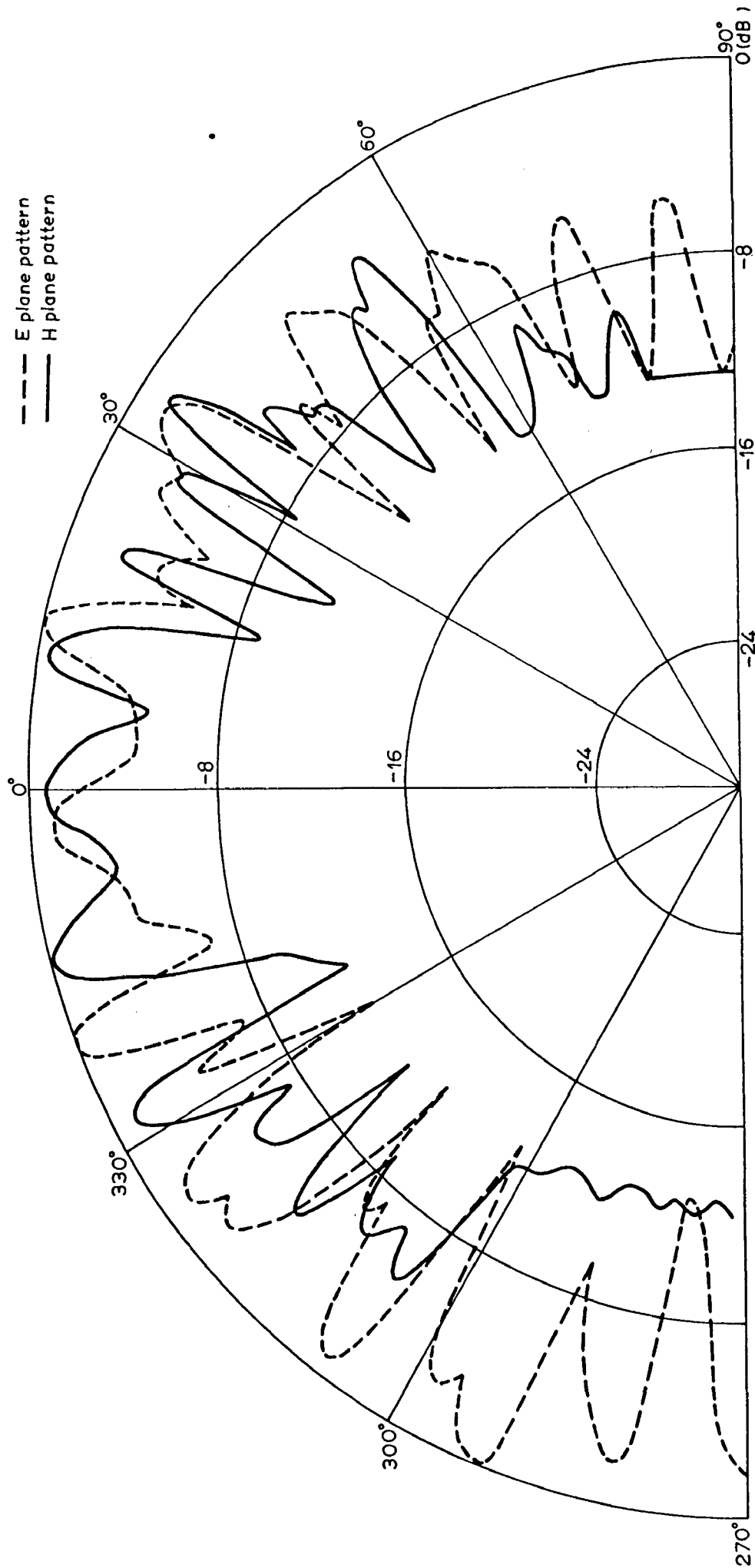
Fig.4.19:Radiation patterns of a patch antenna at 10.3GHz (EGP).
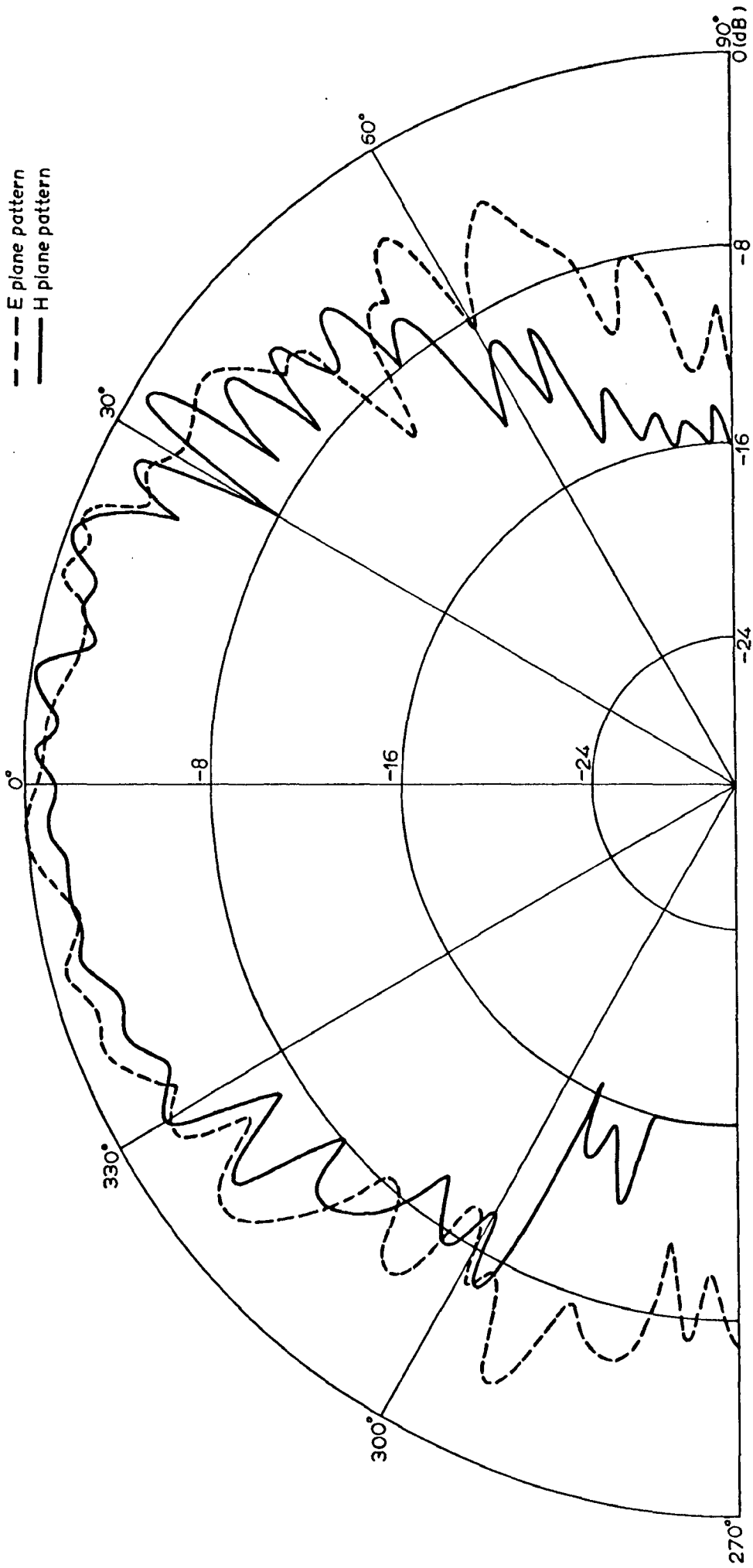
Fig.4.20: Radiation patterns of a patch antenna at 10.6GHz (EGP).
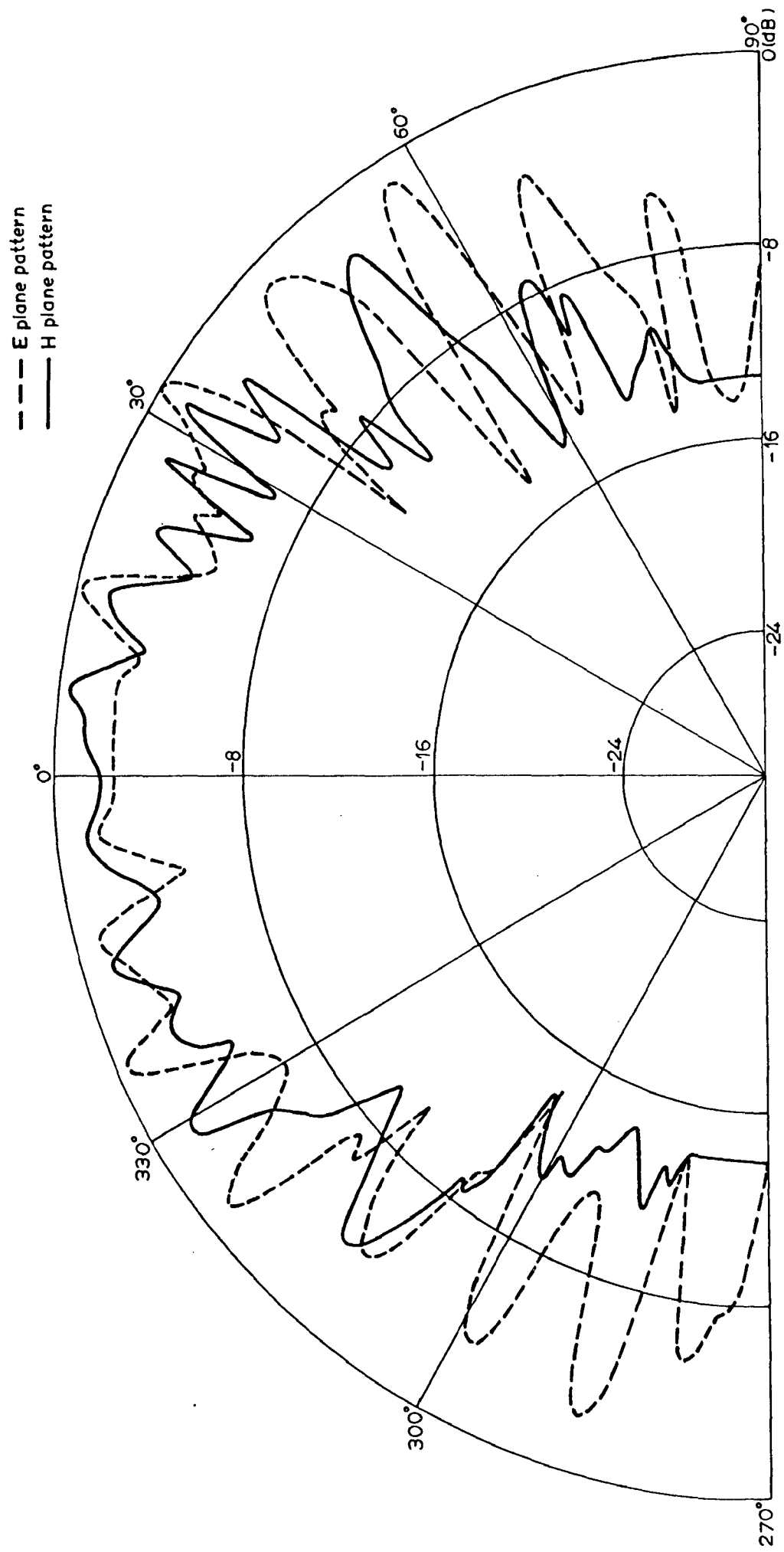
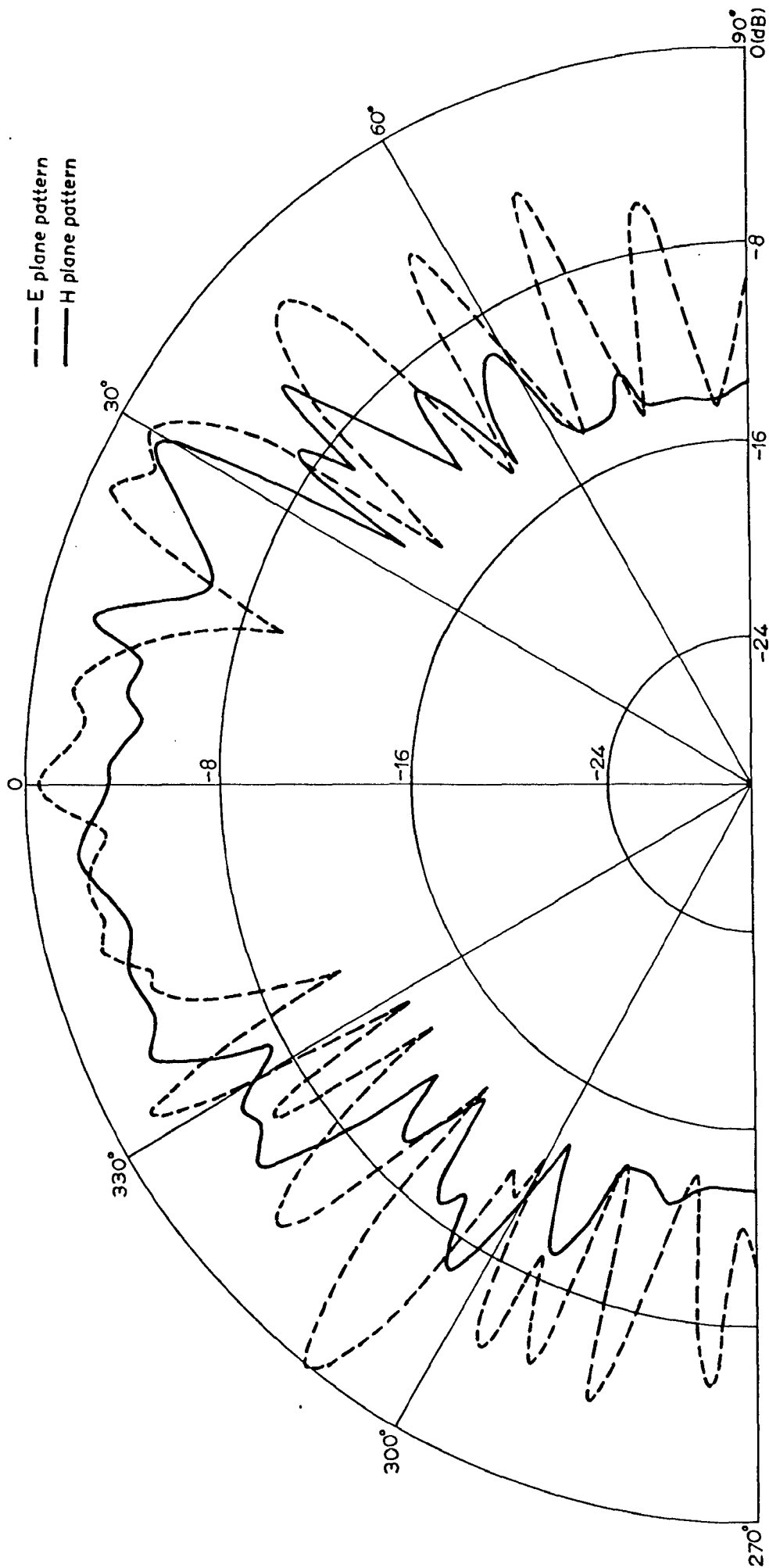Fig.4.21:Radiation patterns of a patch antenna at 11GHz(EGP).
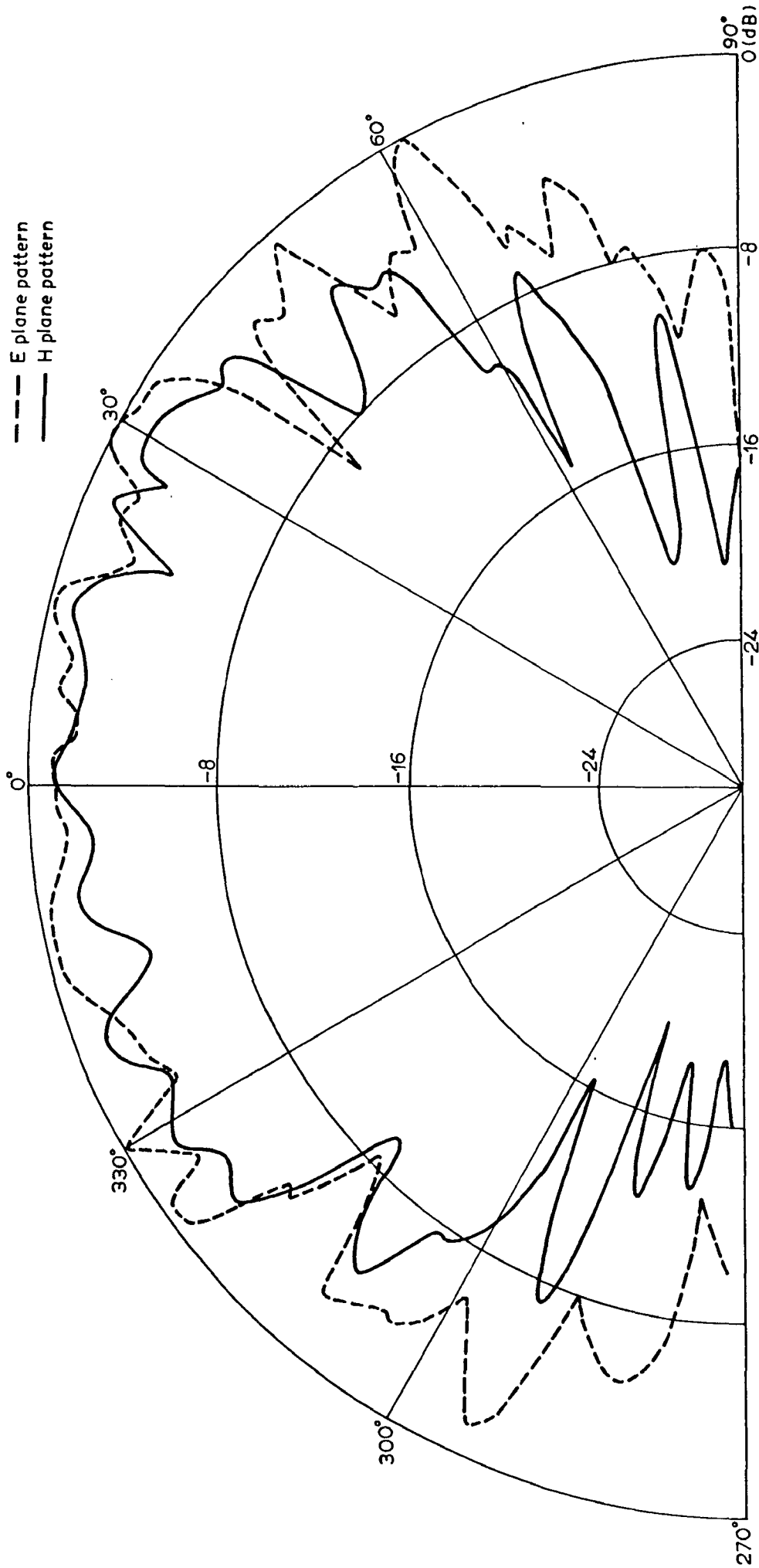
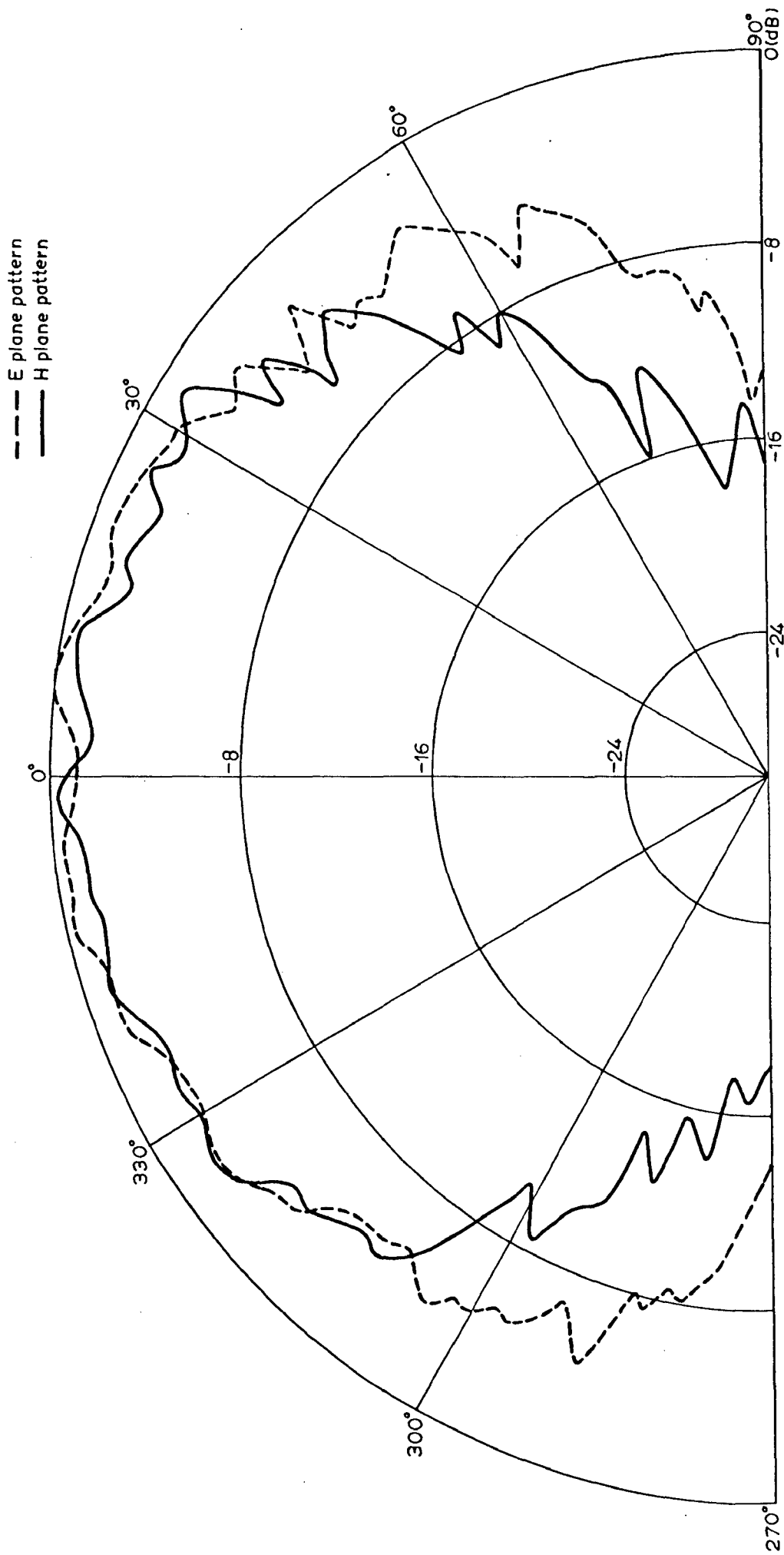- - - E plane pattern
——— H plane pattern

90°
O(dB)

-8

-16

-24

60°

30°

0°

330°

300°

270°

-8

-16

-24

Fig.4.22:Radiation patterns of a tuned patch antenna at 8.6GHz(EGP).

E plane pattern
H plane pattern

90° 0(dB)

120
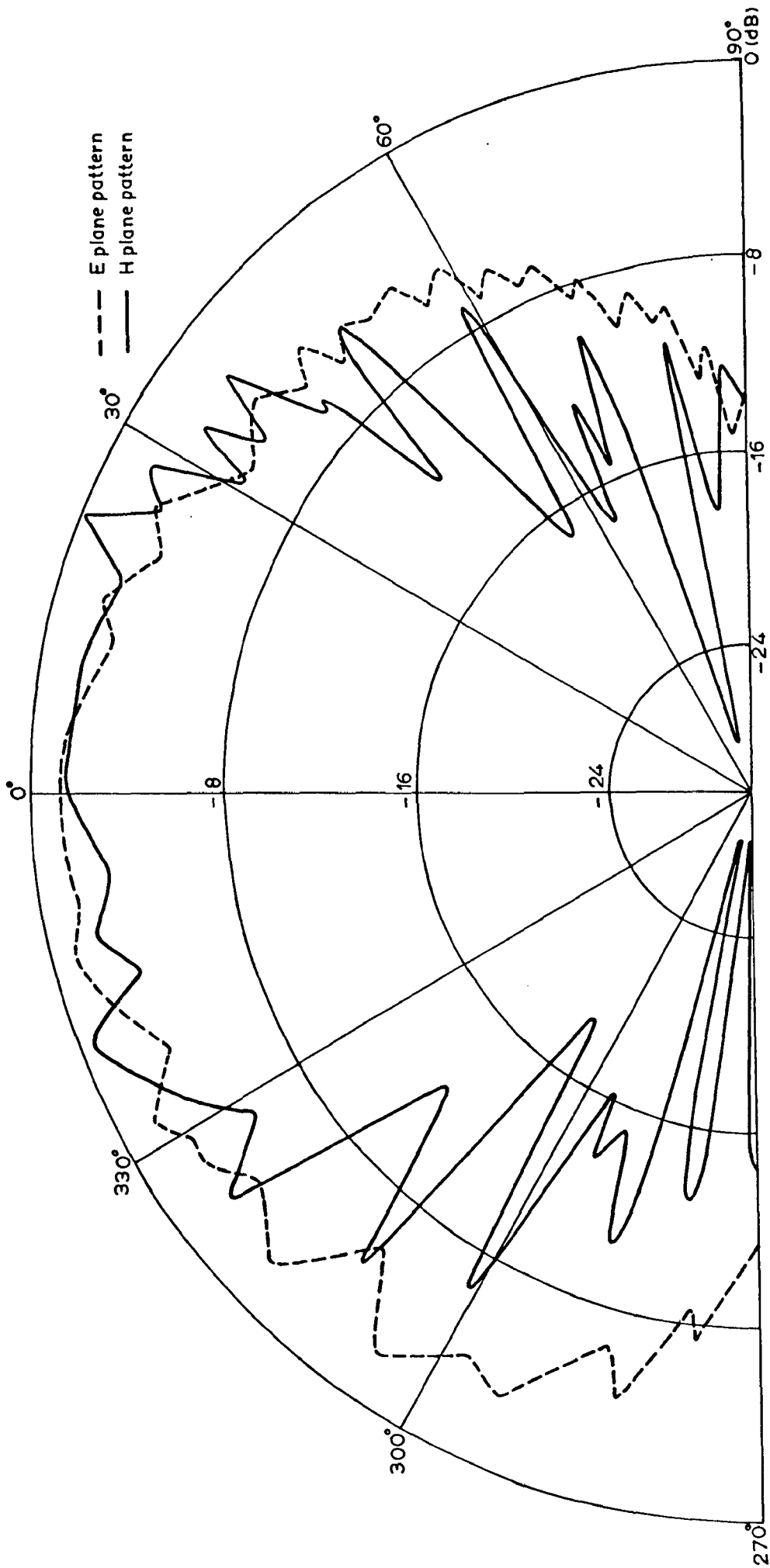
CHAPTER 5

CONCLUSIONS

In the preceding chapters, some investigations have been reported on a waveguide feed rectangular patch antenna. A moment method formulation has been presented for analysing the antenna and the expressions for various matrices and vectors have been derived. Based upon the analysis, a computer program has been developed, the results of which have also been presented. In this chapter, a critical examination of the analysis, the computer program and the numerical and the experimental results has been carried out and some of the areas which require further investigations have been identified.

5.1 The Analysis

A moment method analysis has been presented for a patch antenna fed by a waveguide. The formulation is completely general, in the sense that the shape and the size of the aperture and the patch can be arbitrary. However, for the actual evaluation of the matrix elements, a rectangular patch and a rectangular aperture have been considered. For the sake of simplicity, only the x-directed currents on the aperture and the y-directed currents on the patch have been assumed to be present, which is true for narrow apertures. Piecewise sinusoidal (PWS) functions have been used for both expansion as well as testing (the Galerkin's procecdure). While carrying

out the numerical experiments, rooftop (RT) functions were also utilised in a Galerkin's procedure. However, it was found that both the PWS and the RT functions give similar results. The matrix elements for the waveguide region have been evaluated using the waveguide dyadic Green's function for the electric vector potential in the spatial domain, while the other matrices have been evaluated using spectral domain Green's functions.

For the calculation of the reflection coefficient and hence, the input impedance, a TE_{10} mode is assumed to be incident in the waveguide. The radiation patterns have been determined for the particular case of an air-dielectric patch antenna.

5.2 The Computer Program

Based on the analysis, a computer program has been developed in FORTRAN. The program has been written in the modular form, as a result of which, any modifications can easily be incorporated in it. The variables have been named in such a way that the same names can be retained when the analysis is extended to take into account the y-directed currents on the aperture and the x-directed currents on the patch. A single integration routine has been used which is called several times from different subroutines. However, most of the variables in this routine do not change from one call to another call. Therefore, suitable modifications in the program, say, storing the numerical values of these variables in a database during the first call and using these variables in the subsequent calls, can greatly improve the speed of computation.

...ical Results

checke... ...ts obtained from the computer program have been results. ...convergence and compared with the published elements of ...the self impedance of the patch and the with the publis...ide admittance matrix had a good agreement reflection coeffici... in almost all the cases, the inpu instability with the ...stead of showing convergence, showd Although a number of n...se in the number of subsectios identify the source of this i... ...al t?sts were carried out to ...bilit?, no suitable explanation for the peculiar nature of the cu... ...uld be found.

When the aperture is narrow i...he y-direction, it can be approximated as a magnetic dipol...ith only a x-directed current distribution. Thus, the elec...c current induced on the patch will have only a y-directe...component. An open waveguide, on the other hand, cannot ...approximated as a dipole. Further, when a reflector is pl...ed in front of the waveguide, the field distribution over the a...erture is disturbed and no longer corresponds to that of the TE_{10} mode. Therefore, both the x and the y directed currents on the aperture as well as on the patch need to be considered to obtain reliable results.

Finally, test data has been generated for a waveguide fed microstrip patch antenna. The input characteristics indicated the presence of alternate series and parallel resonances. The input impedance, measured at the pla-

5.3 The Numerical Results

The results obtained from the computer program have been checked for the convergence and compared with the published results. Though, the self impedance of the patch and the elements of the waveguide admittance matrix had a good agreement with the published data in almost all the cases, the input reflection coefficient, instead of showing convergence, showed instability with the increase in the number of subsections. Although a number of numerical tests were carried out to identify the source of this instability, no suitable explanation for the peculiar nature of the curves could be found.

When the aperture is narrow in the y-direction, it can be approximated as a magnetic dipole with only a x-directed current distribution. Thus, the electric current induced on the patch will have only a y-directed component. An open waveguide, on the other hand, cannot be approximated as a dipole. Further, when a reflector is placed in front of the waveguide, the field distribution over the aperture is disturbed and no longer corresponds to that of the TE_{10} mode. Therefore, both the x and the y directed currents on the aperture as well as on the patch need to be considered to obtain reliable results.

Finally, test data has been generated for a waveguide fed microstrip patch antenna. The input characteristics indicated the presence of alternate series and parallel resonances. The input impedance, measured at the plane

containing the aperture, is a very strong function of waveguide-aperture and aperture-patch interactions. Since the resonant frequency has been obtained by considering the impedance referred to the plane of the aperture, it does not coincide with the resonant frequency of an isolated patch. The exact shift and its behaviour can be known only after carrying out more detailed investigations.

5.4 The Experimental Results

An effort was also made to study the characteristics of a waveguide feed patch antenna experimentally. The input characteristics showed the presence of alternate series and parallel resonances, a behaviour which is also predicted by the numerical results. These several parallel resonant points are arising due to the excitation of different modes. With the help of the input characteristics, namely, the input impedance and the VSWR, and the far-field quantities, namely, the radiation patterns and the gain, the resonant frequency of the patch antenna has been predicted. Since the gain was too low due to a high reflection loss at the aperture, a slide screw tuner was used to improve the gain. Though it resulted in an increased gain, the antenna patterns were seriously affected. Hence the use of a slide screw tuner is not recommended. Further, in view of the strong dependence of the input impedance on the location and size of the aperture, more detailed studies need to be carried out to find out an optimum location of the aperture vis-a-vis the patch.

In an effort to reduce the undulations in the radiation patterns, the size of the ground plane was increased which resulted in improved radiation patterns.

Since the radiation patterns are quite broad in both the planes, the reflections from the ground and the walls had a considerable effect on them. Use of microwave absorbers would have minimised these undesirable reflections. Further, the use of a network analyzer would have resulted in more accurate, reliable and repeatable measurements.

5.5 Recommendations for Further Work

In almost all the cases considered in this work, the reflection coefficient showed an oscillatory behaviour. Since, no suitable explanation could be found for this behaviour, further studies are required to resolve this problem.

It was found that at all the frequencies, the input mismatch was unacceptably high. Since, the input characteristics depend on the waveguide-aperture and aperture-patch interactions, more investigations are required to determine the optimum location and size of the aperture for obtaining a good impedance match. Since a purely experimental investigation is costly, time consuming and prone to tolerance-induced errors, a detailed theoretical study of the structure is recommended.

In order to study the effect of coupling via a wide slot, both the x and the y directed currents on the patch as well

as on the aperture have to be considered. Although it would increase the complexity of the problem, this investigation is necessary to fully characterise the waveguide feed patch antenna.

Another interesting problem to be analysed is the excitation of the patch antenna by a shunt slot in the broad wall of a rectangular waveguide. Studies have to be made to determine the location of the patch and the aperture with respect to the waveguide for optimal coupling into the antenna due to both electric and magnetic dipoles. A sliding short circuit terminating the waveguide beyond the antenna could be used to vary the positions of the peaks and nulls in the waveguide standing wave pattern to increase coupling into the antenna.

Finally, application of the aperture feed structure to arrays of microstrip patch antennas have to be considered. Feeding of several patches via longitudinal slots in the broad wall of a waveguide shall reduce the complexity of the feed structure.

APPENDIX A

Evaluation of the Electric Vector Potential
in the Waveguide Region (Eq. 2.52)

The electric vector potential given by (2.43) can be written in the form

$$\overline{F}_j = \epsilon_0 \iint_S \overline{\overline{g}}_m(\overline{r}|\overline{r}').(\overline{M}_j^x(\overline{r}')+\overline{M}_j^y(\overline{r}')) \; ds' \qquad (A.1)$$

Since $\overline{M}_j$ has only x-directed components, (A.1) reduces to

$$\overline{F}_j = \epsilon_0 \iint_S \overline{\overline{g}}_m(\overline{r}|\overline{r}').\overline{M}_j^x(\overline{r}') \; ds' \qquad (A.2)$$

The integrand of (A.2) can be written using (2.30) and (2.44) as

$$\overline{\overline{g}}_m(\overline{r}|\overline{r}').\overline{M}_j^x(\overline{r}') = \hat{x} \sum_m \sum_n [\epsilon_m \epsilon_n/(ab\Gamma_{mn})] \; (SS)_x \; (CC)_y$$
$$S_s^x(x'-x_c+L_{ap}/2) \; P_t^y(y'-y_c+W_{ap}/2) \qquad (A.3)$$

Substituting (A.3) in (A.2)

$$\overline{F}_j = \hat{x} \; \epsilon_0 \sum_m \sum_n [\epsilon_m \epsilon_n/(ab\Gamma_{mn})] \; Sin[(m\pi/a)(x+a/2)]$$
$$Cos[(n\pi/b)(y+b/2)] \iint_S S_s^x(x'-x_c+L_{ap}/2) \; P_t^y(y'-y_c+W_{ap}/2)$$
$$Sin[(m\pi/a)(x'+a/2)] \; Cos[(n\pi/b)(y'+b/2)] \; dx' \; dy' \qquad (A.4)$$

To evaluate the integral in (A.4), we write

$$I_1 = \iint_S S_s^x(x'-x_c+L_{ap}/2) \; P_t^y(y'-y_c+W_{ap}/2) \; Sin[(m\pi/a)(x'+a/2)]$$
$$Cos[(n\pi/b)(y'+b/2)] \; dx' \; dy' \qquad (A.5)$$

Substituting (2.31) and (2.32) in (A.5) with appropriate limits, we get

$$I_1 = \int_{x_a}^{x_b} \frac{\mathrm{Sin}\{k_{ap}[\Delta x - |x' - x_1 - s\Delta x|]\}}{\mathrm{Sin}(k_{ap}\Delta x)} \, \mathrm{Sin}[(m\pi/a)(x'+a/2)] \, dx'$$

$$\int_{y_a}^{y_b} (1/\Delta y) \, \mathrm{Sin}[(n\pi/b)(y'+b/2)] \, dy' \qquad (A.6)$$

$$= I_1^x \cdot I_1^y \quad (\text{say})$$

where

$$x_a = x_1 + (s-1)\Delta x \qquad x_b = x_1 + (s+1)\Delta x$$

$$y_a = y_1 + (t-1)\Delta y \qquad y_b = y_1 + t\Delta y \qquad (A.7)$$

The integral with respect to y' in (A.6) can be evaluated as

$$I_1^y = \int_{y_a}^{y_b} (1/\Delta y) \, \mathrm{Sin}[(n\pi/b)(y'+b/2)] \, dy'$$

$$= (1/\Delta y) \, [2/(n\pi/b)] \, \mathrm{Cos}[\frac{n\pi}{2b}(y_a+y_b+b)] \, \mathrm{Sin}[\frac{n\pi}{2b}(y_b-y_a)]$$

$$(A.8)$$

The integral with respect to x' in (A.6) within the limits x_a to x_b may be separated into two integrals, given by

$$I_1^x = \int_{x_a}^{x_b} \frac{\mathrm{Sin}\{k_{ap}[\Delta x - |x'-x_1-s\Delta x|]\}}{\mathrm{Sin}(k_{ap}\Delta x)} \, \mathrm{Sin}[(m\pi/a)(x'+a/2)] \, dx'$$

$$(A.9)$$

$$= \int_{x_a}^{x_c} \frac{Sin\{k_{ap}[\Delta x+x'-x_1-s\Delta x]\}}{Sin(k_{ap}\Delta x)} \; Sin[(m\pi/a)(x'+a/2)] \; dx'$$

$$+ \int_{x_c}^{x_b} \frac{Sin\{k_{ap}[\Delta x-x'+x_1+s\Delta x]\}}{Sin(k_{ap}\Delta x)} \; Sin[(m\pi/a)(x'+a/2)] \; dx' \qquad (A.10)$$

where

$$x_c = x_1 + s\Delta x \qquad (A.11)$$

On integrating (A.10), we get

$$I_1^x = [1/Sin(k_{ap}\Delta x)]\{Cos[(k_{ap}\Delta x/2)-(m\pi/a)(x_1+s\Delta x)$$

$$+(\frac{m\pi}{2a})\Delta x-(m\pi/2)] \; \frac{Sin[\{k_{ap}-(m\pi/a)\}(\Delta x/2)]}{[k_{ap}-(m\pi/a)]}$$

$$-Cos[(k_{ap}\Delta x/2)+(m\pi/a)(x_1+s\Delta x)-(\frac{m\pi}{2a})\Delta x+(m\pi/2)]$$

$$\frac{Sin[\{k_{ap}+(m\pi/a)\}(\Delta x/2)]}{[k_{ap}+(m\pi/a)]}$$

$$+Cos[(k_{ap}\Delta x/2)-(m\pi/a)(x_1+s\Delta x)-(\frac{m\pi}{2a})\Delta x-(m\pi/2)]$$

$$\frac{Sin[\{-k_{ap}-(m\pi/a)\}(\Delta x/2)]}{[-k_{ap}-(m\pi/a)]}$$

$$-Cos[(k_{ap}\Delta x/2)+(m\pi/a)(x_1+s\Delta x)+(\frac{m\pi}{2a})\Delta x+(m\pi/2)]$$

$$\frac{Sin[\{-k_{ap}+(m\pi/a)\}(\Delta x/2)]}{[-k_{ap}+(m\pi/a)]}\} \qquad (A.12)$$

which can be simplified further to get

$$I_1^x = [1/Sin(k_{ap}\Delta x)]\left[\frac{Sin\{\frac{n\pi\Delta y}{2b}\}}{\{\frac{n\pi\Delta y}{2b}\}}\right]\left[\frac{4\ k_{ap}}{k_{ap}^2-(m\pi/a)^2}\right]$$

$$Cos[(n\pi/b)(y_1+t\Delta y)-(\frac{n\pi}{2b})\Delta y+(n\pi/2)]$$

$$Sin[\{k_{ap}+(m\pi/a)\}(\Delta x/2)]\quad Sin[\{k_{ap}-(m\pi/a)\}(\Delta x/2)]$$

$$Sin[(m\pi/a)(x_1+s\Delta x)+(m\pi/2)]\quad\quad\quad\quad\quad (A.13)$$

Substituting (A.6), (A.8) and (A.13) in (A.4), we obtain expression for the electric vector potential.

APPENDIX B

Fourier Transform of Basis Functions

The k_x dependent part of the Fourier transform of $M_j^x(x_o, y_o)$ is given, from (2.78) and (2.80), as

$$F_{M_j^x}(k_x) = \int_{x_o} S_s^x(x_o - x_c + L_{ap}/2) \, e^{-jk_x x_o} \, dx_o \qquad (B.1)$$

Using (2.30) in (B.1), we get

$$F_{M_j^x}(k_x) = \int_{x_1 + (s-1)\Delta x}^{x_1 + (s+1)\Delta x} \frac{Sin[k_{ap}(\Delta x - |x_o - x_1 - s\Delta x|)]}{Sin(k_{ap}\Delta x)} \, e^{-jk_x x_o} \, dx_o \qquad (B.2)$$

(B.2) can be separated as

$$F_{M_j^x}(k_x) = \int_{x_1 + (s-1)\Delta x}^{x_1 + s\Delta x} \frac{Sin[k_{ap}(\Delta x + x_o - x_1 - s\Delta x)]}{Sin(k_{ap}\Delta x)} \, e^{-jk_x x_o} \, dx_o$$

$$+ \int_{x_1 + s\Delta x}^{x_1 + (s+1)\Delta x} \frac{Sin[k_{ap}(\Delta x - x_o + x_1 + s\Delta x)]}{Sin(k_{ap}\Delta x)} \, e^{-jk_x x_o} \, dx_o \qquad (B.3)$$

Integrating (B.3) by parts and then simplifying, we get

$$F_{M_j^x}(k_x) = \frac{2k_{ap}}{k_x^2 - k_{ap}^2} \left[Cot(k_{ap}\Delta x) - \frac{Cos(k_x \Delta x)}{Sin(k_{ap}\Delta x)}\right] e^{-jk_x(x_1 + s\Delta x)} \qquad (B.4)$$

The k_y dependent part of the Fourier transform of $M_j^x(x_o, y_o)$ is given, from (2.78) and (2.80), as

$$F_{M_j^x}(k_y) = \int_{Y_o} P_t^y(y_o - y_c + W_{ap}/2)\, e^{-jk_y y_o}\, dy_o \tag{B.5}$$

Using (2.30) in (B.5), we get

$$F_{M_j^x}(k_y) = \int_{y_1+(t-1)\Delta y}^{y_1+t\Delta y} (1/\Delta y)\, e^{-jk_y y_o}\, dy_o \tag{B.6}$$

(B.6) is readily integrated to get

$$F_{M_j^x}(k_y) = \frac{\sin(k_y \Delta y/2)}{(k_y \Delta y/2)}\, e^{-jk_y[y_1+(t-\frac{1}{2})\Delta y]} \tag{B.7}$$

Following the same procedure, conjugate Fourier transform of M_j^x can be obtained.

REFERENCES

1. G.A. Deschamps, "Microstrip antennas", presented at 3rd USAF Symposium on Antennas, 1953.

2. J.Q. Howell, "Microstrip antennas", IEEE AP-S Int. Symp. Digest, pp. 177-180, 1972.

3. R.E. Munson, "Conformal microstrip antennas and microstrip phased arrays", IEEE Trans. Antennas and Propag., vol. AP-22, pp. 74-78, Jan. 1974.

4. B. Roudot, J. Mosig, and F. Gardiol, "Surface wave effects on microstrip antenna radiation", Microwave Journal, pp. 201-211, March 1988.

5. A.G. Derneryd, "Analysis of microstrip disk element", IEEE Trans. Antennas and Propag., vol. AP-27, pp. 660-664, Sept. 1976.

6. A.G. Derneryd, "Linearly polarised microstrip antennas", IEEE Trans. Antennas and Propag., vol. AP-22, pp. 846-851, Nov. 1976.

7. H. Pues and A. Van de Capelle, "Accurate transmission line model for the rectangular microstrip antenna", IEE Proc., vol. 131, Pt. H, pp. 334-340, Dec. 1984.

8. Y.T. Lo, D. Solomon, and W.F. Richards, "Theory and experiment on microstrip antennas", IEEE Trans. Antennas and Propag., vol. AP-27, pp. 137-145, March 1979.

9. D.M. Pozar, "Considerations for millimeter wave printed antennas", IEEE Trans. Antennas and Propag., vol. AP-31, pp. 740-747, Sept. 1983.

10. H.G. Oltman, "Electromagnetically coupled microstrip dipole antenna element", Proc. 8th European Microwave Conference, Paris, pp. 281-285, 1978.

11. J.R. James, P.S. Hall, and C. Wood, "Microstrip antenna theory and design", Peter Peregrinus Ltd., 1981.

12. D.M. Pozar, "Microstrip antenna aperture coupled to a microstrip line", Electron. Lett., vol. 21, pp. 49-50, Jan. 1985.

13. D.M. Pozar, "An update on microstrip antenna theory and design including some novel feeding techniques", IEEE Antennas and Propag. Society Newsletter, pp. 5-9, Oct. 1986.

14. D.M. Pozar, "A reciprocity method of analysis for printed slot and slot-coupled microstrip antennas", IEEE Trans. Antennas and Propag., vol. AP-34, pp. 1439-1446, Dec. 1986.

15. D.H. Greenlee, M. Kanda, and D.C. Chang, "The characteristics of iris-fed millimeterwave rectangular microstrip patch antennas", NBS Technical Note 1063, Oct. 1983.

16. M.C. Bailey and M.D. Deshpande, "Integral equation formulation of microstrip antennas", IEEE Trans. Antennas and Propag., vol. AP-30, pp. 651-656, July 1982.

17. S.K. Verma, "A moment solution for thick dielectric filled windows in a waveguide", M.E. Dissertation, Dept. of Electronics and Computer Engg., University of Roorkee, Sept. 1987.

18. R.H. Jansen, "The spectral-domain approach for microwave integrated circuits", IEEE Trans. Microwave Theory Techniques, vol. MTT-33, pp. 1043-1056, Oct. 1985.

19. P.L. Sullivan and D.H. Schaubert, "Analysis of an aperture coupled microstrip antenna", ANTLAB Report No. 8501, Electrical and Computer Engg., University of Massachusetts at Amherst, July 1985.

20. S.N. Sinha, "Experimental and theoretical investigations on reactively loaded waveguide-fed short-backfire arrays", Ph.D. Thesis, Dept. of Electronics and Computer Engg., University of Roorkee, July 1983.

21. D.M. Pozar, "Improved computational efficiency for the moment method solutions of printed dipoles and patches", Electromagnetics, 3, pp. 299-309, 1983.

22. N.K. Uzunoglu, N.G. Alexopoulos, and J.G. Fikioris, "Radiation properties of microstrip dipoles", IEEE Trans. Antennas and Propag., vol. AP-27, pp. 853-858, Nov. 1979.

23. D.M. Pozar, "Input impedance and mutual coupling of rectangular microstrip antennas", IEEE Trans. Antennas and Propag., vol. AP-30, pp. 1191-1196, Nov. 1982.

24. I.J. Bahl and P. Bhartia, "Microstrip antennas", Artech House, Inc., USA, 1982.

25. T.S. Laverghetta, "Microwave materials and fabrication techniques", Artech House, Inc., USA, 1985.

26. I.L. Kosow, "Microwave theory and measurements", Prentice-Hall, Inc., Englewood Cliffs, N.J., 1962.

27. R.W. Dearnley and A.R.F. Barel, "A comparison of models to determine the resonant frequencies of a rectangular microstrip antenna", IEEE Trans. Antennas and Propag., vol. AP-37, pp. 114-118, Jan. 1989.